

NUMERICAL INVERSE SPECTRAL TRANSFORM FOR THE PERIODIC SINE-GORDON EQUATION: THETA FUNCTION SOLUTIONS AND THEIR LINEARIZED STABILITY

Randy FLESCH

Department of Mathematics, Heriot-Watt University, Edinburgh, UK

M. Gregory FOREST¹ and Amarendra SINHA²

Department of Mathematics, The Ohio State University, Columbus, OH 43210, USA

Received 30 August 1989

Revised manuscript received 13 July 1990

Accepted 5 August 1990

Communicated by H. Flaschka

The inverse spectral transform for integrable nonlinear ordinary and partial differential equations (such as the Toda lattice, Korteweg–de Vries, sine-Gordon and nonlinear Schrödinger equations) provides explicit algorithms to generate exact solutions under periodic or quasiperiodic boundary conditions. These oscillatory wavetrains may be prescribed a priori to consist of a nonlinear superposition of N phases, $\theta_j(x, t) = \kappa_j x + \omega_j t + \theta_j^0$, $j = 1, \dots, N$, where the wave is 2π -periodic independently in each phase. This paper exhibits the numerical implementation of the inverse spectral solution of the sine-Gordon equation. The general construction is outlined and then implemented for $N = 1, 2$, and 3 . We compute: (1) the exact theta-function solutions, (2) the Floquet spectrum of x -periodic solutions, (3) the labelling of linearized instabilities of N -phase solutions in terms of spectral data, and (4) the linearized growth rate in each unstable mode. The associated surfaces $q_N(x, t)$ are displayed to illustrate a variety of spatial and dynamical phenomena in the oscillatory solution space of this integrable system.

1. Introduction

In this paper we are concerned with explicit computation of exact oscillatory solutions of the completely integrable sine-Gordon partial differential equation (PDE). The method of solution, the inverse spectral transform, will be briefly summarized here to the extent necessary to explain the algorithms for computation of these solutions and of their salient physical properties (spatial wavenumbers, temporal frequencies and linearized instabilities).

The sine-Gordon equation is one of many completely integrable systems, including ODEs such as the Toda lattice [1], and PDEs such as the Korteweg–de Vries (KdV) and nonlinear Schrödinger (NLS) equations [2–7]. The solution of each integrable PDE involves the spectral theory of a special linear differential operator with variable coefficients, where the Cauchy data of the PDE determines the variable coefficients of this operator. Boundary conditions become very important in this solution

¹Research partially supported by the National Science Foundation, Grant Number DMS-8803465.

²Computer time on the Cray YMP has been granted by the Ohio Supercomputer Center.

technique, since the spatial boundary conditions imposed on the PDE and its Cauchy data are likewise imposed on the linear operator. The solution technique and classes of solutions of the nonlinear PDE are therefore limited to those boundary conditions for which one can control the spectrum of this linear variable coefficient differential operator. The two principal successes have occurred with square integrable boundary conditions on the infinite line and periodic boundary conditions on a finite interval. (There are other examples which will not be discussed here.)

For decaying boundary conditions on the infinite line, the PDE solution technique is called *inverse scattering theory*, which has produced the well-known N -soliton solutions. For oscillatory solutions (either periodic or quasiperiodic) which are bounded as $|x| \rightarrow \infty$ but not square integrable on the line, the technique is called *inverse spectral theory* (IST) and has produced the class of N -phase wavetrains (the analog of N solitons per finite period). For periodic boundary conditions, the IST solution involves the Floquet theory of a linear differential operator with periodic coefficients, as we will summarize below.

Whereas N -soliton formulas are given by rational combinations of exponential functions, oscillatory N -phase wavetrains are represented in terms of Riemann theta functions. The simple functional form of N solitons has led to a wide range of scientific applications. In contrast, the mathematical and computational complexities of computing integrable oscillatory wavetrains, explained in the text below, have hindered the use of these solutions in applications. A few exceptions exist: special N -phase solutions of the NLS equation have been computed by Tracy [4] to display modulational instabilities in the neighborhood of plane waves; Segur and coworkers [8] have computed two-phase solutions of the Kadomstev-Petviashvili equation which were then fitted to doubly periodic surface waves in shallow water. Also, Boyd and coworkers [9] have analyzed techniques to sum theta series and perturbation methods to replace direct theta function computations.

The present paper outlines the numerical implementation of the inverse spectral algorithm for oscillatory solutions of the sine-Gordon equation. The codes described here generate *the class of N -phase quasiperiodic wavetrains for small N (1, 2 and 3). Special care must be taken to handle the subclass of periodic solutions*. We will first describe the inverse spectral solution algorithm; then we will generate specific 1-, 2-, and 3-phase solutions. We will list only those ingredients of inverse spectral theory which are essential for computing these wavetrains, for characterizing their physical wavenumbers and frequencies, and for determining the linearized stability of periodic solutions.

These computations are intended, firstly, *to show how soliton wavetrains can be systematically computed and displayed and to show where the essential problems lie*. Secondly, we plan to use these codes in conjunction with our studies of the perturbed sine-Gordon equation under periodic boundary conditions [10, 11]. To cite two examples: we are currently applying the codes of this paper to predict existence or nonexistence of frequency and phase-locked periodic solutions of the damped and periodically driven sine-Gordon PDE; also, we plan to simulate the modulation equations for perturbed multiphase sine-Gordon wavetrains [12].

We will now describe, in general terms, the direct and inverse spectral transform for the periodic sine-Gordon (s-G) equation. The *direct spectral transform* (DST) is the nonlinear analog of the periodic Fourier transform for linear evolutionary PDEs: the s-G Cauchy data, $(q(x, 0), q_t(x, 0))$, $x \in [0, L]$, is resolved with respect to a nonstandard set of spatial modes. Unlike the fixed orthogonal basis of linear Fourier modes, the s-G nonlinear mode set consists of the class of " N -phase waveforms", to be computed in this paper. This set of N -phase wavefunctions is known to be complete in $L^2[0, P]$ for the integrable KdV example, and almost surely is complete in the sine-Gordon example but a rigorous proof remains to be provided.

The linear Fourier transform of a function $f(x)$ provides the amplitude in each Fourier mode on $[0, L]$. One can then approximate $f(x)$ by a finite sum of Fourier components, where the coefficients in this sum are the Fourier transform data. For sine-Gordon, the DST in principle yields an approximation of the Cauchy data $(q(x, 0), q_t(x, 0))$, $x \in [0, L]$, by a nonlinear waveform which is the analog of N solitons per finite period. The data of the DST transform, however, is the spectrum of a linear differential operator in x with periodic coefficients determined by the PDE Cauchy data.

We remark that the DST has been successfully implemented in studies of the periodic Toda lattice [13], the periodic KdV equation [14], and the perturbed periodic sine-Gordon [15] and NLS [16] equations. In these studies, the DST is applied to measure the nonlinear mode content in the solution at each time step, and then to interpret the perturbed solution in terms of this integrable mode basis. The reconstruction of the approximate “ N -phase spatial waveform” from this DST spectral data requires the inverse spectral transform, which is not as simple as a linear superposition in the linear Fourier analog. Rather, the N -phase waveforms involve theta functions of N variables, and this paper effects their explicit computation beginning with DST data. This reconstruction by IST of the integrable solution was not relevant to the studies in refs. [13–16]; rather, the important issues in those studies related to whether a given integrable mode approximation at one time step was robust and uniform in future time steps.

For the purpose of PDE dynamics, the Fourier transform for linear PDEs with spatially independent coefficients and the DST for integrable nonlinear PDEs have an important role. For such linear PDEs, if the Cauchy data $f(x)$ has exactly N nonzero Fourier amplitudes, then the PDE solution evolves as a time-dependent linear sum of those N Fourier modes. Moreover, if $f(x)$ is only approximated by N Fourier modes, and if there are no instabilities in the remaining Fourier modes, then the linear PDE solution corresponding to this data is approximated by an N -mode sum for all future times. With regard to the periodic DST for an integrable PDE, the time evolution of Cauchy data in the form of an N -phase spatial waveform is an exact N -phase solution whose explicit x, t dependence is known. Moreover, if this N -phase periodic wavetrain does not have any linearized instabilities, then Cauchy data which is approximately an N -phase spatial waveform will evolve by the sine-Gordon flow as an approximate N -phase wavetrain.

We now present the two linear differential operators in x and t (the so-called *Lax pair*) upon which the inverse spectral transform solution of sine-Gordon is based. The initial data is presumed periodic in x of fixed period L ,

$$q(x, 0) = (q(x, 0), q_t(x, 0)), \quad x \in [0, L], \quad (1.1a)$$

$$q(x + L, 0) = q(x, 0) \bmod 2\pi, \quad (1.1b)$$

$$q_t(x + L, 0) = q_t(x, 0), \quad (1.1c)$$

and periodic boundary conditions are imposed for all time,

$$(q(x + L, t), q_t(x + L, t)) = (q(x, t) \bmod 2\pi, q_t(x, t)). \quad (1.2)$$

The appropriate phase or *function space* $\mathcal{F}^{(L)}$ for the periodic sine-Gordon PDE consists of an $L^2 \times L^2$ completion of all function pairs $(q, q_t)(x) \in C^\infty[0, L] \times C^\infty[0, L]$ which satisfy (1.2).

For such $(q, q_t) \in \mathcal{F}^{(L)}$, with $\psi = (\psi_1, \psi_2)^t$, the spatial linear operator $\mathcal{L}^{(x)}$ is given by

$$\mathcal{L}^{(x)}\psi = \left[\begin{pmatrix} 0 & -1 \\ 1 & 0 \end{pmatrix} \frac{d}{dx} + \frac{i}{4}(q_t + q_x) \begin{pmatrix} 0 & 1 \\ 1 & 0 \end{pmatrix} + \frac{1}{16\sqrt{E}} \begin{pmatrix} e^{iq} & 0 \\ 0 & e^{-iq} \end{pmatrix} - \sqrt{E} \begin{pmatrix} 1 & 0 \\ 0 & 1 \end{pmatrix} \right] \psi = 0, \quad (1.3)$$

where $E \in \mathbb{C}$ is the spectral parameter. We remark that $\mathcal{L}^{(x)}$ is *non-selfadjoint*, a fact which makes the spectrum of $\mathcal{L}^{(x)}$ complex and which is ultimately responsible for many of the s-G solution properties (e.g., instabilities) and problems (e.g., characterizing real solutions) that are not shared by integrable PDEs solved through selfadjoint spectral theory. The corresponding temporal operator $\mathcal{L}^{(t)}$ is given by

$$\mathcal{L}^{(t)}\psi = \left[\begin{pmatrix} 0 & -1 \\ 1 & 0 \end{pmatrix} \frac{d}{dt} + \frac{i}{4}(q_t + q_x) \begin{pmatrix} 0 & 1 \\ 1 & 0 \end{pmatrix} - \frac{1}{16\sqrt{E}} \begin{pmatrix} e^{iq} & 0 \\ 0 & e^{-iq} \end{pmatrix} - \sqrt{E} \begin{pmatrix} 1 & 0 \\ 0 & 1 \end{pmatrix} \right] \psi = 0. \quad (1.4)$$

The compatibility condition $\psi_{xt} = \psi_{tx}$ holds for simultaneous eigenfunctions of $\mathcal{L}^{(x)}$ and $\mathcal{L}^{(t)}$ if and only if the coefficients (q, q_t) satisfy the sine-Gordon equation,

$$q_{tt} - q_{xx} + \sin q = 0. \quad (1.5)$$

Thus, the Lax pair $(\mathcal{L}^{(x)}, \mathcal{L}^{(t)})$ carries the sine-Gordon PDE as a compatibility condition, the essential fact which is exploited to solve the s-G PDE.

The DST for the periodic sine-Gordon equation is a map from periodic Cauchy data $q(x, 0)$, $x \in [0, L]$, eq. (1.1), to the set of periodic and antiperiodic eigenvalues of $\mathcal{L}^{(x)}$, which we shall call the periodic spectrum $\Sigma^{(p)}(q)$, and where $q(x, 0) = (q(x), q_t(x))$ determine the variable coefficients of $\mathcal{L}^{(x)}$, (1.3). By definition,

$$\begin{aligned} \Sigma^{(p)}(q) &= \{E_k \in \mathbb{C} \mid \mathcal{L}^{(x)}\psi(x; E = E_k) = 0, \psi(x + L; E_k) = \pm \psi(x; E_k)\}, \\ \text{DST: } q(x) &= (q(x), q_t(x)) \rightarrow \Sigma^{(p)}(q). \end{aligned} \quad (1.6)$$

Complete integrability of the periodic sine-Gordon equation is embodied in the following two remarkable facts [5, 7]:

Fact 1. $\Sigma^{(p)}(q(x, 0)) = \Sigma^{(p)}(q(x, t))$ if $q(x, t)$ solves the sine-Gordon PDE, i.e., the periodic spectrum of any initial data $q(x, 0)$ is invariant as this data evolves according to the sine-Gordon flow (1.5).

Fact 2. A complete set of (countably infinite) conserved quantities for the periodic s-G PDE is provided by $\Sigma^{(p)}(q(x, t))$. For example, the conserved sine-Gordon energy and momentum functionals, as well as the remaining complete list of higher-order integrals, are functions of $\Sigma^{(p)}(q)$.

Therefore, at least in principle, the DST yields a complete nonlinear mode decomposition for arbitrary initial data (1.1). By analogy, sine-Gordon *infinite-line scattering theory* employs $\mathcal{L}^{(x)}$ with “potentials” $(q(x), q_t(x))$ in a weighted subspace of $L^2(\mathbb{R}) \times L^2(\mathbb{R})$. The direct scattering transform then consists of the discrete spectrum of $\mathcal{L}^{(x)}$, which precisely determines the soliton composition of $q(x)$, and of the continuous spectrum of $\mathcal{L}^{(x)}$, which describes the nonsoliton radiation composition of $q(x)$.

Given these spectral measurements of Cauchy data, the main interest for dynamics is to determine the nonlinear mode content for future times $t \geq 0$. The interest in solitons, for example, is based on their dynamical interactions, and the ability to write down precise functional forms for the N -soliton solutions. In this direction, the infinite-line DST produces a precise characterization of pure N -soliton waveforms.

The Cauchy data $q(x, 0)$, in an appropriate subspace of $L^2(\mathbb{R}) \times L^2(\mathbb{R})$, evolves as a pure N -soliton solution of s-G if and only if the spectrum of $\mathcal{L}^{(x)}$ is purely discrete, with N discrete eigenvalues, and the reflection coefficient vanishes identically.

The inverse scattering transform (IST) on the infinite-line is a map from the scattering data of $\mathcal{L}^{(x)}$ (i.e., the spectrum, discrete and continuous) to the coefficients $(q(x), q_t(x))$; the IST map is the inverse of the DST map, as the name implies. Moreover, the infinite-line IST solution method employs the linear time-dependent operator $\mathcal{L}^{(t)}$, (1.4), to explicitly time-advance $q(x, 0)$ to $q(x, t)$.

In particular, the N -soliton solutions are generated as follows. From DST, one knows to select a pure discrete spectrum of N eigenvalues of $\mathcal{L}^{(x)}$ with zero reflection coefficient, and from IST one has a precise formula for $q(x, t)$ for all $t \geq 0$, which is guaranteed to evolve as an N -soliton waveform since the DST data is invariant in time. These infinite-line details may be found in any of the soliton textbooks.

For this paper, we will implement the analogous construction of N -soliton oscillatory wavetrains for $N = 1, 2, 3$. The periodic DST provides the spectral data $\Sigma^{(p)}(q(x, 0))$ that uniquely specifies N -soliton oscillatory waveforms. The initial data is guaranteed to evolve as an N -mode nonlinear wavetrain. The periodic IST solution then yields an explicit formula for these N -soliton wavetrains. This information is compiled in section 3.

In both the infinite-line and periodic cases, the inverse spectral solution is summarized by the following diagram:

$$\begin{array}{ccc} q(x, 0) & \xrightarrow[\mathcal{L}^{(x)}]{(1) \text{ DST}} & \Sigma(q(x, 0)) \\ & \downarrow (2) \mathcal{L}^{(t)} & \\ q(x, t) & \xleftarrow[\mathcal{L}^{(x)}]{(3) \text{ IST}} & \Sigma(q(x, t)) \end{array}$$

We will not need the full details of this diagram. Rather, we will implement the result of steps (2) and (3) for special choices of periodic spectrum $\Sigma^{(p)}(q(x, 0))$ which correspond to oscillatory N -soliton wavetrains for $N = 1, 2, 3$.

The remainder of the paper is organized as follows. In section 2 we recall the classical construction of one-soliton wavetrains (single-phase sine-Gordon solutions) by Jacobi elliptic functions. In section 3 we summarize the IST formula for N -soliton wavetrains (N -phase sine-Gordon solutions). In section 4 we summarize the IST ingredients necessary to determine all linearized instabilities of periodic N -phase wavetrains. Then in sections 5, 6, and 7 we numerically compute the IST solutions and their stability properties for $N = 1, 2, 3$. The final section 8 displays infinite-period (soliton) limits of two-phase waves and the one-phase limit of two-phase waves.

2. Single-phase solutions by classical analysis

We begin with the classical construction of one-phase solutions, which does not require IST, in order to illustrate the necessary ingredients for the general IST algorithm in a familiar setting.

The single-phase periodic solutions of the sine-Gordon equation,

$$q_{tt} - q_{xx} + \sin q = 0 \tag{2.1}$$

may be constructed by reduction to a traveling wave ode,

$$q(x, t) \equiv q_1(\theta) \equiv q_1(\kappa x + \omega t) \quad (2.2a)$$

with 2π -periodicity in the *phase* or *angle* θ ,

$$q_1(\theta + 2\pi) = q_1(\theta) \pmod{2\pi}. \quad (2.2b)$$

Each solution of this form yields, perhaps after rescaling, a pendulum equation. We begin with the simple case of (2.2a) where $\kappa = 0$, corresponding to x -independent pendulum solutions of the PDE (2.1),

$$q_{tt} + \sin q = 0. \quad (2.3a)$$

The classical analysis of this integrable ODE yields the complete family of solutions,

$$q(t) = 2 \sin^{-1}(k \operatorname{sn}(t - t_0; k)), \quad \text{real } t\text{-period} = 4K(k), \quad (2.3b)$$

parametrized by the modulus k of the Jacobi elliptic function sn and by the phase shift t_0 . The temporal period involves the complete elliptic integral of the first kind, $K(k)$, and yields the explicit nonlinear amplitude–frequency relation. The modulus k is an invariant of (2.3a) and is related to the conserved total energy H by

$$k^2 = \frac{1}{2}H = \frac{1}{2}\left(\frac{1}{2}q_t^2 + 1 - \cos q\right) \geq 0. \quad (2.3c)$$

Upshot. The behavior of solutions *within* this complete family is classified in terms of the “nonlinear mode parameter” k as follows:

$$\begin{aligned} q(t) &\text{ is purely oscillatory if } 0 < k^2 < 1, \\ q(t) &= 4 \arctan(e^{t-t_0}) \pm \pi \text{ is separatrix-like if } k^2 = 1, \\ q(t) &\text{ is periodic mod } 2\pi \text{ if } k^2 > 1. \end{aligned}$$

Remarks. Within the two-dimensional ODE, (2.3a), the single invariant (or “nonlinear mode parameter”) k is sufficient to label all qualitative behavior, including the linearized stability of the degenerate solutions $q = 0, \pm \pi$ corresponding to the critical level sets $k^2 = 0, 1$, respectively. As solutions of the sine-Gordon PDE with x -periodic boundary conditions (1.2), additional information (section 4) is required to determine the stability of each member of the family (2.3b). For this family, the linearized stability analysis is again a classical calculation [17], in which the linearized growth rate in the n th Fourier mode of wavenumber $\kappa_n = 2n\pi/L$ requires analysis of a Lamé equation for the amplitude of each mode of wavenumber κ_n in the L -periodic function space.

As we will discuss and calculate later, the IST parametrization of the family (2.3b) provides closed-form solutions equivalent to (2.3b) and provides computable linearized growth rate formulas. The IST results, however, generalize this classical single-phase example to any N -phase, x -periodic sine-Gordon solution [17].

Returning to the single-phase traveling waves, (2.2a), (2.2b), the full parametrization of these solutions is deduced from the pendulum solutions (2.3b),

$$q_1(\theta) = q_1(\kappa x + \omega t) = 2 \sin^{-1} \left[k \operatorname{sn} \left(\frac{2K(k)}{\pi} [\theta(x, t) + \theta_0]; k \right) \right], \quad (2.2c)$$

where $\theta(x, t) = \kappa x + \omega t$ is the 2π -periodic phase or angle, $U = \omega/\kappa$ is the phase velocity,

$$\theta(x, t) = \frac{\pi}{2K(k)} \frac{x + Ut}{\sqrt{U^2 - 1}}. \quad (2.2d)$$

For this discussion we will take $U^2 > 1$; $U^2 < 1$ corresponds to a rescaled inverted pendulum.

Upshot. The amplitudes of single-phase sine-Gordon solutions are determined by the invariant mode parameter k , which then fixes the wavenumber and frequency of the wavetrain in terms of “period information” on the underlying elliptic Riemann surface, that is, in terms of the complete elliptic integral $K(k)$.

From (2.2d), we find the spatial period L is given by

$$L = 4K(k)\sqrt{U^2 - 1}, \quad (2.4)$$

from which we deduce:

Fact 3. Under x -periodic boundary conditions on an interval of fixed length L , there is a two-parameter family of periodic traveling waves of x -period L . The two parameters are the invariant elliptic modulus k , which fixes the total energy, and an arbitrary phase shift $\theta_0 \in [0, 2\pi)$.

For practical purposes, these one-phase solutions may be explicitly computed using standard algorithms for Jacobi elliptic functions and elliptic integrals.

Remark. It is clear from the above formulas that any two of the three parameters $\{\kappa, \omega, H = 2k^2\}$ specifies the remaining one. As a result, we conclude that the space of all one-phase periodic s-G wavetrains of fixed x period L , $\kappa \equiv 2\pi/L \equiv \text{constant}$, has real dimension two. This two-dimensional space of L -periodic solutions may be parametrized by varying the frequency ω (which then fixes the energy), or by varying the energy H (which then fixes the frequency). Each solution for fixed κ, ω, H has a free translational parameter θ_0 .

We now describe the inverse spectral transform (IST), which reproduces this traveling wave family as well as all N -phase sine-Gordon wavetrains.

3. Inverse spectral construction of N -phase sine-Gordon wavetrains

The classical construction of one-phase periodic solutions of section 2 can be summarized in the following algorithm.

Step 1. The spatial length L is given and fixed. The “input data” is the conserved energy H , which determines the elliptic modulus, $k^2 = \frac{1}{2}H$.

Step 2. Compute $K(k)$, the complete elliptic integral of the first kind with modulus k .

Step 3. With $L, k, K(k)$ now prescribed, construct the Jacobi elliptic function $\text{sn}(z; k)$, evaluated along the real axis in the complex z -plane according to formula (2.2c). (This step guarantees the solution below will be real-valued and bounded.)

Step 4. For any $\theta_0 \in [0, 2\pi)$, the formula (2.2c) yields a computable, single-phase solution of the sine-Gordon equation with prescribed x -period and energy.

The IST construction is similar. The essential differences are:

Step 1. The IST invariants, which are the input data, consist of the elements of the conserved periodic spectrum, $\Sigma^{(P)}$, eq. (1.6), computed from the linear operator $\mathcal{L}^{(x)}$, (1.3).

Step 2. For single-phase wavetrains, in the classical construction the invariant elliptic modulus k defines an underlying Riemann surface \mathcal{R} of genus one. The complete elliptic integral $K(k)$ is simply one of two possible independent loop integrals (called *periods*) of differentials “of the first kind” (i.e., holomorphic differentials). For genus one Riemann surfaces, there is only one independent holomorphic differential, and for the purposes of integration, only two independent closed curves on \mathcal{R} . Thus, there are only two pieces of holomorphic period data: $K(k)$ is one, and the remaining holomorphic period is required to construct the elliptic function $\text{sn}(z; k)$.

In the IST construction, at step 2, we will compute all period information of holomorphic differentials on the underlying Riemann surface. Just as above, the input invariants of IST, $\Sigma^{(P)}$, will explicitly define this Riemann surface, and determine all period data.

Step 3. Given this complete set of holomorphic period data, the Riemann theta function is uniquely defined, and may then be computed. For single-phase solutions, the theta function is a function of one complex variable; for N -phase wavetrains, the appropriate theta function depends on N complex variables. The single-phase solutions $q(x, t)$ depend on x and t only through the linear phase $\theta = \kappa x + \omega t + \theta^0$, and $q(\theta)$ is 2π -periodic (mod 2π) in θ . The corresponding N -phase solutions depend on x and t only through N linear phases, $\theta_j = \kappa_j x + \omega_j t + \theta_j^0$, and $q(\theta_1, \dots, \theta_N)$ is 2π -periodic independently in each θ_j . The real-valued and bounded N -phase solutions require the theta function evaluations for real x and t along specified directions in \mathbb{C}^N [6].

Step 4. For N -phase solutions, we may take any $\theta_j^0 \in [0, 2\pi)$, $j = 1, \dots, N$, and a precise formula is numerically evaluated to generate the N -phase wavetrain whose physical characteristics (wavenumbers and frequencies) are explicitly known and determined from the input data $\Sigma^{(P)}$.

Given this preview, we now describe the IST construction of N -phase sine-Gordon wavetrains. We begin with some key ingredients and facts; the details may be found in refs. [5, 6].

3.1. Associated linear spectral problem: $\mathcal{L}^{(x)}\psi = 0$

The first ingredient is the spectrum of the linear operator $\mathcal{L}^{(x)}$, eq. (1.3), with spectral parameter E , periodic coefficients $q(x)$, eq. (1.1), and eigenfunction $\psi(x; E; q)$. The general analysis of linear operators with periodic coefficients is called *Floquet theory*. With eigenfunctions $\psi(x; E; q)$ considered for $x \in (-\infty, +\infty)$, it follows

Fact 4. The entire Floquet spectrum, Σ , of $\mathcal{L}^{(x)}$ is a continuous spectrum,

$$\Sigma \stackrel{\text{def}}{=} \{E \in \mathbb{C} \mid \mathcal{L}^{(x)}\psi(x; E; q) = 0, \psi(x) \text{ is bounded for all } x \in \mathbb{R}\}. \quad (3.1)$$

For second-order differential operators, such as $\mathcal{L}^{(x)}$, the fundamental object of Floquet theory is the *Floquet discriminant*, $\Delta(E; q)$. (Briefly, $\Delta(E; q)$ is the trace of the transfer matrix for $\mathcal{L}^{(x)}\psi = 0$.) In terms of the discriminant, the spectrum Σ of $\mathcal{L}^{(x)}$ is succinctly characterized by

Fact 5.

$$\Sigma = \{E \in \mathbb{C} \mid -2 \leq \Delta(E; q) \leq +2\}. \quad (3.2)$$

Thus, the Floquet spectrum of $\mathcal{L}^{(x)}$ consists entirely of the closure of curves in the complex E plane along which $\Delta(E; q)$ is real-valued and bounded between -2 and $+2$. This characterization of Σ will prove quite useful in our numerical computations later (section 4, with regard to linearized instability). Moreover, this formula (3.2) is precisely what is computed in the numerical DST calculations cited earlier [13–16].

The set of periodic (antiperiodic) eigenvalues of $\mathcal{L}^{(x)}$, $\Sigma^{(P)}$ in eq. (1.6), is likewise simply characterized by the discriminant:

Fact 6.

$$\Sigma^{(P)} = \{E_j \in \mathbb{C} \mid \Delta(E_j; q) = \pm 2\}. \quad (3.3)$$

From facts 5 and 6, it is easy to deduce that the endpoints of curves of continuous spectrum are special periodic (antiperiodic) eigenvalues which are not critical points of $\Delta(E)$. Generically, these *terminal points of curves of continuous spectrum are simple periodic or antiperiodic eigenvalues*, defined by

$$\begin{aligned} \Sigma^{(s)} &\equiv \text{the simple periodic, antiperiodic spectrum of } \mathcal{L}^{(x)} \\ &= \{E_j \in \mathbb{C} \mid \Delta(E_j) = \pm 2, \Delta'(E_j) \neq 0\}. \end{aligned} \quad (3.4)$$

Fact 7. The simple periodic, antiperiodic spectrum, $\Sigma^{(s)}$ in eq. (3.4), determines the entire Floquet spectrum, Σ in eq. (3.2).

Fact 7 is critical to the construction of this paper. *We shall only need to pose the simple periodic spectrum $\Sigma^{(s)}$ as our “input data”, from which the corresponding sine-Gordon solution $q(x, t)$ is specified.*

(Recall the diagram at the end of section 1. The IST solution is a map from Σ , which is determined uniquely by $\Sigma^{(s)}$, to $q(x, t)$.)

The IST ingredients and facts to be provided in the remainder of this section are:

- (a) symmetries and properties of $\Sigma^{(p)}$, in facts 8, 9;
- (b) a precise characterization of those $\Sigma^{(s)} = \Sigma_N^{(s)}$ which correspond to N -phase s-G solutions, in section 3.2;
- (c) the Riemann surface \mathcal{R} defined by $\Sigma_N^{(s)}$ and all necessary period information on \mathcal{R} , in section 3.3, step 2;
- (d) the theta function representation of $q_N(x, t) = q_N(\theta_1, \dots, \theta_N)$ corresponding to the prescribed simple periodic spectrum $\Sigma_N^{(s)}$, in section 3.3, steps 3 and 4.

Fact 8. The entire positive real axis in the complex E plane is continuous spectrum, and $E = 0, \infty$ are limit points of positive real sequences in $\Sigma^{(p)}/\Sigma^{(s)}$, with

$$-2 \leq \Delta(E) \leq +2 \quad \text{for all } 0 < E < \infty. \quad (3.5)$$

It follows immediately from fact 8 that all $E_j \in \Sigma^{(p)} \cap \mathbb{R}^+$ must be critical points of $\Delta(E)$: $\Delta(E_j) = \pm 2$, and the first nonvanishing derivative of Δ at $E = E_j$ must be even, $\Delta'(E_j) = \dots = \Delta^{(2j-1)}(E_j) = 0$, $\Delta^{(2j)}(E_j) \neq 0$ for some $j \geq 1$. (Otherwise, there must be “gaps” in the continuous spectrum on \mathbb{R}^+ , contrary to fact 8.) All periodic and antiperiodic eigenvalues E_j for which $\Delta(E_j)$ also has zero derivatives up to order $k-1$ at E_j , $\Delta'(E_j) = \dots = \Delta^{(k-1)}(E_j) = 0$, $\Delta^{(k)}(E_j) \neq 0$, $k \geq 2$, are called k th-order multiple (anti) periodic eigenvalues. Generically, the multiple points in $\Sigma^{(p)}$ are *double points*, E_j^d , and we denote the set of all double (anti) periodic eigenvalues by $\Sigma^{(d)}$,

$$\Sigma^{(d)} \equiv \{E_j^d \in \mathbb{C} \mid \Delta(E_j^d) = \pm 2, \Delta'(E_j^d) = 0, \Delta''(E_j^d) \neq 0\}. \quad (3.6)$$

In reference to fact 8, $E = 0$ and ∞ are in fact limit points of countably infinite positive real sequences in $\Sigma^{(d)}$.

Remark. The non-real elements of $\Sigma^{(d)}$, which are determined by $\Sigma^{(s)}$ (fact 7), play a fundamental role in characterizing all possible instabilities of the periodic sine-Gordon solution determined by $\Sigma^{(s)}$. We elaborate on this connection in section 4.

Fact 9. The simple (anti) periodic spectrum $\Sigma^{(s)}$ consists of pairs, $E_{2j-1} \neq E_{2j}$, which *either* are negative real *or* occur in complex conjugate pairs, the asterisk denotes the complex conjugate,

$$\Sigma^{(s)} = \left\{ (E_{2j-1}, E_{2j}) \mid E_{2j-1} < E_{2j} < 0 \text{ or } E_{2j-1}^* = E_{2j}, E_{2j-1} \neq E_{2j} \right\}. \quad (3.7)$$

Fact 10. The main geometric distinction between simple periodic points $E_j \in \Sigma^{(s)}$ and double periodic points $E_j^d \in \Sigma^{(d)}$ is that curves of continuous spectrum terminate at $E_j \in \Sigma^{(s)}$ whereas all double periodic points E_j^d are embedded inside curves of spectrum. (Isolated double points $E_j^d \in \mathbb{R}^-$ may occur.)

Remark. In addition to $E = 0, \infty$ (fact 8), the elements of $\Sigma^{(s)}$ yield endpoints of curves of continuous spectrum for the operator $\mathcal{L}^{(x)}$. Additional terminal points of spectral curves occur at all odd order

multiple (anti) periodic points of order $k \geq 3$, but the corresponding Riemann surfaces are singular. For this reason, we shall assume that $0, \infty$ and elements of $\Sigma^{(s)}$ are the only endpoints of curves of spectrum for $\mathcal{L}^{(x)}$.

With this general information, we can now proceed to the specific choices of $\Sigma^{(s)}$ which lead to N -phase wavetrains $q(x, t)$.

3.2. N -phase inverse spectral solutions: general properties

It is a remarkable fact that N -phase s-G wavetrains are specified by those $\Sigma^{(s)}$, (3.7), consisting of N pairs of elements.

Theorem 3.1. Suppose the linear differential operator $\mathcal{L}^{(x)}$, eq. (1.3), has a simple periodic spectrum, $\Sigma^{(s)}$, eq. (3.4), consisting of exactly $N < \infty$ distinct pairs,

$$\Sigma^{(s)} = \Sigma_N^{(s)} = \{E_1, \dots, E_{2N} \mid E_{2j-1} < E_{2j} < 0 \text{ or } E_{2j-1}^* = E_{2j}, E_j \text{ all distinct}\}. \quad (3.8)$$

Then there exist real coefficients $(q(x, t), q_t(x, t))$ of $\mathcal{L}^{(x)}$ that: (a) satisfy the sine-Gordon PDE (1.5), (b) satisfy the x -periodic boundary conditions (1.2) with fixed period L , and (c) may be explicitly reconstructed from $\Sigma_N^{(s)}$ in the form of an N -phase wavetrain,

$$q(x, t; \Sigma_N^{(s)}) = q_N(\theta_1, \dots, \theta_N), \quad (3.9a)$$

$$\theta_j = \kappa_j x + \omega_j t + \theta_j^0, \quad \theta_j^0 \in [0, 2\pi), \quad (3.9b)$$

$$q_N(\theta_1, \dots, \theta_j + 2\pi, \dots, \theta_N) = q_N(\theta_1, \dots, \theta_j, \dots, \theta_N) \pmod{2\pi} \quad (3.9c)$$

$$\kappa_j = 2\pi n_j / L, \quad j = 1, \dots, N, \quad \text{for some } n_j \in \mathbb{Z}, \quad (3.9d)$$

where the wavenumbers κ_j and frequencies ω_j , $j = 1, \dots, N$, are explicit functions of $\Sigma_N^{(s)}$.

Remark. The explicit formulas for κ_j , ω_j , $j = 1, \dots, N$, and $q_N(x, t)$, are given below in section 3.3.

Remark. The set $\Sigma_N^{(s)}$, (3.8), has real dimension $2N$. For a given fixed period L , however, the periodicity constraints (3.9d) place N real conditions on $\Sigma_N^{(s)}$, so that the subsets of $\Sigma_N^{(s)}$ corresponding to fixed period L have real dimension N .

The corresponding family of N -phase solutions $q(x, t; \Sigma_N^{(s)})$ of x -period L are in general quasiperiodic in t , since the N frequencies ω_j , $j = 1, \dots, N$, are in general incommensurate. This L -periodic family is parametrized either by the N -dimensional L -periodic subsets of $\Sigma_N^{(s)}$ or by the N frequencies $\omega_1, \dots, \omega_N$. Each member of this family, corresponding to fixed $\omega_1, \dots, \omega_N$ for example, also depends on N arbitrary phases $\theta_j^0 \in [0, \pi)$, $j = 1, \dots, N$.

Caution. For arbitrary sets $\Sigma_N^{(s)}$, (3.8), which fail to satisfy the periodicity constraints (3.9d), then $\Sigma_N^{(s)}$ is not a bona fide periodic spectrum of $\mathcal{L}^{(x)}$. Nonetheless, the construction outlined below generates an N -phase s-G wavetrain which is quasiperiodic in x and t . A fundamental obstruction in the IST solution method arises when one demands periodicity in x of period L for $N \geq 2$. In effect, one must search the $2N$ -dimensional space of all $\Sigma_N^{(s)}$, (3.8), for the N -dimensional subspace of $\Sigma_N^{(s)}$ which satisfies the

N -periodicity constraints (3.9d). As we will display below, these constraints (3.9d), $\kappa_j(\Sigma_N^{(s)}) \equiv 2\pi n_j/L$, $j = 1, \dots, N$, for every choice $\{n_1, \dots, n_N\}$ of N integers, consist of N transcendental equations in $2N$ variables. Each fixed set $\{n_1, \dots, n_N\}$ corresponds to one N -dimensional component of L -periodic N -phase solutions and the union of all N -dimensional subsets $\Sigma_N^{(s)}$ corresponding to fixed $\{n_1, \dots, n_N\}$ is undoubtedly dense in the $2N$ -dimensional space of all $\Sigma_N^{(s)}$, (3.8).

While the situation may seem hopeless, in section 6 we shall illustrate how to exploit symmetries in $\Sigma_N^{(s)}$ which guarantee periodicity when $N = 2$. In this way, we shall be able to pose IST input data, $\Sigma_{N=2}^{(s)}$, which guarantees periodicity in x with either $n_1 = \pm n_2 = 1$ or $n_1 = 1, n_2 = 0$ in (3.9d). All other periodic subsets of $\Sigma_2^{(s)}$ corresponding to a fixed choice $\kappa_1 = n_1 2\pi/L$, $\kappa_2 = n_2 2\pi/L$, $n_1, n_2 \in \mathbb{Z}$, may be individually determined through intensive numerical calculations. We provide one such example for $n_1 = 1, n_2 = 2$ in section 6. In section 7 we give some three-phase examples. For $N > 3$ the calculation seems formidable except through special symmetries.

Remark. As mentioned above in the previous remark, the need to search the N -dimensional subspace of \mathbb{R}^{2N} defined by the fixed length conditions (3.9d) is the crucial obstruction to the IST algorithm. An appealing possibility exists for generating connected components of $\Sigma_N^{(s)}$ for fixed length L . The x -periodic N -phase modulation equations of the perturbed sine-Gordon equation [12] preserve spatial length. These ODEs are flows on $\Sigma_N^{(s)}$, whose ratios are independent of the perturbation. Thus we may be able to use one L -periodic element of $\Sigma_N^{(s)}$ (corresponding to fixed n_1, \dots, n_N in (3.9d)) as initial data in the modulation ODEs and then numerically integrate to find additional L -periodic elements of $\Sigma_N^{(s)}$.

Remark. There is no fundamental obstruction if one is content with N -phase wavetrains that are quasiperiodic in x and t . The IST construction described below applies for any choice of $\Sigma_N^{(s)}$, (3.8), and yields an N -phase s-G solution quasiperiodic in x and t . The real $2N$ -dimensional family $\Sigma_N^{(s)}$ is explicitly related to the set $\{\kappa_j, \omega_j, j = 1, \dots, N\}$ of real wavenumbers and frequencies via the transcendental formulas (3.21).

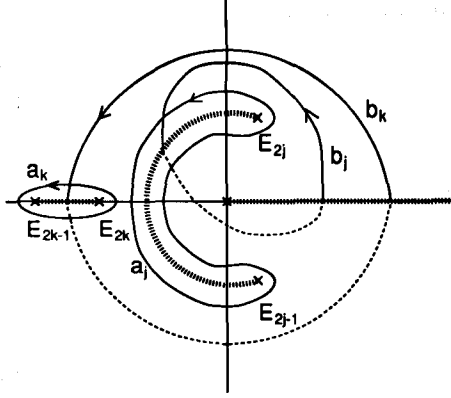
Remark. The solutions (3.9), and more explicitly (3.19) below, may not represent all L -periodic functions of x with a prescribed simple periodic spectrum $\Sigma_N^{(s)}$, (3.8), satisfying the fixed period constraints (3.9d). There may be additional s-G solutions \hat{q}_N with the same $\Sigma_N^{(s)}$ which are L -periodic in x but depend upon a finite number of additional degrees of freedom, and where \hat{q}_N is either "homoclinic" or oscillatory as a function of t in each additional L -periodic spatial mode. (Refer to ref. [17] for details.) These homoclinic degrees of freedom exist for each linear instability of the t -quasiperiodic, x -periodic solution q_N , (3.9). While we will not compute homoclinic solutions in this paper, we will detect their existence in section 4 and then near-homoclinic limits are illustrated in section 7.

3.3. N -phase inverse spectral solutions: explicitly construction from $\Sigma_N^{(s)}$

The algorithm parallels steps 1–4 of the classical single-phase construction listed at the start of section 3.

Step 1. Choose the fixed spatial length L , and choose the simple periodic spectrum

$$\Sigma_N^{(s)} = \{E_j, j = 1, \dots, 2N \mid E_{2j-1} < E_{2j} < 0 \text{ or } E_{2j-1}^* = E_{2j}\}.$$

Fig. 1. Canonical a and b cycles on \mathcal{R} .

(We assume that $\Sigma_N^{(s)}$ meets the fixed period constraints (3.9d). These constraints will be verified in step 3.)

Step 2. Compute all period information for differentials of the first kind on the hyperelliptic Riemann surface \mathcal{R} determined by $\Sigma_N^{(s)}$.

Define a Riemann surface \mathcal{R} of genus N from $\Sigma_N^{(s)}$ as follows:

$$\mathcal{R} = \left\{ (E, R(E)) \mid R^2(E) = E \prod_{j=1}^{2N} (E - E_j) \right\}. \quad (3.10)$$

The simple periodic, antiperiodic eigenvalues E_j , $j = 1, \dots, 2N$, plus $0, \infty$, are the branch points of \mathcal{R} . The branch cuts and choice of canonical basis of closed one-cycles on \mathcal{R} , $\{a_j, b_j\}_{j=1}^N$, are depicted in fig. 1. (This choice conforms to ref. [6].) The solid paths indicate the upper sheet of \mathcal{R} while the dashed paths indicate the lower sheet. The thick dotted curves indicate the branch cuts.

A basis of differentials of the first kind, or holomorphic differentials, is

$$\phi_k = \frac{E^{k-1} dE}{R(E)}, \quad k = 1, \dots, N. \quad (3.11)$$

The period information for $\{\phi_k\}$ consists of the $2N^2$ integrals around the basis $\{a_j, b_j\}_{j=1}^N$ of closed cycles on \mathcal{R} ,

$$\left\{ \oint_{a_j} \phi_k, \oint_{b_j} \phi_k; j, k = 1, \dots, N \right\}. \quad (3.12)$$

This period information is computed as follows. We define a *normalized basis of holomorphic differentials*, $\{\psi_i\}_{i=1}^N$,

$$\psi_i = \sum_{j=1}^N C_{ij} E^{N-j} \frac{dE}{R(E)}, \quad i = 1, \dots, N, \quad (3.13a)$$

where the N^2 normalization constants C_{ij} are uniquely specified by the N^2 conditions

$$\oint_{a_k} \psi_i = \delta_{ik} = 0 \quad \text{for } i \neq k \quad \text{or} \quad 1 \quad \text{for } i = k, \quad i, k = 1, \dots, N. \quad (3.13b)$$

The N column vectors of a_k periods of $\psi = (\psi_1, \dots, \psi_N)^T$, by (3.13b), consist of the unit orthogonal vectors in \mathbb{C}^N ,

$$e_k = \oint_{a_k} \psi, \quad (3.13c)$$

$$(e_k)_i = \delta_{ik}. \quad (3.13d)$$

The “period matrix” (or Riemann matrix), $B_{N \times N}$, of \mathcal{R} is defined by

$$B_{ij} = \oint_{b_i} \psi_j. \quad (3.14a)$$

The columns of B are denoted by

$$B_j = \oint_{b_j} \psi. \quad (3.14b)$$

The normalized period matrix B has two important properties:

(i) B is symmetric,

$$B_{ij} = B_{ji}. \quad (3.15a)$$

(ii) The imaginary part of B is positive definite,

$$\langle \text{Im}(B)V, V \rangle > 0 \quad \text{for } V \neq 0. \quad (3.15b)$$

Upshot. The complete holomorphic period information (i.e., a complete set of periods for a basis of holomorphic differentials) is contained in $\{C_{ij}, B_{ij}\}_{i,j=1}^N$, which are explicit functions of the branch points $\{E_j\}_{j=1}^{2N} = \Sigma_N^{(s)}$.

Step 3. Construct the Riemann theta function of N variables, $\Theta(z; B)$, from the $N \times N$ period matrix B on the Riemann surface \mathcal{R} , (3.10).

The Riemann theta function, $\Theta(z; B)$, is an entire function of N complex variables $z \in \mathbb{C}^N$ constructed from the period matrix B , (3.14), on \mathcal{R} by the formula

$$\Theta(z; B) = \sum_{k \in \mathbb{Z}^N} \exp[i\pi(\langle Bk, k \rangle + 2\langle z, k \rangle)]. \quad (3.16)$$

The values of Θ in one fundamental domain (a paralleliped in \mathbb{C}^N spanned by $e_1, \dots, e_N, B_1, \dots, B_N$)

suffice to give values on all of \mathbb{C}^N by virtue of the automorphic ("periodicity") properties [18]:

$$\Theta(z + \Lambda_{n,m}; B) = \exp[-i\pi(\langle Bm, m \rangle + 2\langle z, m \rangle)] \Theta(z; B), \quad (3.17a)$$

where $\Lambda_{n,m}$ is any lattice element

$$\Lambda_{n,m} = \sum_{i=1}^N n_i e_i + m_i B_i, \quad n, m \in \mathbb{Z}^N. \quad (3.17b)$$

In turn, the formulas (3.16), (3.17) indicate that ratios of theta functions are the basis for meromorphic functions on \mathbb{C}^N with period $\Lambda_{n,m}$, (3.17b). Thus ratios of theta functions are meromorphic functions on the Jacobian of \mathcal{R} , $\text{Jac}(\mathcal{R})$, defined by

$$z \in \text{Jac}(\mathcal{R}) = \mathbb{C}^N / \Lambda, \quad \Lambda = \{e_1, \dots, e_N, B_1, \dots, B_N\}. \quad (3.18)$$

Remark. Since $\text{Im}(B)$ is positive definite, (3.15b), the definition (3.16) indicates absolute convergence of this multiple Fourier series.

Step 4. Compute the N -phase theta function solution of sine-Gordon with the prescribed spectrum $\Sigma_N^{(s)}$.

The explicit N -phase theta-function solutions $q_N(x, t)$ of the sine-Gordon equation are [6]

$$q_N(x, t) = i \ln \left(\frac{\Theta^2(l(x, t) + \frac{1}{2}; B)}{\Theta^2(l(x, t); B)} \right), \quad (3.19a)$$

where

$$\frac{1}{2} \equiv (\frac{1}{2}, \dots, \frac{1}{2}) \in \mathbb{R}^N, \quad (3.19b)$$

B is the $N \times N$ period matrix on \mathcal{R} , (3.14), l is the complex N -phase vector linear in x and t whose entries, modulo phase shifts and constant term, are fixed by $\Sigma_N^{(s)} = \{E_j\}_1^{2N}$,

$$l_j(x, t) = -2i \left[\left(C_{j1} + \frac{(-1)^{m+1} C_{jN}}{16\sqrt{\prod_1^{2N} E_k}} \right) x + \left(C_{j1} + \frac{(-1)^m C_{jN}}{16\sqrt{\prod_1^{2N} E_k}} \right) t \right] + l_j^0. \quad (3.19c)$$

The integer $m = 0$ or 1 is related to the strict or mod 2π periodicity in x of q_N (see the last remark of this section), the complex phase shifts l_j^0 will be detailed below, eq. (3.23), and the C_{jk} are the holomorphic normalization constants on \mathcal{R} , (3.13).

We emphasize here that, except for the discrete choice $m = 0$ or 1 and the complex phase shifts l_j^0 , the N -phase formula (3.19) specifies $q_N(x, t)$ uniquely as a function of the spectral parameters $\{E_j\}_{j=1}^{2N} = \Sigma_N^{(s)}$. The freedom of choice of m and l_0 appears below.

The real physical wavenumbers κ_j and frequencies ω_j , and thereby the real phases θ_j , $j = 1, \dots, N$, and phase shifts θ_j^0 , are deduced from (3.19) by symmetries on \mathcal{R} inherited from the symmetries of $\Sigma_N^{(s)}$, (3.8):

$$E_{2j-1} < E_{2j} < 0 \quad \text{or} \quad E_{2j}^* = E_{2j-1}. \quad (3.20a)$$

With the a_j, b_j cycles as depicted in fig. 1, it follows that [6]

$$\operatorname{Im}(C_{ij}) = 0 \quad \forall i, j, \quad (3.20b)$$

$$\operatorname{Re}(B_{ij}) = 0, \quad i \neq j, \quad (3.20c)$$

$$\operatorname{Re}(B_{jj}) = 0 \quad \text{if } E_{2j-1} < E_{2j} < 0, \quad \operatorname{Re}(B_{ij}) = \frac{1}{2} \quad \text{if } E_{2j-1}^* = E_{2j}. \quad (3.20d)$$

The symmetries imply, from (3.19c),

$$\operatorname{Re}(l(x, t) - l_0) = 0. \quad (3.20e)$$

These properties provide a basis for the real s-G flows, $l(x, t) - l_0$, with coefficients in \mathbb{R} , where the basis elements are in the span of the period lattice Λ . The real coefficients in this expansion yield the real angles:

$$l(x, t) - l_0 = \sum_{j=1}^N \frac{\theta_j}{2\pi} f_j, \quad (3.21a)$$

$$\theta_j(x, t) = \kappa_j x + \omega_j t, \quad (3.21b)$$

$$f_j = B_j \quad \text{if } E_{2j-1} < E_{2j} < 0, \quad f_j = e_j - 2B_j \quad \text{if } E_{2j-1}^* = E_{2j}. \quad (3.21c)$$

If we let $F_{N \times N} = [f_1 \dots f_N]$, then the real angles, wavenumbers and frequencies are explicitly given by

$$\theta = 2\pi F^{-1}(l - l_0), \quad (3.21d)$$

$$\kappa = 4\pi i F^{-1} \left(C_1 + \frac{(-1)^{m+1} C_N}{16\sqrt{\prod_1^{2N} E_j}} \right), \quad (3.21e)$$

$$\omega = 4\pi i F^{-1} \left(C_1 + \frac{(-1)^m C_N}{16\sqrt{\prod_1^{2N} E_j}} \right), \quad (3.21f)$$

where

$$(C_1)_j = C_{j1}, \quad (C_N)_j = C_{jN}. \quad (3.21g)$$

From the symmetries (3.20), it follows that the f_j are purely imaginary, C_1, C_N are real, and thus the phase θ , wavenumbers κ , and frequencies ω are real. The periodicity properties of $q_N(x, t)$, (3.19), with respect to the phases θ are [6]

$$\begin{aligned} q_N(\theta_1, \dots, \theta_j + 2\pi, \dots, \theta_N) &= q_N(\theta_1, \dots, \theta_j, \dots, \theta_N) & \text{if } E_{2j-1}^* = E_{2j}, \\ &= q_N(\theta_1, \dots, \theta_j, \dots, \theta_N) \pm 2\pi & \text{if } E_{2j-1} < E_{2j} < 0. \end{aligned} \quad (3.22)$$

The final ingredient in this algorithm is the constant vector l_0 . The proper choice of l_0 which ensures that $q_N(x, t)$ is real-valued and bounded for real x and t is [6]

$$\operatorname{Re}[(l_0)_j] = 0 \quad \text{if } E_{2j-1}^* = E_{2j}, \quad \operatorname{Re}[(l_0)_j] = \pm \frac{1}{4} \quad \text{if } E_{2j-1} < E_{2j} < 0, \quad (3.23a)$$

$$\operatorname{Im}[l_0] = \sum_{k=1}^N f_k \theta_k^0, \quad \theta_k^0 \in [0, 2\pi), \quad k = 1, \dots, N, \quad (3.23b)$$

where the constants θ_k^0 , $k = 1, \dots, N$ are the N real phase shifts.

Remark. From (3.22), (3.23a) each complex conjugate pair $E_{2j-1}^* = E_{2j}$ in $\Sigma_N^{(s)}$ corresponds to a strictly periodic phase, θ_j , or “breather” degree of freedom, whereas each negative real pair $E_{2j-1} < E_{2j} < 0$ in $\Sigma_N^{(s)}$ corresponds to a “kink” degree of freedom (q_N increases by 2π as θ_j increases by 2π) if $\operatorname{Re}(l_0)_j = \frac{1}{4}$ and an “antikink” mode (q_N decreases by 2π as θ_j increases by 2π) if $\operatorname{Re}(l_0)_j = -\frac{1}{4}$.

Remark. The discrete parameter, $m = 0$ or 1 , in the N -phase solution formulas (3.19c), (3.21e), (3.21f) reflects a discrete symmetry of the sine-Gordon equation,

$$(q, x, t) \rightarrow (q + \pi, t, x),$$

in which the roles of x and t are reversed. Note that the operators $\mathcal{L}^{(x)}$, $\mathcal{L}^{(t)}$, (1.3), (1.4), are interchanged by this transformation. For the more general class of solutions q_N quasiperiodic in x and t , each choice of m may be taken with an arbitrary $\Sigma_N^{(s)}$ subject only to the constraints (3.20a). For x -periodic solutions of fixed period L , one must pick the “charge” m , which fixes κ and ω by (3.21e), (3.21f) then search the $2N$ -dimensional space $\Sigma_N^{(s)} = \{E_j\}_1^{2N}$, satisfying (3.20a), for elements of the N -dimensional subspace defined by (3.9d), $\kappa = n 2\pi/L$, for each $n \in \mathbb{Z}^N$. Either choice of m may yield a valid simple periodic spectrum $\Sigma_N^{(s)}$ of (1.3).

Before proceeding to numerically implement the ingredients and steps outlined above, we shall describe in section 4 those ingredients computed from the simple periodic spectrum $\Sigma_N^{(s)}$ which are necessary to label and compute all linearized instabilities of the x -periodic, N -phase solution q_N determined by $\Sigma_N^{(s)}$.

4. Nonlinear mode labelling via Hochstadt’s formula for the Floquet discriminant

An N -phase L -periodic solution $q_N(x, t)$ consists of N interacting nonlinear spatial modes; each phase with wavenumber $\kappa_j = n_j 2\pi/L$ represents one element of the function space $\mathcal{F}^{(L)}$, defined below eq. (1.2), for which q_N has nonzero projection. Since $\mathcal{F}^{(L)}$ is infinite-dimensional, there are infinitely many directions in $\mathcal{F}^{(L)}$ for which q_N has zero projection. Whereas the N pairs of simple periodic eigenvalues label the N “open” degrees of freedom of q_N , the $\infty - N$ “closed” or inactive degrees of freedom in the solution $q_N \in \mathcal{F}^{(L)}$ are explicitly labelled by the pairs of double periodic eigenvalues of (1.3), E_j^d . Refer to ref. [17] for rigorous details of this section. The double periodic spectrum, $\Sigma^{(d)}$, is

defined from the Floquet discriminant of (1.3) by (3.6),

$$\Sigma^{(d)} = \{E_j^d \in \mathbb{C} \mid \Delta(E_j^d) = \pm 2, \Delta'(E_j^d) = 0, \Delta''(E_j^d) \neq 0\}. \quad (4.1)$$

Heuristically, each double periodic eigenvalue should be thought of as a pair of simple periodic spectra which have coalesced thereby restricting a potentially active mode.

In the linearized stability analysis of $q_N(x, t)$, it is shown in ref. [17] that q_N is linearly unstable to small perturbations in $\mathcal{F}^{(L)}$ of wavenumber κ_p only if the corresponding p th pair of double periodic eigenvalues, E_{2p-1}^d, E_{2p}^d , is nonreal. Thus, to determine the number of linearly unstable modes in $\mathcal{F}^{(L)}$ associated to the solution q_N , one only has to find the number of pairs of complex conjugate double periodic eigenvalues and compute the corresponding growth rates.

The calculation of non-real double periodic eigenvalues and the corresponding growth rates is now outlined.

The simple periodic spectrum $\Sigma^{(s)} = \{E_j\}_{j=1}^{2N}$ explicitly determines the double periodic spectrum (in fact, the entire continuous spectrum of (1.3)) by Hochstadt's formula [2]

$$\Delta(E; q_N) = \Delta(E; \Sigma_N^{(s)}) = 2 \cos \left(L \int_{E_0}^E \Omega_N^{(x)} \right), \quad (4.2)$$

where E_0 is one of the simple periodic eigenvalues, L is the x -period length, and $\Omega_N^{(x)}$ is the following meromorphic differential on \mathcal{R} uniquely specified by $\Sigma_N^{(s)}$ [17]:

$$\Omega_N^{(x)} = -\frac{1}{2} \left(E^{N+1} - \beta_N^{(x)} E^N - \dots - \beta_1^{(x)} E - \frac{(-1)^m \sqrt{\prod_1^{2N} E_j}}{16} \right) \frac{dE}{ER(E)}, \quad (4.3a)$$

$$\oint_{\mu_k \text{ cycle}} \Omega_N^{(x)} = 0, \quad k = 1, \dots, N, \quad (4.3b)$$

where [6]

$$\begin{aligned} \mu_k \text{ cycle} &\sim a_k - 2b_k && \text{if } E_{2k-1}^* = E_{2k}, \\ &\sim b_k && \text{if } E_{2k-1} < E_{2k} < 0. \end{aligned} \quad (4.3c)$$

Companion to $\Omega_N^{(x)}$ is another meromorphic differential, $\Omega_N^{(t)}$, also uniquely specified by $\Sigma_N^{(s)}$,

$$\Omega_N^{(t)} = -\frac{1}{2} \left(E^{N+1} - \beta_N^{(t)} E^N - \dots - \beta_1^{(t)} E - \frac{(-1)^{m+1} \sqrt{\prod_1^{2N} E_j}}{16} \right) \frac{dE}{ER(E)}, \quad (4.4a)$$

$$\oint_{\mu_k} \Omega_N^{(t)} = 0, \quad k = 1, \dots, N, \quad \mu_k \text{ cycles as in (4.3c)}. \quad (4.4b)$$

Whereas $\Omega_N^{(x)}$ will be used to identify nonreal pairs of double points E_{2p-1}^d, E_{2p}^d and thus all potential linearly unstable modes of wavenumber κ_p in $\mathcal{F}^{(L)}$ associated to $q_N(x, t)$, the differential $\Omega_N^{(t)}$ will then be

used to compute the linearized growth rate $\sigma(\kappa_p)$ in the unstable direction(s) [17]:

$$\sigma(\kappa_p) = \text{Im} \int_{E_{2p-1}^d}^{E_{2p}^d} \Omega_N^{(t)}. \quad (4.5)$$

Remarks

The differentials $\Omega_N^{(x)}, \Omega_N^{(t)}$ reflect fundamental properties of solutions $q_N(x, t)$ generated by *IST* from this prescribed simple periodic spectrum $\Sigma_N^{(s)} = \{E_k\}_{k=1}^{2N}$. These differentials will be computed in order to determine:

- (a) the curves of continuous spectrum of $\mathcal{L}^{(x)}$ for given $\Sigma_N^{(s)}$ (recall facts 2, 7);
- (b) the number of unstable modes associated to $q_N(x, t)$ and their linear growth rates.

$\Omega_N^{(x)}$ and $\Omega_N^{(t)}$ also provide independent numerical checks on the computation of the wavenumbers κ_j and frequencies ω_j . Riemann bilinear identities yield alternative formulas to (3.21e), (3.21f) [19]:

$$\kappa_j = \oint_{\nu_j} \Omega_N^{(x)}, \quad (4.6a)$$

$$\omega_j = \oint_{\nu_j} \Omega_N^{(t)}, \quad (4.6b)$$

where

$$\nu_j \sim a_j \quad \text{if } E_{2j-1} < E_{2j} < 0, \quad \nu_j \sim b_j \quad \text{if } E_{2j-1}^* = E_{2j}. \quad (4.6c)$$

The differentials $\Omega_N^{(x)}, \Omega_N^{(t)}$ are the fundamental objects in the modulation equations of an N -phase wavetrain $q_N(x, t)$ [19, 20]. Thus, these calculations will be necessary in any numerical simulation of N -phase modulation theory.

5. Numerical inverse spectral solutions: $N = 1$

We now implement steps 1 through 4 of section 3 and display several one-phase sine-Gordon wavetrains by the inverse spectral algorithm (in contrast to the classical construction of section 2). We also compute, following section 4, (a) the entire continuous spectrum (3.1) of linear system (1.3) with potentials (q, q_t) given by these single-phase solutions, (b) all potential linearly unstable modes of these solutions, and (c) the linearized growth rate in each unstable mode.

Step 1. Choose

$$\Sigma_{N=1}^{(s)} = \{E_1, E_2 \mid E_1 < E_2 < 0 \text{ or } E_1^* = E_2, E_1 \neq E_2\}. \quad (5.1)$$

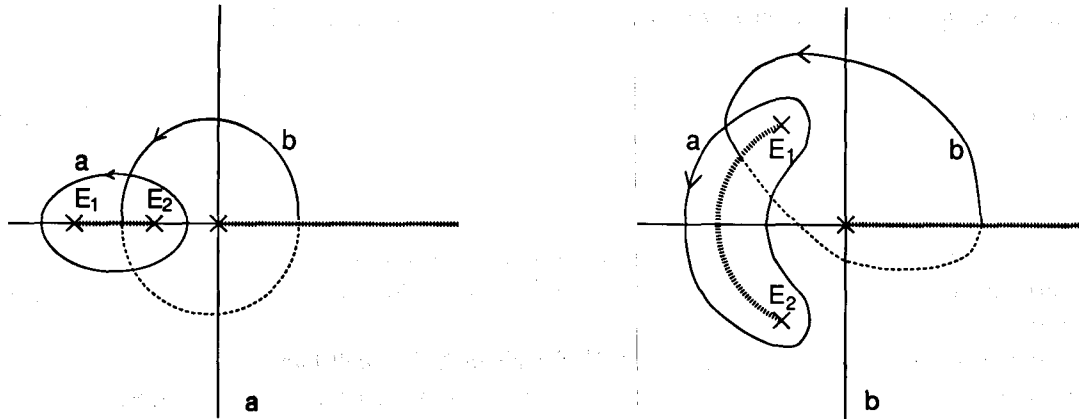


Fig. 2. Canonical a and b cycles, $N = 1$: (a) for $E_1 < E_2 < 0$, and (b) for $E_1 = E_2^*$.

Since there is only one 2π -periodic phase, thus one wavenumber κ_1 and one frequency ω_1 , any choice of $\Sigma_{N=1}^{(s)}$ yields an x -periodic and t -periodic solution. Later we will generate one-dimensional curves in $\Sigma_{N=1}^{(s)}$ corresponding to fixed x -period, $\kappa(E_1, E_2) \equiv \text{constant}$, and fixed t -period, $\omega(E_1, E_2) \equiv \text{constant}$. If $\kappa = 0$ or $\omega = 0$, the x - or t -periods are arbitrary.

Step 2. Compute all period information on the elliptic Riemann surface, \mathcal{R} ,

$$\mathcal{R} = \{(E, R(E)) | R^2(E) = E(E - E_1)(E - E_2)\}. \quad (5.2)$$

From the branch cut convention in fig. 1, the two classes of $\Sigma_{N=1}^{(s)}$ are depicted in fig. 2, along with the canonical a, b cycles.

By virtue of the symmetries in $\Sigma_{N=1}^{(s)}$ (invariance under complex conjugation) and the inherited symmetry in the a, b cycles in fig. 2, the path integrals of basic differentials on \mathcal{R} of the form $E^j dE/R(E)$ may be tremendously simplified for numerical computations. With curves $\alpha, \beta, \gamma, \beta_1, \gamma_1$ as depicted in fig. 3, with x_1, y_1, x'_1 arbitrary, the numerical computations of a, b cycles for all differentials

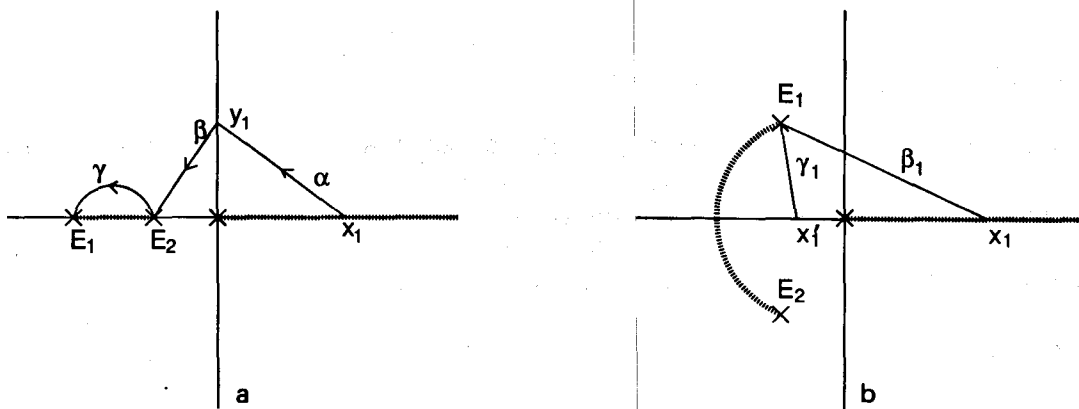


Fig. 3. Parametrized paths for numerical computation of a and b cycles, $N = 1$.

$E^j dE/R(E)$ simplify to

Case 1. $E_1 < E_2 < 0$. For $j = -1, 0, 1$,

$$\oint_a \frac{E^j dE}{R(E)} = 2 \operatorname{Re} \left(\int_{\gamma} \frac{E^j dE}{R(E)} \right), \quad (5.3a)$$

$$\oint_b \frac{E^j dE}{R(E)} = 2i \operatorname{Im} \left(\int_{\alpha+\beta} \frac{E^j dE}{R(E)} \right). \quad (5.3b)$$

Case 2. $E_1^* = E_2$. For $j = -1, 0, 1$,

$$\oint_a \frac{E^j dE}{R(E)} = 4 \operatorname{Re} \left(\int_{\gamma_1} \frac{E^j dE}{R(E)} \right), \quad (5.4a)$$

$$\oint_b \frac{E^j dE}{R(E)} = 2 \operatorname{Re} \left(\int_{\gamma_1} \frac{E^j dE}{R(E)} \right) + 2i \operatorname{Im} \left(\int_{\beta_1} \frac{E^j dE}{R(E)} \right). \quad (5.4b)$$

Remark. These closed path integrals are independent of the choice of $x_1 > 0$, $y_1 > 0$, $x'_1 < 0$, which we exploit to check the numerical computations by picking at least two choices of these parameters for each calculation.

The holomorphic period data only involves $j = 0$ in (5.3), (5.4), which provides the normalization constant C_{11} , (3.13), and period “matrix” B_{11} , (3.14). We compute the meromorphic period data, $j = -1, 1$ in (5.3), (5.4), in order to construct the meromorphic differentials $\Omega^{(x)}, \Omega^{(t)}$, eqs. (4.3), (4.4).

Step 3. Construct the Riemann theta function of $N = 1$ variable.

The Riemann theta function, $\Theta(z, B)$, for elliptic curves (5.2) is (with $B = B_{11}$)

$$\Theta(z; B) = \sum_{k \in \mathbb{Z}} \exp[i\pi(Bk^2 + 2zk)]. \quad (5.5)$$

For the two classes of genus one curves of interest here, the period “matrix” B takes the explicit form (recall (3.20))

$$B = i \operatorname{Im}(B) \quad E_1 < E_2 < 0, \quad B = \frac{1}{2} + i \operatorname{Im}(B) \quad E_1^* = E_2, \quad (5.6)$$

with $\operatorname{Im}(B) > 0$ in both cases.

Step 4. The real sine-Gordon theta function solutions (3.19), with $N = 1$, are evaluated along $z = l$ and

$z = l + \frac{1}{2}$, with $l(x, t)$ given explicitly by (3.19), (3.21), (3.23), which yield

$$l(x, t) = -2i C_{11} \left[\left(1 + \frac{(-1)^{m+1}}{16\sqrt{E_1 E_2}} \right) x + \left(1 + \frac{(-1)^m}{16\sqrt{E_1 E_2}} \right) t \right] + l_0, \quad (5.7)$$

$$\begin{aligned} &= (\theta_1 + \theta_1^0) B / 2\pi \pm \frac{1}{4} \quad E_1 < E_2 < 0, \\ &= (\theta_1 + \theta_1^0)(1 - 2B) \quad E_1^* = E_2. \end{aligned} \quad (5.8a)$$

$$C_{11} = \left(\oint_a \frac{dE}{R(E)} \right)^{-1}, \quad R^2(E) = E(E - E_1)(E - E_2), \quad (5.8b)$$

$$\theta_1 = \kappa_1 x + \omega_1 t, \quad \theta_1^0 \in [0, 2\pi), \quad (5.8c)$$

$$\begin{aligned} \left(\frac{\kappa_1}{\omega_1} \right) &= \frac{4\pi i}{B} C_{11} \left(1 \pm \frac{(-1)^{m+1}}{16\sqrt{E_1 E_2}} \right) \quad E_1 < E_2 < 0, \\ &= \frac{4\pi i}{1 - 2B} C_{11} \left(1 \pm \frac{(-1)^{m+1}}{16\sqrt{E_1 E_2}} \right) \quad E_1^* = E_2. \end{aligned} \quad (5.8d)$$

Remark. (On the numerical computations.) The theta functions, $\Theta(l + \frac{1}{2}; B)$ and $\Theta(l; B)$, with the symmetries described above for B , l and $l + \frac{1}{2}$, have the property [6]

$$[\Theta(l + \frac{1}{2}; B)]^* = \Theta(l; B).$$

Thus,

$$q = i \ln \left(\frac{\Theta(l + \frac{1}{2}; B)}{\Theta(l; B)} \right)^2 = 4 \arctan \left(\frac{\text{Im}[\Theta(l; B)]}{\text{Re}[\Theta(l; B)]} \right). \quad (5.9)$$

The real and imaginary parts of $\Theta(l; B)$ are separated a priori, again using the structure of l and B . We now proceed to explicit computations.

Example 1. x -independent, pendulum solutions.

Spatially constant solutions of sine-Gordon are strictly periodic, with the discrete parameter $m \equiv 0$ in (5.7), (5.8). From (5.8d), the x -independent condition $\kappa_1 = 0$ corresponds to the explicit constraint on $\Sigma_{N=1}^{(s)}$:

$$\kappa_1 = 0 \quad \text{iff} \quad E_1 E_2 = 1/16^2. \quad (5.10)$$

For the two cases (5.3), (5.4) of $\Sigma_{N=1}^{(s)}$, this condition (5.10) yields an explicit parametrization of the real one-dimensional space of $\Sigma_{N=1}^{(s)}$ with $\kappa = 0$. To make contact with the parametrization of the classical pendulum representation of section 2, we also include the sine-Gordon energy H as a function of E_1, E_2 [5].

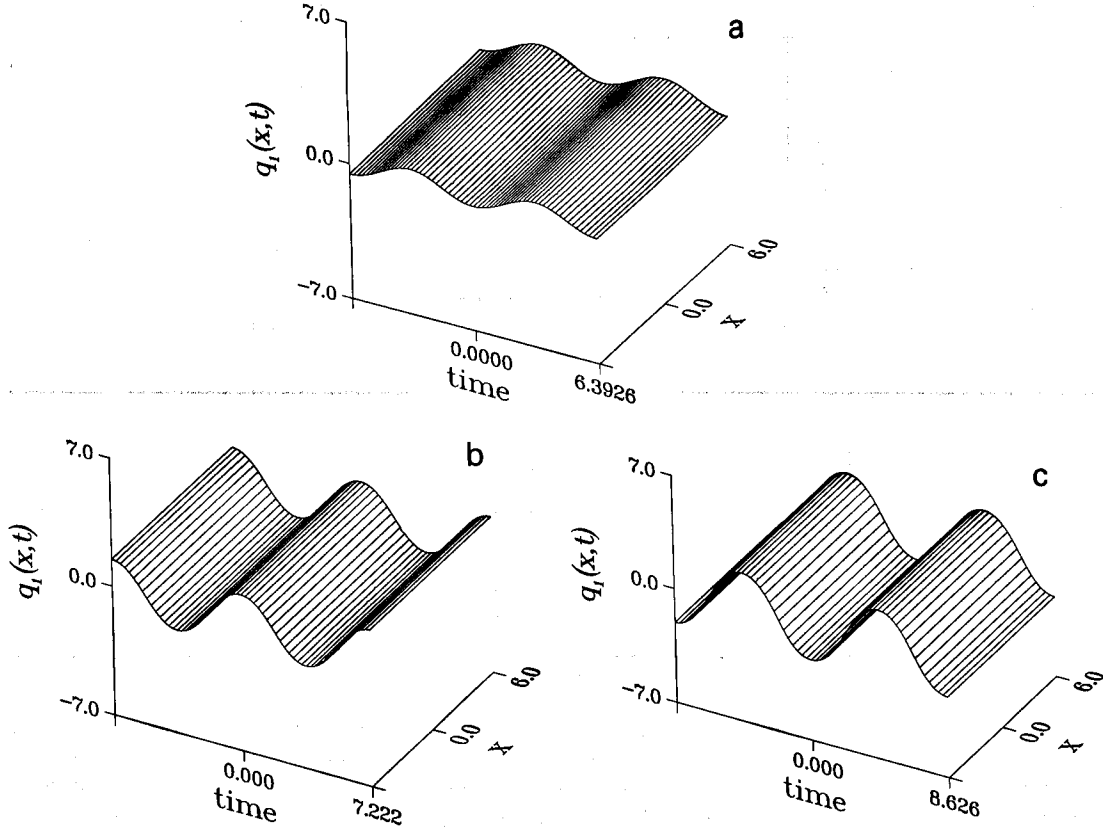


Fig. 4. The one-phase solutions $q_1(x, t)$ computed from (5.7), (5.8), (5.9) are shown for two t -periods and for $-6 \leq x \leq 6$. Since $\kappa_1 = 0$ for these solutions, they are x -independent; the x -period is chosen arbitrarily. In (a) $E_1 = E_1^* = \frac{1}{16} e^{i\pi/6}$, $\omega_1 = 0.98289$, $\text{Im}(B) = 0.28867$, in (b) $E_1 = E_1^* = \frac{1}{16} e^{i\pi(0.461)}$, $\omega_1 = 0.87$, $\text{Im}(B) = 0.47274$ and in (c) $E_1 = E_1^* = \frac{1}{16} e^{i2\pi/3}$, $\omega_1 = 0.7284$, $\text{Im}(B) = 0.63931$.

Case 1. $E_1^* = E_2$, $\kappa_1 = 0 \Leftrightarrow E_1 E_2 = 1/16^2$.

$$E_1 = \frac{1}{16} e^{i\phi}, \quad \phi \in (0, \pi), \quad H(E_1, E_2) = 1 - 8(E_1 + E_2) = 1 - \cos \phi \in (0, 2). \quad (5.11)$$

Case 2. $E_1 < E_2 < 0$, $\kappa_1 = 0 \Rightarrow E_1 E_2 = 1/16^2$.

$$E_1 = -\frac{1}{16} e^\eta, \quad \eta > 0, \quad H(E_1, E_2) = 1 + \cosh \eta > 2. \quad (5.12)$$

Figs. 4a–4c display $q_1(x, t)$ computed from (5.7), (5.8), (5.9) in case 1, (5.11), where $\phi = \text{phase}(E_1) = \text{amplitude of } q_1 = \pi/6, 0.461\pi, 2\pi/3$, respectively. Figs. 5a–5c show the corresponding Floquet spectrum of (1.3) for the solutions in figs. 4a–4c. Figs. 6a–6c depict $\text{Re}(\int_{E_1}^E \Omega_{N=1}^{(x)})$ and $\text{Im}(\int_{E_1}^E \Omega_{N=1}^{(t)})$ along the nonreal band of spectrum in the upper half plane, from which $\Delta(E)$ is computed, complex double points are identified, and the corresponding linearized growth rates are determined.

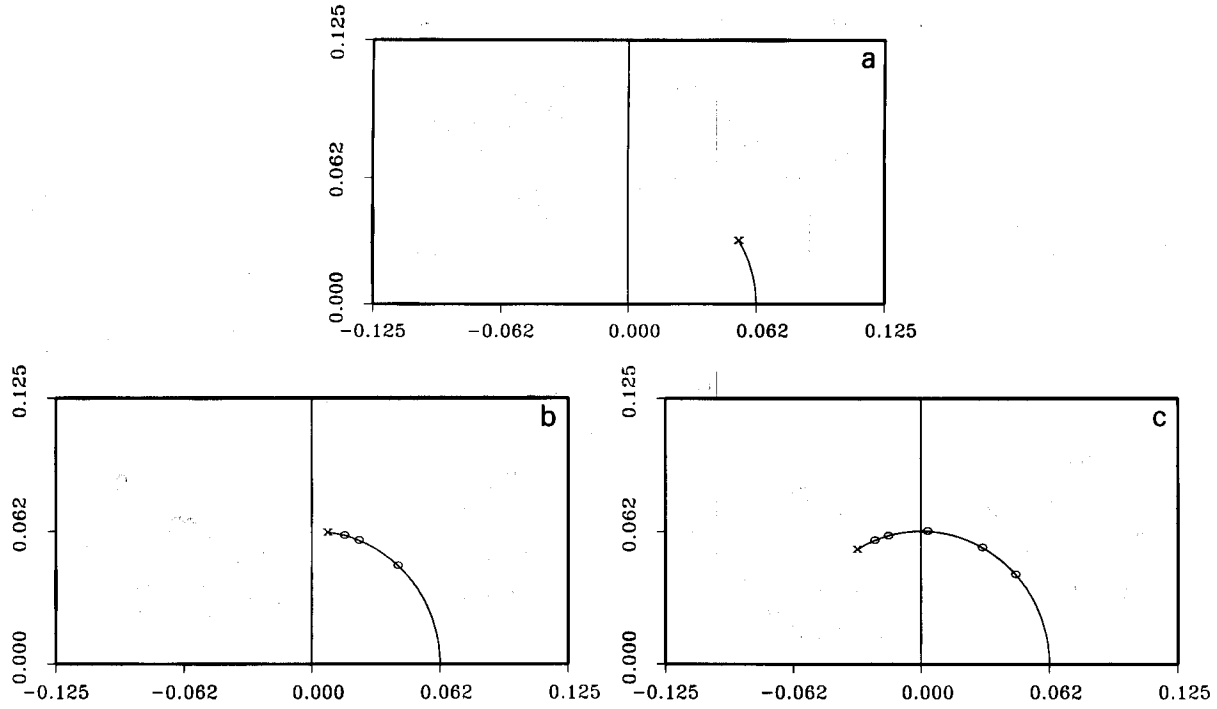


Fig. 5. The Floquet spectrum in the upper-half plane corresponding to the solutions in fig. 4 are shown. The spectrum is symmetric about the real axis. The spectrum includes the positive real axis, which is not shown in these figures. As noted in the text, the nonreal portion of the spectrum consists of an arc on the circle of radius $\frac{1}{16}$. The circles represent complex double periodic eigenvalues, (3.6), that arise for the indicated x -periods, taken as integer multiples of 6 (see fig. 6 on next page).

In the general $N = 1$ case, the differentials $\Omega^{(x)}, \Omega^{(t)}$ are

$$\Omega_{N=1}^{(x)}(E) = -\frac{1}{2} \left(E^2 - \beta_1^{(x)} E - \frac{(-1)^m \sqrt{E_1 E_2}}{16} \right) \frac{dE}{ER(E)}, \quad (5.13)$$

$$\Omega_{N=1}^{(t)}(E) = -\frac{1}{2} \left(E^2 - \beta_1^{(t)} E + \frac{(-1)^m \sqrt{E_1 E_2}}{16} \right) \frac{dE}{ER(E)}, \quad (5.14)$$

where $\beta_1^{(x)}, \beta_1^{(t)}$ are uniquely specified by

$$\oint_{\mu_1 \text{ cycle}} \Omega^{(x)} = \oint_{\mu_1 \text{ cycle}} \Omega^{(t)} = 0, \quad (5.15a)$$

$$\begin{aligned} \mu_1 \text{ cycle} &\sim a_1 - 2b_1 & E_1^* &= E_2, \\ &\sim b_1 & E_1 < E_2 < 0, \end{aligned} \quad (5.15b)$$

so that

$$\beta_1^{(x)} = \left(\oint_{\mu_1} \frac{E dE}{R(E)} \pm \frac{(-1)^m \sqrt{E_1 E_2}}{16} \oint_{\mu_1} \frac{dE}{ER(E)} \right) / \oint_{\mu_1} \frac{dE}{R(E)}. \quad (5.15c)$$

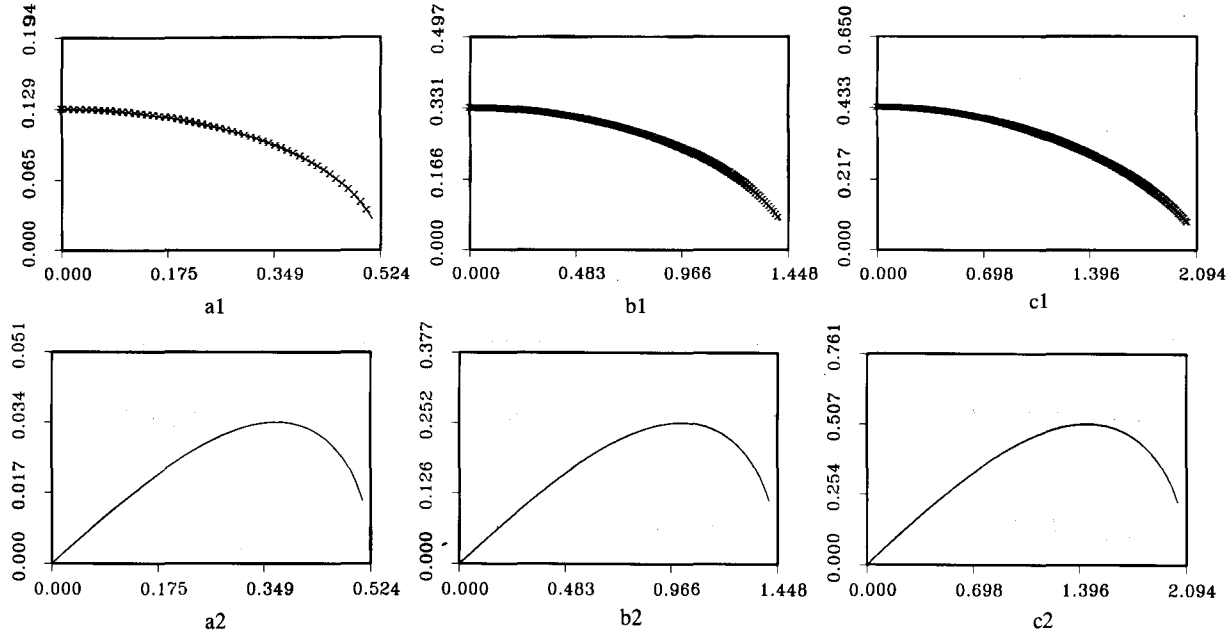


Fig. 6. We plot $\int_{E_1}^E \Omega^{(x)}$ in (a1), (b1), (c1) and $\int_{E_1}^E \Omega^{(t)}$ in (a2), (b2), (c2) where E is along the nonreal band of the spectrum; the horizontal axis is the polar angle of the points along the spectrum. (a), (b) and (c) correspond to figs. 4a, 5a, 4b, 5b and 4c, 5c respectively. (a1), (b1), (c1) allow the construction of $\Delta(E)$ along the complex spectrum, whereas (a2), (b2), (c2) constitute growth rates. In (a1), (b1), (c1), the solid curve represents the exact result from eq. (5.18a) and the hatched curve is from the computed values. These figures allow one to obtain complex double points, (3.6), and their growth rates for any choice of x -period. For example, for the complex double points, $E_{2p-1}^d = (E_{2p}^d)^* = \frac{1}{16} e^{i\phi_p^d}$, in figs. 5b, 5c, we find: in (b) $\phi_1^d = 0.266\pi$, $\sigma_1 = 0.238$ for $L = 12, 24$; $\phi_3^d = 0.380\pi$, $\sigma_2 = 0.233$ for $L = 18$; $\phi_5^d = 0.418\pi$, $\sigma_3 = 0.190$ for $L = 24$; and in (c) $\phi_1^d = 0.237\pi$, $\sigma_1 = 0.348$ for $L = 24$; $\phi_3^d = 0.342\pi$, $\sigma_2 = 0.456$ for $L = 18$; $\phi_5^d = 0.485\pi$, $\sigma_3 = 0.505$ for $L = 12, 24$; $\phi_7^d = 0.583\pi$, $\sigma_4 = 0.420$ for $L = 18$; $\phi_9^d = 0.618\pi$, $\sigma_5 = 0.342$ for $L = 24$. a1 a2 b1 b2 c1 c2

The graphs 6a–6c give complete linearized stability information as follows. Hochstadt's formula, (4.2), becomes

$$\Delta(E; q(t)) = 2 \cos \left(L \int_{E_1}^E \Omega_{N=1}^{(x)} \right), \quad (5.16)$$

where L is the x -period which is arbitrary for these x -independent solutions. For given L , one first finds if there exist any complex double periodic spectra E_p^d along non-real curves of spectrum by solving for $E_p^d \notin \mathbb{R}$ which satisfy

$$L \int_{E_1}^{E_p^d} \Omega_{N=1}^{(x)} = p\pi, \quad p \neq 0.$$

In each case, for L small enough there are no complex double points, and likewise no linear instabilities of $q_1(t)$ for those lengths L . As L increases beyond $\pi / \max_E (\int_{E_1}^E \Omega^{(x)})$ in fig. 6, nonreal double periodic spectra appear on the corresponding complex band of spectrum in fig. 5. These complex double points E_p^d label linearly unstable modes of $q_1(t)$, from fig. 4, whose growth rates σ_p are read off

directly from fig. 6 by the formula

$$\sigma_p = 2 \operatorname{Im} \left(\int_{E_1}^{E_p^d} \Omega^{(t)} \right). \quad (5.17)$$

As an illustration, we consider the pendulum solution $q_1(t)$ with $E_1 = \frac{1}{16} e^{i\pi(0.461)}$, energy $H = 0.8778$, and frequency $\omega = 0.87$, considered on an x -interval of length $L = 6, 12, 24$. Note from fig. 6b that $\max(\int_{E_1}^E \Omega^{(x)}) = 0.3313$. For $L = 6$, fig. 5b shows, since $6 \max(\int_{E_1}^E \Omega^{(x)}) < \pi$, there are no complex double spectra. For $L = 12$, there is one pair of complex double periodic points, since $\pi < 12 \max(\int_{E_1}^E \Omega^{(x)}) < 2\pi$. For $L = 24$, $2\pi < 24 \max(\int_{E_1}^E \Omega^{(x)}) < 3\pi$, there are two pairs of complex double points. In each case, we find E_p^d such that *along complex spectrum* $\int_{E_1}^{E_p^d} \Omega^{(x)} = p\pi/L$, and then compute the corresponding growth rate σ_p by (5.17). The results are

$$L = 12, \quad E_1^d = (0.0421, 0.0464), \quad \sigma_1 = 0.1193,$$

$$L = 24, \quad E_1^d = (0.0421, 0.0464), \quad \sigma_1 = 0.1193, \quad E_2^d = (0.016, 0.0606), \quad \sigma_2 = 0.0949.$$

Remark. The x -periods $L = 6, 12, 24$ are chosen to make contact with our extensive numerical investigations of the weakly perturbed sine-Gordon PDE [10, 11, 15, 16]. Also, refer ahead to case 3, section 7.1.

Remark. Analytic checks on the numerical discriminant code *via exact formulas* are provided by the following special examples.

In this special case of pendulum solutions [17], the form of $\Omega_{N=1}^{(x)}$, (5.13), simplifies dramatically, with

$$m = 0, \quad \beta_1^{(x)} = 0, \quad E_1 E_2 = 1/16^2,$$

and $\Omega_{N=1}^{(x)}$ becomes an *exact differential*,

$$\Omega_{N=1}^{(x)}(E) = -dW(E),$$

$$\begin{aligned} W(E) &= \sqrt{E + 1/16^2 E - \frac{1}{8} \cos \phi} \quad \text{if } E_1 = \frac{1}{16} e^{i\phi}, \\ &= \sqrt{E + 1/16^2 E + \frac{1}{8} \cosh \eta} \quad \text{if } E_1 = -\frac{1}{16} e^\eta. \end{aligned} \quad (5.18a)$$

Thus, the Floquet discriminant becomes

$$\Delta(E; q(t)) = 2 \cos[LW(E)], \quad (5.18b)$$

which yields an analytic representation of the entire Floquet spectrum, including a precise labelling of all double periodic spectra. The spectral codes based on (5.13), (5.15) are checked, in these special cases, against the exact analytic formula.

In the two cases (5.11), (5.12), the Hochstadt formula (5.18) yields:

Case 1. $E_1 = \frac{1}{16} e^{i\phi}$, $E_2 = \frac{1}{16} e^{-i\phi}$, $\phi \in (0, \pi)$, $0 < H < 2$.

$$\Sigma = \{E \mid -2 \leq \Delta \leq 2\} = \{E \mid W(E) \text{ is real}\}$$

$$= \{E \geq 0\} \cup \{E = \frac{1}{16} e^{i\theta}, -\phi \leq \theta \leq \phi\}.$$

$$\Sigma^p = \text{periodic spectrum} = \Sigma^{(s)} \cup \Sigma^{(d)}$$

$$\Sigma^{(s)} = \{E_j \mid \Delta = \pm 2, \Delta'(E_j) \neq 0\} = \{E_1, E_2\},$$

$$\Sigma^{(d)} = \{E_j^d \mid \Delta = \pm 2, \Delta'(E_j^d) = 0\} = \{E_j^d \mid W(E_j^d) = j\pi/L\}.$$

The *nonreal* double periodic spectra are precisely given by

$$E_j^d = \frac{1}{16} e^{\pm i\alpha_j},$$

$$\cos \alpha_j = \cos \phi + 8j^2\pi^2/L^2, \quad j = 1, \dots, M,$$

where M is the largest positive integer such that

$$\cos \phi + 8(M\pi/L)^2 < 1.$$

(Note: These double point formulas coincide with results from our general codes.)

Case 2. $E_1 = -\frac{1}{16} e^\eta$, $E_2 = -\frac{1}{16} e^{-\eta}$, $\eta > 0$, $H > 2$.

$$\Sigma = \{E \geq 0\} \cup \{|E| = \frac{1}{16}\} \cup \{E \mid E_1 \leq E \leq E_2\}.$$

The *nonreal* double periodic spectra are

$$E_j^d = \frac{1}{16} e^{\pm i\alpha_j},$$

$$\cos \alpha_j = -(\cosh \eta - 8j\pi/L), \quad j = 1, \dots, M,$$

where $j = 1, \dots, M$ satisfy

$$|\cosh \eta - 8j\pi/L| < 1.$$

These formulas are relevant for the next examples.

Proceeding now to some more examples, figs. 7a–7c display $q_1(x, t)$ in case 2, (5.12), corresponding to *kink or antikink pendulum solutions*, where $E_1 = -\frac{1}{16} e^\eta$, $\eta = 0.001, 0.1, 1.0$, respectively. Figs. 8a–8c display the corresponding Floquet spectrum of (1.3) for these “helical” pendulum modes. Figs. 9a–9c depict $\text{Re}(f_{E_1}^E \Omega_{N=1}^{(x)})$ and $\text{Im}(f_{E_1}^E \Omega_{N=1}^{(y)})$ along the nonreal band of spectrum, $|E| = \frac{1}{16}$, in the upper half plane.

Once again we deduce all linearized stability information from these graphs. We first fix a length L , then determine if there are any nonreal double periodic eigenvalues, E_p^d , by solving for $E_p^d \notin \mathbb{R}$ such that

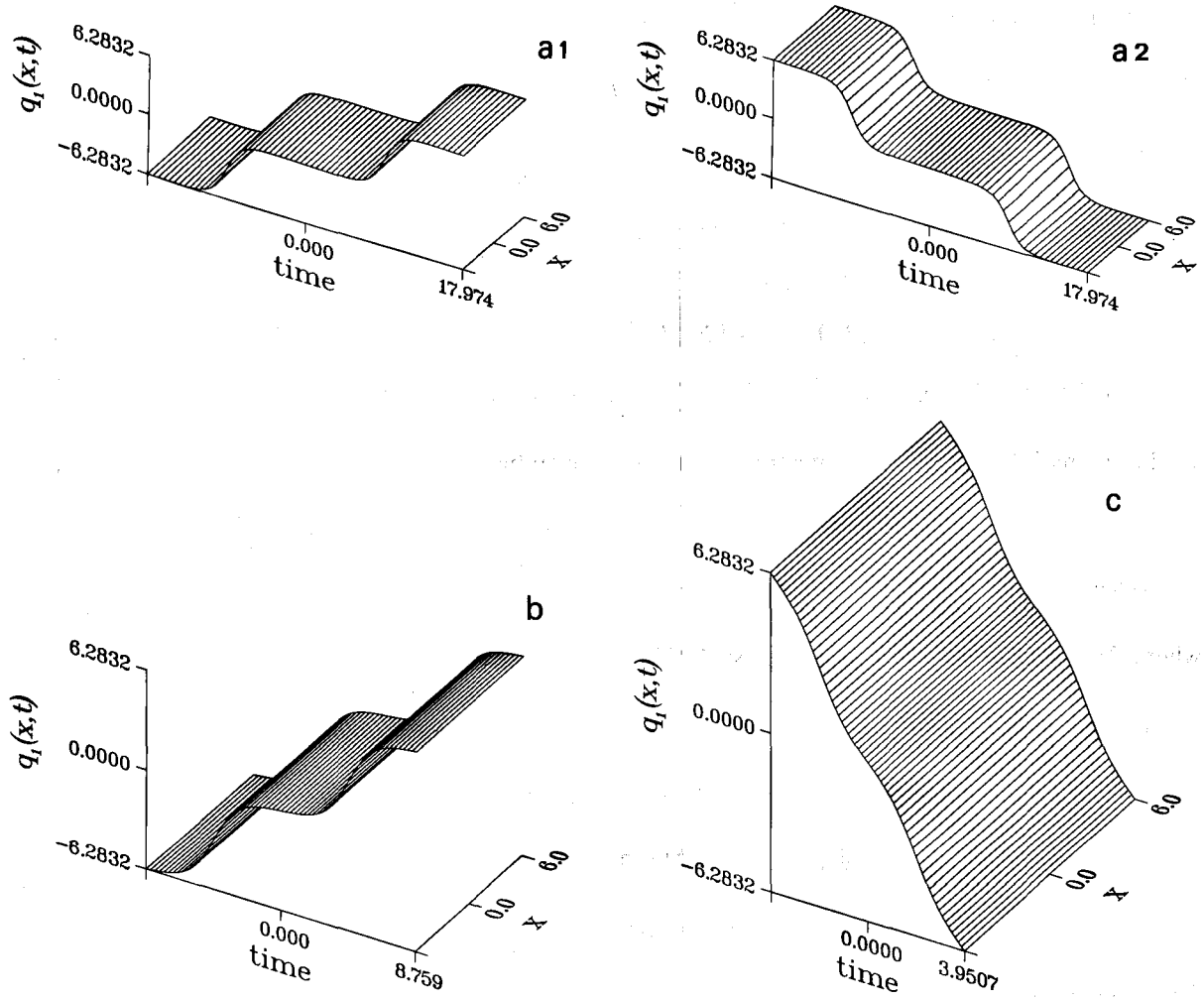


Fig. 7. Spatially uniform, running pendulum solutions are depicted. (a1), (a2) both correspond to negative real periodic spectra of case 2, (5.12), $\eta = 0.001$, energy $H = 1 + \cosh \eta = 2.0000005$, where (a1) is the kink mode of this energy specified by $\text{Re}(l_0) = \frac{1}{4}$, (5.8a), and (a2) is the anti-kink mode with $\text{Re}(l_0) = -\frac{1}{4}$, (5.8a). (b), (c) are higher energy running pendulum modes, with $H = 1 + \cosh \eta$, $\eta = 0.1$ in (b) and $\eta = 1.0$ in (c), and we have selected to display the kink mode in (b) and the antikink mode in (c) by the choices of $\text{Re}(l_0) = \frac{1}{4}, -\frac{1}{4}$, respectively.

$\int_{E_1^d}^{E_p^d} \Omega^{(x)} = p\pi/L$. For each such pair, $(E_p^d, (E_p^d)^*)$, we then compute the linearized growth rate σ_p in that mode by formula (5.17). Explicit examples may be created by the reader with the information provided here.

Example 2. t -independent solutions $\omega_1 \equiv 0$, $\kappa_1 \neq 0$.

Each of the above x -independent solutions yields a corresponding t -independent (inverted pendulum) solution by the Backlund transformation $(q, x, t) \rightarrow (q + \pi, t, x)$. These examples are instructive from the point of view of curves of spectrum and their connection to linearized instabilities. The above formulas for $\Omega^{(x)}$ and $\Omega^{(t)}$ are interchanged, so that now $\Omega^{(t)}$ is exact, not $\Omega^{(x)}$, and the Floquet discriminant must be computed numerically.

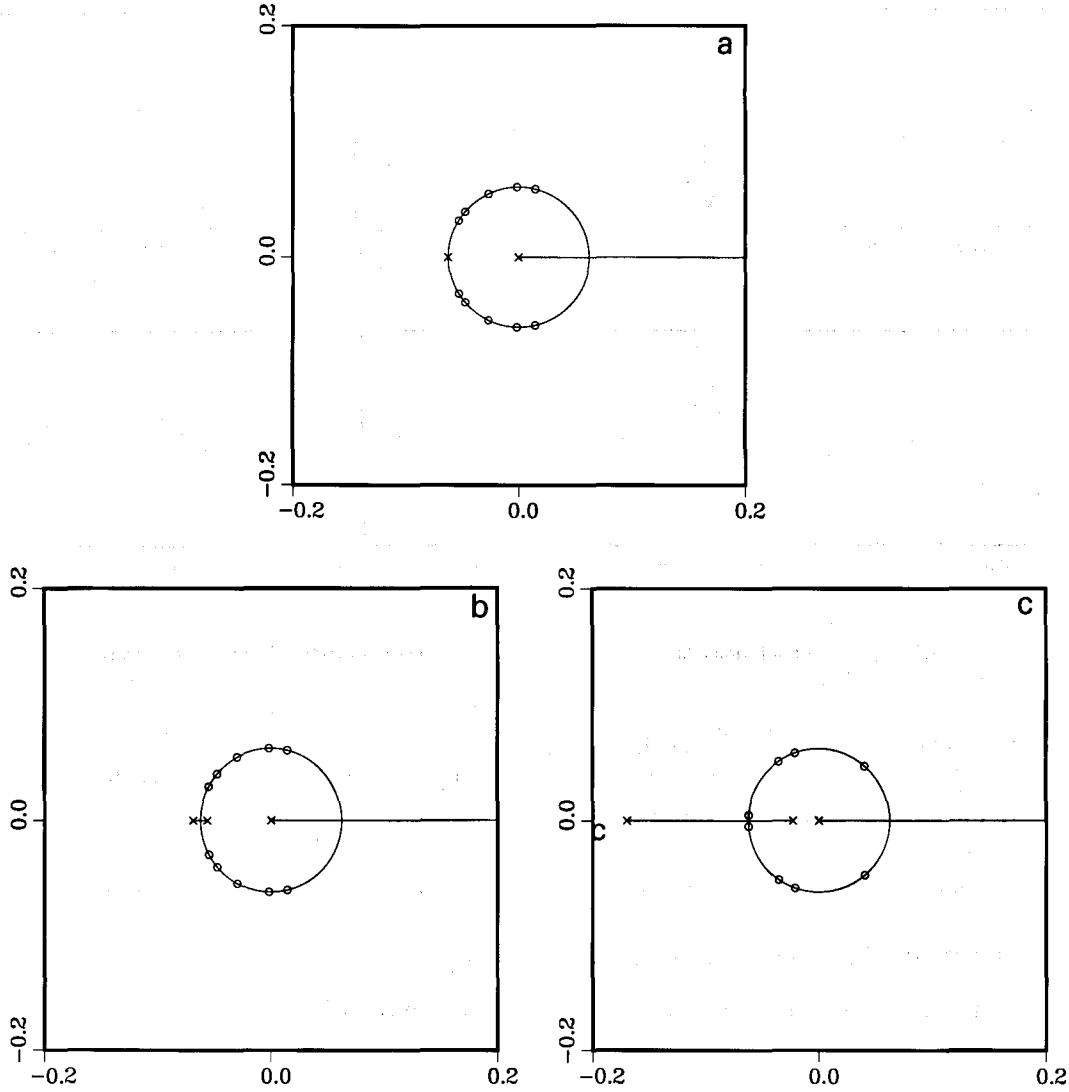


Fig. 8. The Floquet spectrum for the modes 7a, 7b, 7c is displayed in (a), (b), (c) respectively. The negative real band of spectrum is the interval from E_1 to E_2 . For charge $m = 0$ (x -independent solutions), the entire circle $|E| = \frac{1}{16}$ is continuous spectrum. From fig. 9, with chosen spatial length L , pairs of complex double points, (3.6), for selected lengths $L = 6, 12, 18, 24$ are labelled on the spectral bands.

For the same choices of $\Sigma_{N=1}^{(s)}$ as in example 1, but with $m = 1$ now so that $\omega = 0$, $\kappa \neq 0$, (5.8d), the spectrum is easily described relative to the $m = 0$ case of figs. 5a–5c, 8a–8c. For spatial oscillatory solutions ($E_1^* = E_2$) at rest, the real spectrum is the same, whereas the complement of the $m = 0$ spectrum on the circle of radius $\frac{1}{16}$ now becomes the spectrum with $m = 1$. For spatial kinks ($E_1 < E_2 < 0$) at rest (t -independent), the real spectrum is the same as in figs. 8a–8c, whereas the “ring” $|E| = \frac{1}{16}$ is absent. This implies that there is *no complex spectrum*, and therefore *no possibility of linearized instability for spatial kink trains at rest*.

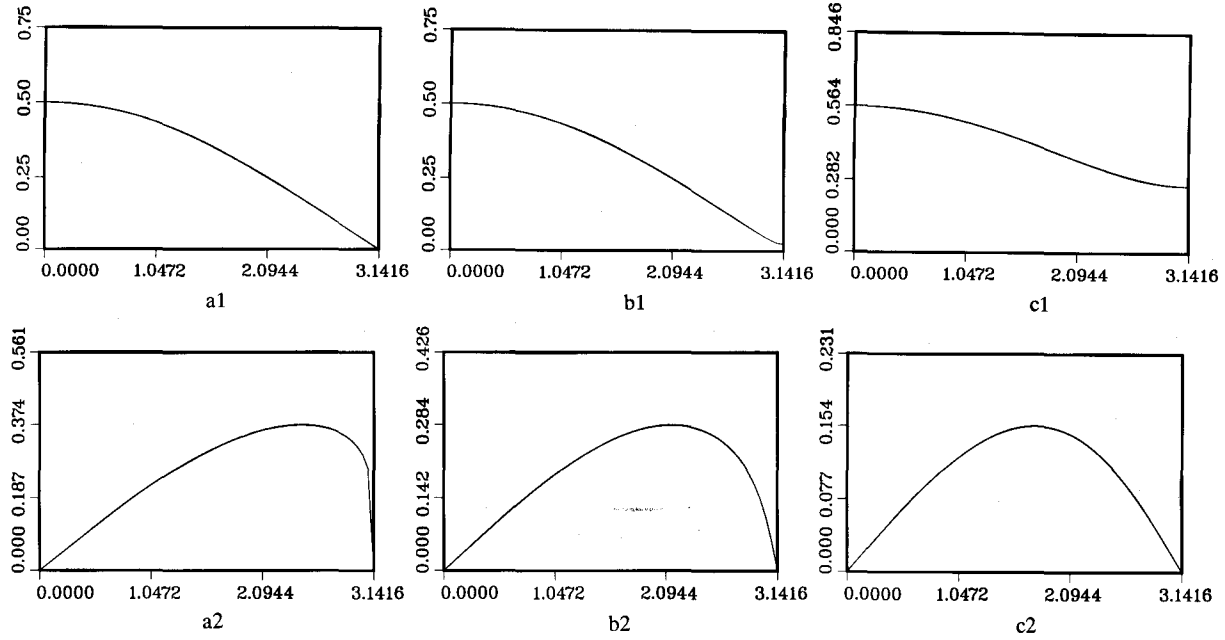


Fig. 9. The plots $\int_{E_1}^E \Omega^{(x)}$, $\int_{E_1}^E \Omega^{(t)}$ for solutions 7a, 7b, 7c are shown in (a1), (a2), (b1), (b2), (c1), (c2) respectively. The same remarks as in the fig. 6 caption apply here.

Example 3. Single-phase oscillatory traveling waves.

We now relax the constraint $E_1 E_2 = 1/16^2$, which yields x and t dependent traveling waves ($\kappa \neq 0$ and $\omega \neq 0$). Of interest now is the set of all $\Sigma_{N=1}^{(s)}$ with a fixed spatial period, or likewise, with a fixed temporal period, computed now from formulas (5.8d).

Fig. 10 provides several loci of E_1 in the upper half-plane (UHP) ($E_2 = E_1^*$) corresponding to ($m = 0$)

$$\{E_1 \in \text{UHP} \mid \kappa_1 = [4\pi i / (1 - 2B)] C_{11} (1 - 1/16 |E_1|) \equiv \text{constant}\}, \quad (5.19a)$$

$$\{E_1 \in \text{UHP} \mid \omega_1 = [4\pi i / (1 - 2B)] C_{11} (1 + 1/16 |E_1|) \equiv \text{constant}\}. \quad (5.19b)$$

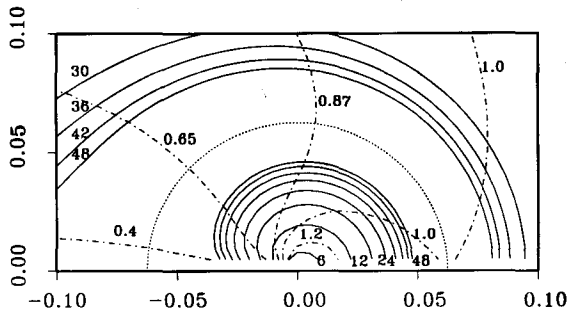


Fig. 10. Loci of $E_1 (= E_2^*)$ in the upper half-plane corresponding to fixed x -period, $L = 6, 12, \dots, 48$ (solid curves) and fixed t -period, $\omega_1 = 0.4, 0.65, 0.87, 1.0, 1.2$ (dash-dotted curves) are shown. Note that these curves are symmetric under inversion through the circle of radius $1/16$ (the dotted curve). At the intersection point of the solid/dashed curves, inside $|E| = 1/16$, the corresponding solution $q_1(x, t)$ is a right-running single-phase wave with indicated wavenumber $\kappa_1 = 2\pi/L$ and frequency ω_1 . At the inverted point about $|E| = 1/16$, $1/16^2 E_1$, one finds the same wavenumber and frequency, but a left-running wave. On the circle one finds $\kappa_1 = 0$. Note the roles of κ and ω can be reversed by the choice of the charge $m = 1$ instead of $m = 0$.

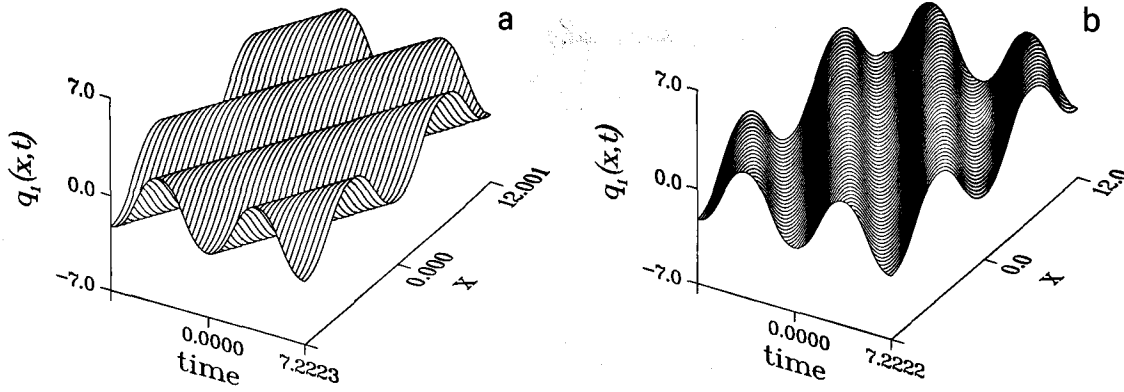


Fig. 11. The two single-phase wavetrains with $L = 12$, $\omega_1 = 0.87$ are shown. In (a) $E_1 = 0.0155362 e^{i\pi(0.7061)}$, $\text{Im}(B) = 0.681427$, which gives a right-running wave. In (b) $E_1 = 0.251439 e^{i\pi(0.7061)}$, $\text{Im}(B) = 0.681439$, which gives a left-running wave. The two simple spectra are related by inversion through $|E| = \frac{1}{16}$.

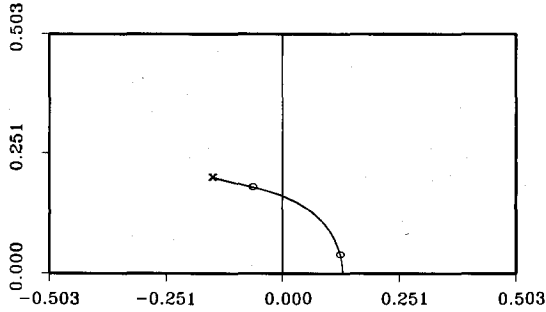


Fig. 12. The Floquet spectrum in the upper-half plane corresponding to the solution in fig. 11b is shown. The spectrum is symmetric about the real axis. The spectrum includes the positive real axis, which is not shown here. There are two pairs of complex double points, (3,6), for $L = 12$ given by $E_1^d = (0.1242, 0.0391)$, with linearized growth rate σ_1 computed from (5.17), $\sigma_1 = 0.0373$ and $E_2^d = (-0.0643, 0.18)$, with growth rate $\sigma_2 = 0.1102$. The spectrum corresponding to fig. 11a is obtained by an inversion through $|E| = \frac{1}{16}$.

(Again, these formulae for κ_1 and ω_1 may be reversed by taking $m = 1$, corresponding to the discrete transformation $(q, x, t) \rightarrow (q + \pi, t, x)$.)

The intersection of these $\kappa_1 \equiv \text{constant}$, $\omega_1 \equiv \text{constant}$ curves yields the unique $\Sigma_{N=1}^{(s)} = \{E_1, E_2 = E_1^*\}$ corresponding to the unique single-phase sine-Gordon solution (5.8), (5.9) with the prescribed wavenumber and frequency. There is another solution with the same value of $|\kappa_1|$, $|\omega_1|$ but opposite phase velocity obtained by inversion of $\Sigma_1^{(s)}$ through $|E| = \frac{1}{16}$, i.e., $\Sigma_1^{(s)} = \{1/16^2 E_1, 1/16^2 E_1^*\}$.

For example^{#1}, prescribed x -period $L = 12$ and frequency $\omega = 0.87$ yields precisely two distinct sets $\Sigma_{N=1}^{(s)}$, one with $E_1 = 0.251439 e^{i\pi(0.7061)}$, $E_2 = E_1^*$, and the other simple periodic spectrum is obtained by inversion of this set through the circle of radius $\frac{1}{16}$. One simple spectrum (outside of the circle of radius $\frac{1}{16}$) yields a right-running (fig. 11a), the other a left-running (fig. 11b), single-phase wavetrain.

The Floquet spectrum for these solutions no longer resides on the circle of radius $\frac{1}{16}$; in fact, one continuous spectrum is the inversion of the other through this circle. We compute these spectral curves numerically using Hochstadt's formula, (5.16), with $\Omega_{N=1}^{(x)}$ given by (5.13), $m = 0$. Fig. 12 shows the spectrum corresponding to fig. 11a. For period $L = 12$, we find there are two pairs of nonreal double periodic eigenvalues, each of which yields a positive growth rate, so that the solution is two-dimensionally unstable. The same solution also is periodic on an interval of length $L = 24, 36, \dots$, etc. For $L = 24$, we find four pairs of nonreal double points.

^{#1}This example is relevant for the studies of the damped, driven sine-Gordon system with x -periodic boundary conditions [10, 11].

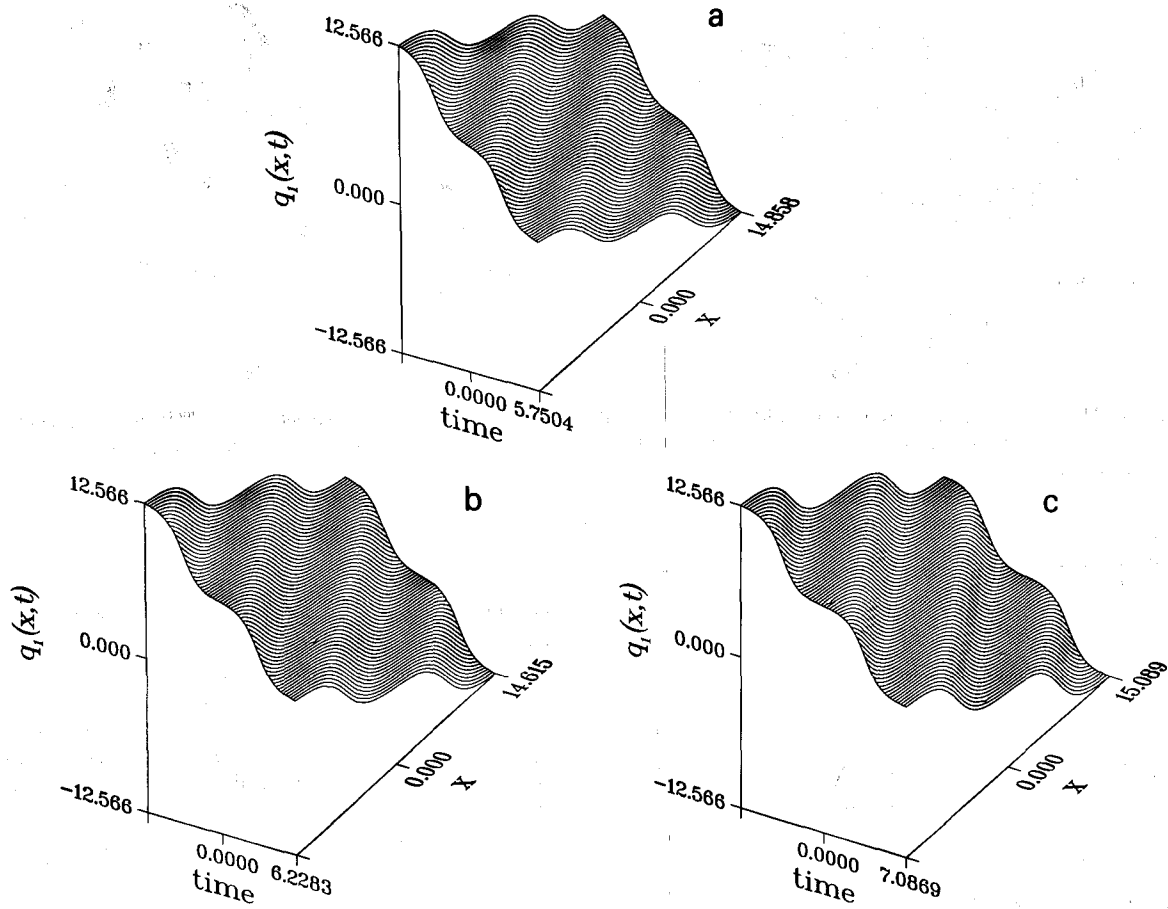


Fig. 13. Three traveling wave kink solutions for two x -periods and two t -periods are shown. In all three cases $E_1 = -0.2$, while we vary E_2 with $E_2 = -0.1, -0.120642, -0.15$ in (a), (b) and (c) respectively.

Example 4. Single-phase kink trains.

We now display some running wavetrains where $E_1 < E_2 < 0$ are not symmetric about $|E| = \frac{1}{16}$. In addition to displaying these traveling wave kink solutions, figs. 13a–13c, we have chosen these examples also to illustrate the “ring” of spectrum may deform and detach from the negative real band of spectrum between E_1 and E_2 (figs. 14a–14c).

6. Numerical two-phase inverse spectral solutions

Next we implement the IST algorithm of sections 3, 4 for two-phase sine-Gordon wavetrains. This class of solutions requires more sophisticated mathematical analysis than the classical traveling wave solutions, and thus represents the first significant payoff from the general IST construction of solutions. We emphasize, however, that even in the single-phase computations above, nontrivial results have been deduced from IST: the spectral theoretic results, labelling of unstable modes, and computation of linearized growth rates.

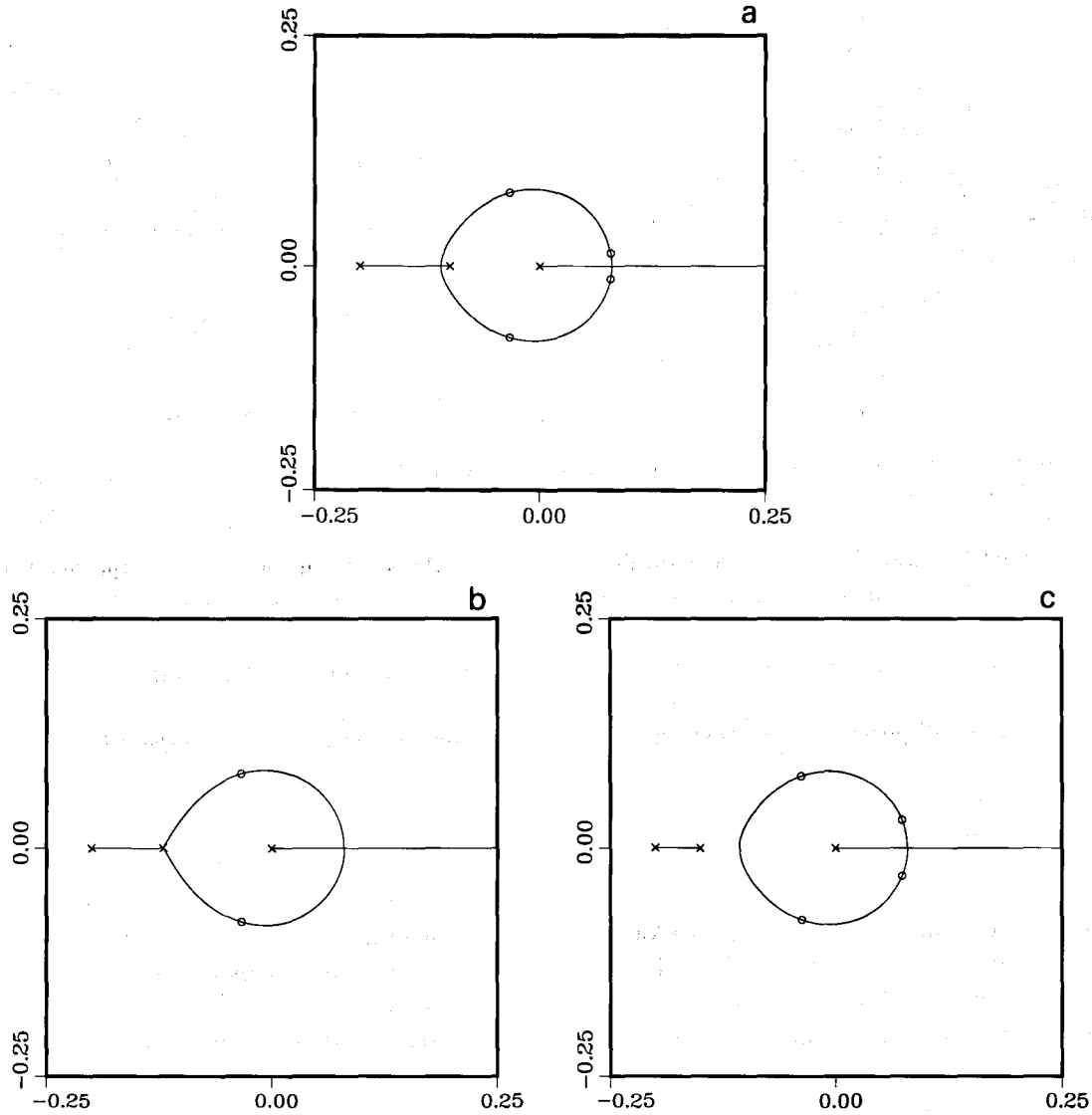


Fig. 14. The Floquet spectrum corresponding to the solutions in figs. 13a–13c are shown. The crosses denote the simple spectra and the circles denote the complex double points, (3.6).

The two-phase sine-Gordon solutions may consist of the nonlinear superposition of two purely oscillatory phases, two kink phases (periodic mod 2π) or two antikink phases, a kink–antikink pair, or an oscillatory–running mode superposition. At the level of solutions, these are rather easily categorized. However, there is a variety of spectral configurations, which translate into physical aspects of the waves such as stability properties, which have not yet been analytically charted. We will display some of this variety and corresponding physical implications as we implement the two-phase IST algorithm.

Step 1. Choose a two-phase simple-periodic spectrum of (1.3),

$$\Sigma_{N=2}^{(s)} = \{E_j, j = 1, \dots, 4 \mid E_{2j-1} < E_{2j} < 0 \text{ or } E_{2j}^* = E_{2j-1}, \text{ all distinct}\}. \quad (6.1)$$

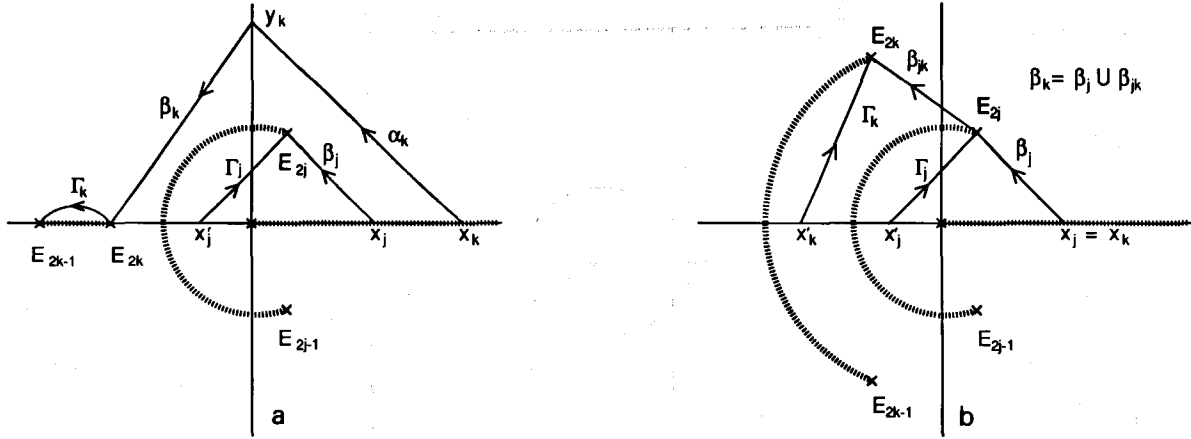


Fig. 15. (a) Parametrized paths for numerical computation of a, b cycles. (b) Computationally efficient parametrization of a, b cycles when there are at least two pairs of conjugate branch points.

(We assume for now that (6.1) is a bona fide simple periodic spectrum of (1.3), i.e., the fixed period constraints (3.9d) are satisfied. These constraints will be verified in step 3. Nonetheless, *if one relaxes the constraints (3.9d), this algorithm yields sine-Gordon solutions which are quasiperiodic in x and t . The spectral theoretic and stability considerations, however, must be completely revamped.*)

Step 2. Compute all period information on the genus 2 Riemann surface \mathcal{R} , determined from $\Sigma_{N=2}^{(s)}$ by

$$\mathcal{R} = \left\{ (E, R(E)) \mid R^2(E) = E \prod_{j=1}^4 (E - E_j) \right\}. \quad (6.2)$$

The branch cuts and choice of a, b cycles on \mathcal{R} are chosen as in fig. 1, and we recall the holomorphic period information as described in step 2, section 3. *For computational purposes*, we first depict the parametrization of each closed curve a_j, b_j , $j = 1, 2$, on \mathcal{R} , specific to whether the pair (E_{2j-1}, E_{2j}) is negative real or complex conjugates. (Recall fig. 1 of section 3 and fig. 3 of section 5.) With the parametrizations of fig. 15, the single-phase formulae, (5.3), (5.4), apply to each individual pair of simple spectra, (5.3) for negative pairs, (5.4) for conjugate pairs. (These results are, in fact, independent of N and apply to general $\Sigma_N^{(s)}$.)

Parametrized a, b periods of basic differentials

Let $\phi_p = E^p dE/R(E)$, $p = 0, \pm 1, 2$. Then, in the notation and convention of figs. 1, 15,

Case 1. $E_{2k-1} < E_{2k} < 0$

$$\oint_{a_k} \phi_p = 2 \operatorname{Re} \left(\int_{\Gamma_k} \phi_p \right). \quad (6.3a)$$

$$\oint_{b_k} \phi_p = 2i \operatorname{Im} \left(\int_{\alpha_k \cup \beta_k} \phi_p \right). \quad (6.3b)$$

Case 2. $E_{2j}^* = E_{2j-1}$

$$\oint_{a_j} \phi_p = 4 \operatorname{Re} \left(\int_{\Gamma_j} \phi_p \right) \quad (6.4a)$$

$$\oint_{b_j} \phi_p = 2 \operatorname{Re} \left(\int_{\Gamma_j} \phi_p \right) + 2i \operatorname{Im} \left(\int_{\beta_j} \phi_p \right). \quad (6.4b)$$

Remark. As noted in section 5, these path integrals are independent of the choices of $x_j > 0$, $x_k > 0$, $x'_j < 0$, which we exploit to check the numerical computations.

Remark. For computational efficiency and economy, *specific* choices of the paths $\alpha_k, \beta_k, \beta_j, \Gamma_j$ of fig. 15a may be chosen. For the $N = 2$ example of fig. 15a, one may take $y_k = E_{2j}$, $x_j = x_k$, so that two of the five paths are the same, $\alpha_k \equiv \beta_j$. In the $N = 2$ example of two conjugate pairs for $\Sigma_{N=2}^{(s)}$, the economical choice is indicated in fig. 15b. *In general, $2N$ linear segments suffice to compute the $2N$ cycles a, b .*

The holomorphic period data, normalization constants C_{ij} and 2×2 period matrix B , are then constructed from the periods (6.3), (6.4), $p = 0, 1$, by purely algebraic operations via formulas (3.13), (3.14).

Step 3. Construct the Riemann theta function of two variables, $\Theta(z; B)$, with period matrix B computed above. Given B , we can compute $\Theta(z, B)$ for any z :

$$\Theta(z; B) = \sum_{k \in \mathbb{Z}^2} \exp[i\pi(Bk, k) + 2i\pi(z, k)]. \quad (6.5a)$$

In particular, we shall compute $\Theta(z, B)$ along the real sine-Gordon flows, $z = l(x, t) + \frac{1}{2}$ and $z = l$, (3.19), (3.21).

The period matrix B and the 2-phase vector $l(x, t)$ have the special symmetries indicated in equations (3.19), (3.20), which we first numerically verify and then explicitly use in the numerical computations.

Step 4. Compute the 2-phase sine-Gordon solution, (3.19), with the prescribed simple spectrum $\Sigma_{N=2}^{(s)}$, (6.1),

$$q_2(x, t) = i \ln \left(\frac{\Theta^2(l + \frac{1}{2}; B)}{\Theta^2(l; B)} \right) = 4 \arctan \left(\frac{\operatorname{Im}[\Theta(l; B)]}{\operatorname{Re}[\Theta(l; B)]} \right). \quad (6.5b)$$

Remark. (On the numerical computation of multiple theta series)

We now describe the procedure used for numerical evaluation of the theta function for breather trains (similar considerations apply in the other cases as well). In this case $\operatorname{Re}(B) = \frac{1}{2}I$ and l is purely imaginary. Using this, we split the series (6.5a) into three pieces, corresponding to $(k = (k_1, k_2)^t)$ k_1 and k_2 both even, both odd, and one even, one odd. The terms in these subseries are all positive and real (exponential of a real quantity), where the first two contribute to the real part and the third one gives the imaginary part of $\Theta(l; B)$.

Next, observe that each term in the series is of the form $\exp\{-\pi[(bk, k) + 2(v, k)]\}$, where $b = \text{Im}(B)$ and $l = iv$. We estimate the k_0 which gives the largest contribution to the series from the maximum absolute value of the quadratic form which multiplies π . The estimate of the number of terms that must be included for a given relative accuracy is easily obtained in terms of $\|b\|$. In single precision machine arithmetic this often leads to overflow. To avoid this, we subtract from the argument of the exponential an estimate of the maximum of the quadratic form. The effect of this is an overall factor which cancels in the ratio in (6.5b). In practice, it is sufficient to include ≈ 10 terms in each component k_j to obtain approximately 6-digit accuracy for moderate values of x and t . Recall that the values of the theta function in one fundamental period suffice to give its values for all arguments. These periodicity properties are not implemented in the numerical computations, but rather checked numerically, primarily to test how well the numerical algorithm works.

Before proceeding to explicit examples, we recall the spectral theoretic discussions of section 4. To apply spectral theory, we must choose $\Sigma_{N=2}^{(s)}$, (6.1), so that the fixed x -period constraints are satisfied. With κ_1, κ_2 as computed from (3.21e), we must have (from (3.9d))

$$\kappa_1 = n_1 2\pi/L, \quad \kappa_2 = n_2 2\pi/L, \quad n_1, n_2 \in \mathbb{Z}, \quad (6.6)$$

for some fundamental x -period L .

Numerically, of course, all machine computations yield commensurate κ_1, κ_2 , but the period L may be quite large. Following most conceivable applications, we opt to prescribe $L = \mathcal{O}(1)$ and search for those $\Sigma_{N=2}^{(s)}$ that satisfy (6.6) for small n_1, n_2 . We shall begin with a special subclass of $\Sigma_{N=2}^{(s)}$ for which (6.6) is automatically satisfied. Namely, we impose the symmetry

$$E_j \in \Sigma_{N=2}^{(s)} \quad \text{iff} \quad 1/16^2 E_j \in \Sigma_{N=2}^{(s)}, \quad (6.7a)$$

which can be shown [21] to impose the following constraints on κ, ω :

$$\{\kappa_1 = \pm \kappa_2 \text{ or } \kappa_2 = 0, \kappa_1 \neq 0\} \quad \text{and} \quad \{\omega_1 = \pm \omega_2 \text{ or } \omega_2 = 0, \omega_1 \neq 0\}. \quad (6.7b)$$

For example, we find $\theta_1 = \kappa_1 x - \omega_1 t$, $\theta_2 = \kappa_1 x + \omega_1 t$, and in general the two-phase solutions (6.5) where $\Sigma_{N=2}^{(s)}$ satisfies the symmetry (6.7a) are *standing waves* if the phase shifts satisfy $\theta_1^0 = -\theta_2^0$, (3.23b). (Recall from section 5 that the symmetry (6.7a) for $N = 1$ implies either $\kappa_1 = 0$ or $\omega_1 = 0$.)

We also remark that the symmetry (6.7a) of the simple periodic spectrum implies a corresponding symmetry on the entire continuous spectrum of (1.3): $E \in \text{continuous spectrum} \Rightarrow 1/16^2 E \in \text{continuous spectrum}$. This result follows from period symmetries which ultimately imply [5, 21]

$$\Delta(E) = (-1)^m \Delta(1/16^2 E). \quad (6.7c)$$

6.1. Two-phase periodic standing waves. $E_j \in \Sigma_{N=2}^{(s)} \Leftrightarrow 1/16^2 E_j \in \Sigma_{N=2}^{(s)}$

This subsection is devoted to two-phase standing waves, characterized spectrally by the symmetry (6.7a). This subclass of $\Sigma_{N=2}^{(s)}$ is real, two-dimensional, and is explicitly parametrized below. The symmetry (6.7a) of the branch points of \mathcal{R} , (6.2), induces symmetries on periods of differentials on \mathcal{R} , which imply the wavenumber and frequency conditions (6.7b). The relations (6.7b) define *fundamental* x

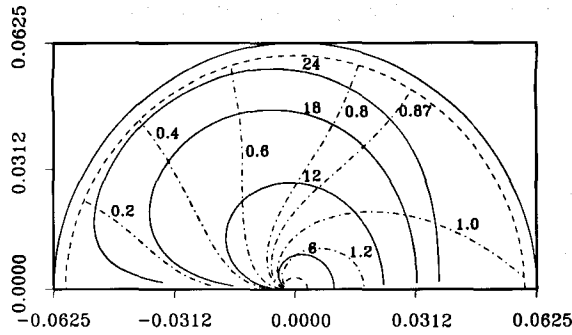


Fig. 16. Consider $\Sigma_{N=2}^{(s)} = \{E_1, E_2, E_3, E_4 | E_1 = E_2^* = \rho_1 e^{i\phi}, E_3 = E_4^* = \rho_2 e^{i\phi}, \rho_1 \rho_2 = 1/16^2, \rho_1 < \frac{1}{16}\}$. Loci of E_1 in the upper half plane corresponding to fixed x -period, $L = 6, 12, 18, 24$ (solid curves) and fixed t -period, $\omega_1 = -\omega_2 = 0.2, 0.4, 0.6, 0.8, 0.87, 1.0, 1.2$ (dash-dotted curves) are shown. The semi-circle of radius $\frac{1}{16}$ is included. The two dashed semi-circles represent the boundary of the region for which data were obtained.

and t periods for two-phase standing waves:

$$L = L^{(x)} = 2\pi / |\kappa_1|, \quad T = L^{(t)} = 2\pi / |\omega_1|. \quad (6.7d)$$

6.1.1. Standing breather trains

Here all $E_j \in \Sigma_{N=2}^{(s)}$, (6.1), are nonreal. If we introduce polar coordinates, then this two-dimensional family of standing 2-phase breather trains is explicitly parametrized by

$$\{\Sigma_{N=2}^{(s)} | \kappa_1 = \kappa_2\} = \{r e^{i\phi}, r e^{-i\phi}, (r/16^2) e^{i\phi}, (r/16^2) e^{-i\phi}; 0 < r < \frac{1}{16}, \phi \in (0, \pi)\}, \quad (6.8a)$$

or

$$\{\Sigma_{N=2}^{(s)} | \kappa_1 \neq 0, \kappa_2 = 0\} = \{\frac{1}{16} e^{i\phi_1}, \frac{1}{16} e^{i\phi_2}, \frac{1}{16} e^{-i\phi_1}, \frac{1}{16} e^{-i\phi_2}; 0 < \phi_1 < \phi_2 < \pi\}. \quad (6.8b)$$

The *fixed period subspaces* $L = L^{(x)} \equiv \text{constant}$ or $L^{(t)} \equiv \text{constant}$, of these families are then real, *one-dimensional subsets* of (6.8a), (6.8b). The curves of $\kappa_1 \equiv \text{constant}$ and $\omega_1 \equiv \text{constant}$ are numerically computed (fig. 16) for the subfamily (6.8a). In applications to weakly damped and driven sine-Gordon systems, for example, the x length L fixes κ_1 , the driving frequency determines ω_1 , and the intersection of κ_1, ω_1 level curves provides a candidate for two-phase, frequency- and phase-locked breather trains of the perturbed system.

We now exhibit theta function solutions and corresponding spectral data for elements of these two families.

Example A.1. Standing breather trains with $|E_j| = \frac{1}{16}$, $j = 1, \dots, 4$

We shall display two elements of this family (6.8b), along with their spectral and stability properties. First we note some features common to all solutions in the family (6.8b) with $m = 0$:

- (i) $\kappa_1 \neq 0, \kappa_2 = 0, \omega_1 = -\omega_2 \neq 0$.

The zero wavenumber, $\kappa_2 = 0$, indicates a *nonzero spatial mean* of these solutions, as the graphics below confirm.

(ii)

$$\text{Im}(B) = \begin{pmatrix} \alpha & \alpha \\ \alpha & \beta \end{pmatrix}.$$

(iii) maximum amplitude of $q_2(x, t) = \phi_1 + \phi_2$.

This is a remarkable nonlinear superposition of the single-phase result, $\max(q_1) = \phi_1 = \text{phase of } E_1$.

(iv) With charge variable $m = 0$ in (3.19c) and (4.3), the continuous spectrum of (1.3) for $q_2(x, t)$ in this family is always $E > 0$ together with the two arcs of the circle $E = \frac{1}{16} e^{i\phi}$, $\phi \in (\phi_1, \phi_2)$ and $\phi \in (-\phi_2, -\phi_1)$. Clearly, this entire continuous spectrum is invariant with respect to reflection through the circle $|E| = \frac{1}{16}$, $E \rightarrow 1/16^2 E$.

(v) For each of these solutions, $L \int_{E_1}^{E_2} \Omega^{(x)} = \pi$, so that $\Delta(E)$ has no double points on these two arcs of spectrum, and *therefore all of these standing breather trains are neutrally stable on their fundamental x-period*.

(vi) $E = \frac{1}{16}$ is a double periodic eigenvalue.

We numerically compute that $\Delta(\frac{1}{16}) = \pm 2$, and that the polynomial part of $\Omega^{(x)}$ has a simple zero at $E = \frac{1}{16}$, which implies $\Delta'(\frac{1}{16}) = 0$ by Hochstadt's formula.

The first example is given in fig. 17 where we have selected the two free parameters, ϕ_1, ϕ_2 , so that $L^{(x)} = 12$ and $\omega_1 = 0.87$. The graphics include: (a) the spatial structure of $q_2(x, t_n)$ at selected times t_n , (b) contour levels of the surface $q_2(x, t)$, (c) the surface $q_2(x, t)$ over one x -period and two temporal periods, (d) the spectrum of (1.3) in the upper half plane for this potential $q_2(x, t)$ with $L =$ the fundamental length, (e) $\Delta(E)$ along the nonreal band of spectrum, (f) $(L/\pi) \int_{E_1}^E \Omega^{(x)}$ along the band of spectrum, (g) $\text{Im}(\int_{E_1}^E \Omega^{(t)})$ along the spectrum.

Remarks. Note from fig. 17b that the maximum and minimum values of $q_2(x, t)$ are $\phi_1 + \phi_2$ and $-(\phi_1 + \phi_2)$ respectively.

From the values of $L \int_{E_1}^E \Omega^{(x)}$, one deduces that $\Delta(E) = 2 \cos(L \int_{E_1}^E \Omega^{(x)})$ is monotone on the two spectral bands, so that there are *no complex double periodic eigenvalues* when the system has the fundamental length $L^{(x)}$.

For lengths $L^{(n)} = nL^{(x)}$, $n > 1$, $n - 1$ double points are created on these complex spectral bands. For example, with $L = 24 = 2L^{(x)}$, the location E_p^d where $(L/\pi) \int_{E_1}^{E_p^d} \Omega^{(x)} = \frac{1}{2}$ in fig. 17f becomes a double point. Then, the growth rate associated to this potentially unstable mode is read off from fig. 15f and formula (6.5). For this example with $L = 24$, a double point occurs approximately at $E_1^d = \frac{1}{16} e^{i\pi(0.35)}$, with growth rate $\sigma_1 = 0.058$.

As another example of this family, we choose ϕ_1, ϕ_2 so that $\phi_1 + \phi_2 = \pi$, a much larger amplitude wave than the previous one. Here we display the surface (fig. 18a), the spectrum (fig. 18b), $\Delta(E)$ along the spectrum (fig. 18c).

Example A.2. Standing breather trains, family (6.8a)

The following features are common to all members of this family, again with $m = 0$. We also have chosen length $L = 12$ for most of the examples below.

(i) $\kappa_1 = \kappa_2 \neq 0$, $\omega_1 = -\omega_2 \neq 0$. (Recall the $\kappa_1 \equiv \text{constant}$, $\omega_1 \equiv \text{constant}$ level curves for this family, fig. 16.)

In contrast to family (6.8b), now there is no zero wavenumber, *so the spatial mean of this family is zero*, as confirmed in the graphics below (figs. 19–25).

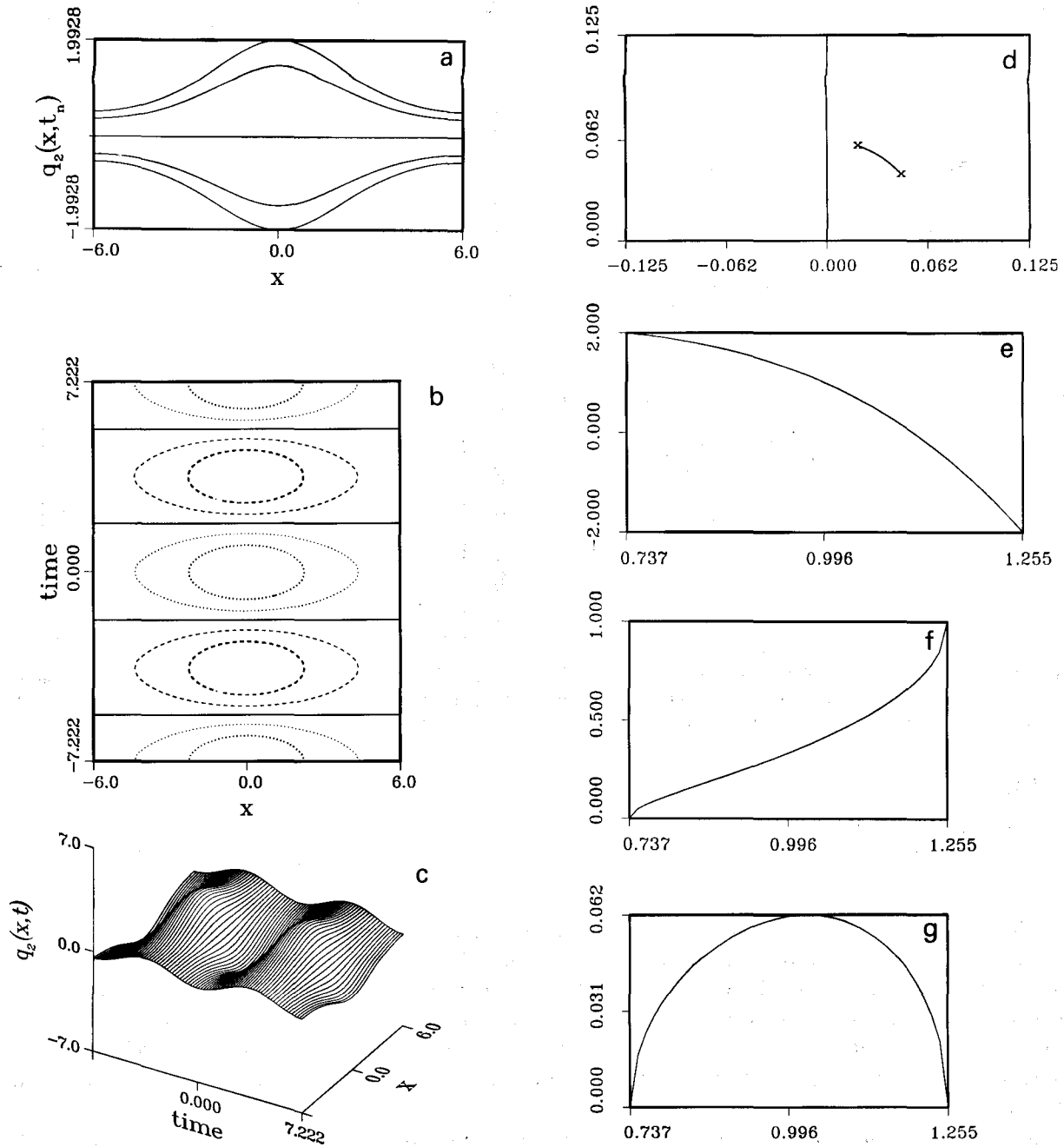


Fig. 17. For the two-phase solution with $E_1 = E_2^* = \frac{1}{16} e^{i\pi(0.23475)}$, $E_2 = E_4^* = \frac{1}{16} e^{i\pi(0.39957)}$, $L = 2\pi/|\kappa_1| = 12$, $\kappa_2 = 0$, $\omega_1 = -\omega_2 = 0.87$ we show (a) the spatial structure of $q(x, t_n)$ at selected times $t_n = n(T/8)$, $n = -4, -3, \dots, 4$, T is the temporal period, (b) contour levels of the surface $q(x, t)$, (c) the surface $q(x, t)$ over one x -period and two temporal periods, (d) the Floquet spectrum in the upper half plane, (e) $\Delta(E)$ along the complex band of spectrum, (f) $(L/\pi) f_{E_1}^E \Omega^{(x)}$ along the band of spectrum, (g) $\text{Im}(f_{E_1}^E \Omega^{(t)})$ along the spectrum. In (d) the part of the spectrum along the positive real axis is not shown. In (e), (f) and (g) the horizontal axis represents the polar angle of the points of the band of spectrum. In the contour plot, (b), we show five uniformly spaced contour levels, the dotted curves, the solid curves and the dashed curves correspond to $q_2 < 0$, $q_2 = 0$, $q_2 > 0$, respectively.

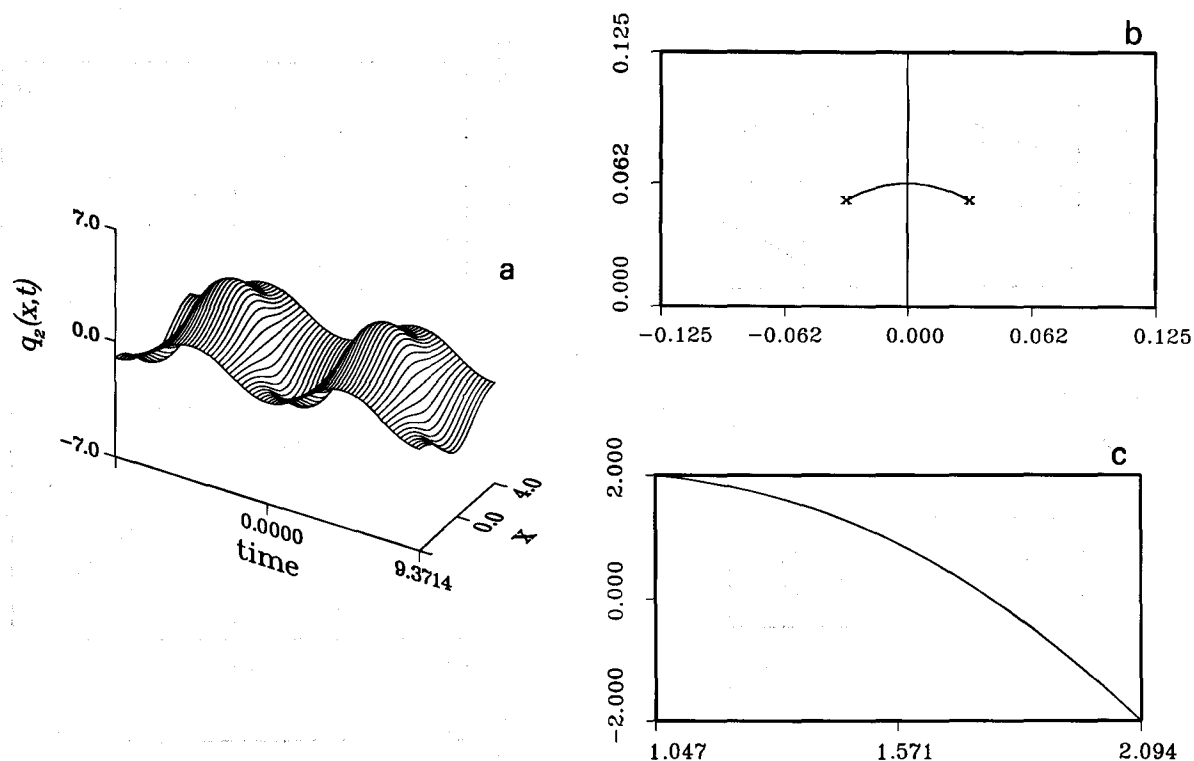


Fig. 18. For the two-phase solution with $E_1 = E_2^* = \frac{1}{16} e^{i\pi/3}$, $E_2 = E_4^* = \frac{1}{16} e^{i2\pi/3}$, $L = 2\pi/|\kappa_1| = 8.008$, $\kappa_2 = 0$, $\omega_1 = -\omega_2 = 0.6705$ we show (a) the surface $q_2(x, t)$ over one x -period and two temporal periods, (b) the Floquet spectrum in the upper half plane, (c) $\Delta(E)$ along the complex band of spectrum.

(ii)

$$\text{Im}(\mathbf{B}) = \begin{pmatrix} \alpha & \beta \\ \beta & \alpha \end{pmatrix}$$

(iii) Maximum amplitude of $q_2(x, t) = 2\phi$. If we fix ϕ , then the amplitude is independent of r .

(iv) The spectrum of (1.3) is symmetric about the circle $|E| = \frac{1}{16}$, but since the simple periodic spectra are off the circle, the spectral bands have more variety than in family (6.8b). The spectrum may all be connected to the positive E axis or may consist of two disjoint bands as in the previous family. We provide examples of each type of wave. Generally, the spectrum is connected for sufficiently small amplitude, and then detaches into two bands as ϕ is increased beyond a critical value that depends on the value of $r = |E_1|$.

(v) $E = \frac{1}{16}$ is a third-order periodic eigenvalue ($\Delta = \pm 2$, $\Delta' = \Delta'' = 0$, $\Delta''' \neq 0$) when the spectrum is all connected, and splits into two double periodic eigenvalues on the circle $|E| = \frac{1}{16}$ as the spectrum detaches away from the positive real axis. This is numerically verified by computing the zeros of the polynomial part of $\Omega^{(x)}$, which yield critical points of Δ . For example, when the spectrum is connected we always find $E = \frac{1}{16}$ is a first order zero of the polynomial part of $\Omega^{(x)}$.

(vi) When the spectrum has two disjoint bands, there are two complex double points, E_p^d and $(E_p^d)^*$, each of modulus $\frac{1}{16}$, which label potential instabilities. We show, however, that the growth rates σ_p actually vanish at these spectral points for every member of this family. (See the next remarks below.)

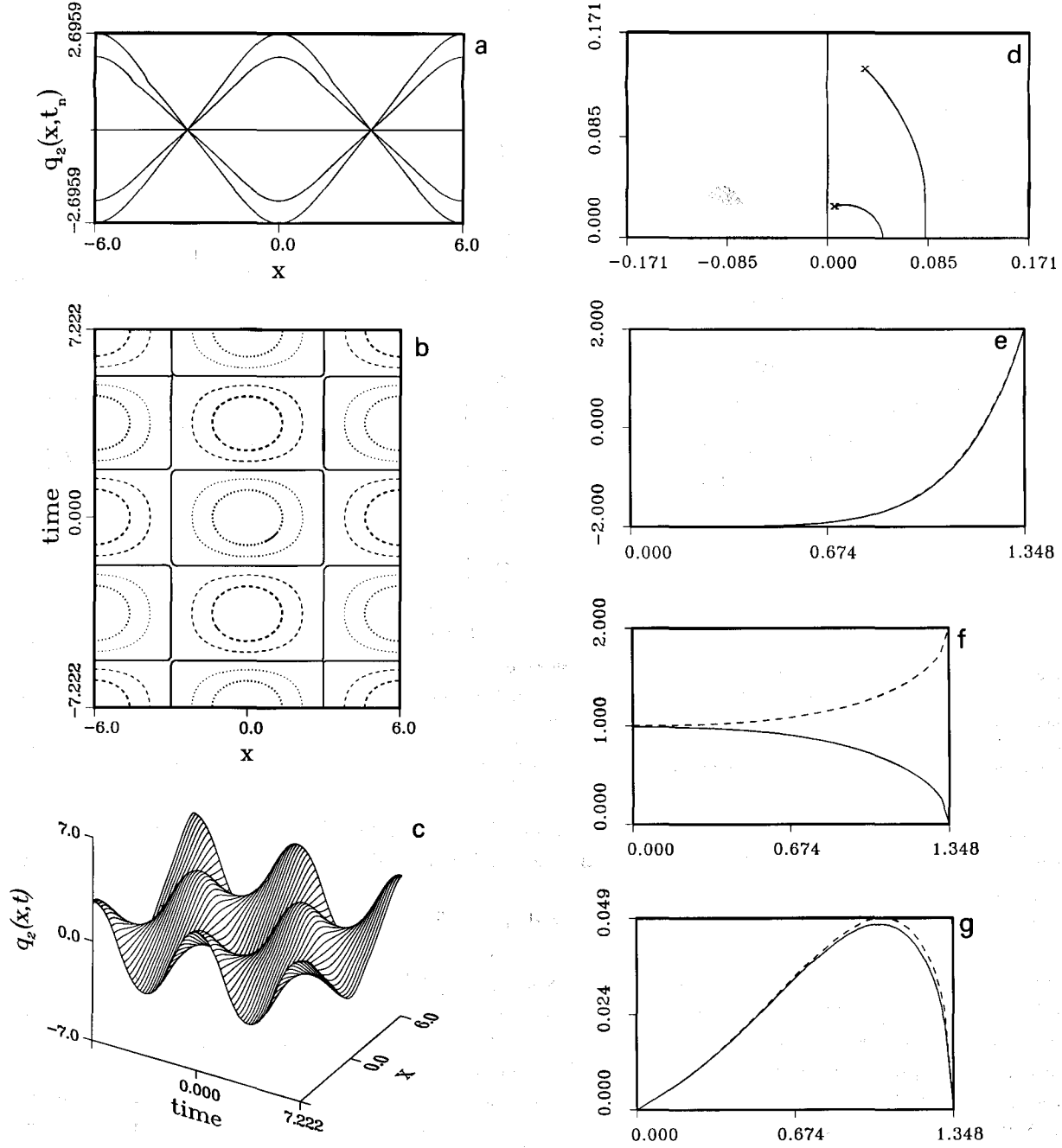


Fig. 19. For the two-phase solution with $E_1 = E_2^* = 0.027239 e^{i\pi(0.42907)}$, $E_3 = E_4^* = 0.143407 e^{i\pi(0.42907)}$, $L = 2\pi/|\kappa_1| = 12$, $\kappa_2 = \kappa_1$, $\omega_1 = -\omega_2 = 0.87$ we show (a) the spatial structure of $q_2(x, t_n)$ at selected times $t_n = n(T/8)$, $n = -4, -3, \dots, 4$, (b) contour levels of the surface $q_2(x, t)$, (c) the surface $q_2(x, t)$ over one x -period and two temporal periods, (d) the Floquet spectrum in the upper half plane, (e) $\Delta(E)$ along the complex bands of spectrum, (f) $(L/\pi) \int_{E_1}^{E_2} \Omega^{(x)}$ along the complex bands of spectrum, (g) $\text{Im}(\int_{E_1}^{E_2} \Omega^{(t)})$ along the complex bands of spectrum. In the contour plot, (b), we show five uniformly spaced contour levels, the dotted curves, the solid curves and the dashed curves correspond to $q_2 < 0$, $q_2 = 0$, $q_2 > 0$, respectively. In (d) the part of the spectrum along the positive real axis is not shown. In (e)–(g) the horizontal axis represents the polar angle of the points on the band of spectrum, the solid curves are for the left spine and the dashed curves are for the right spine of spectrum. The two spines are related by inversion through the circle of radius $\frac{1}{16}$. This symmetry is reflected in (e). The two curves in (g) should be identical, the difference reflects the numerical errors. The points of the spectrum were calculated to a relative accuracy of about 0.005.

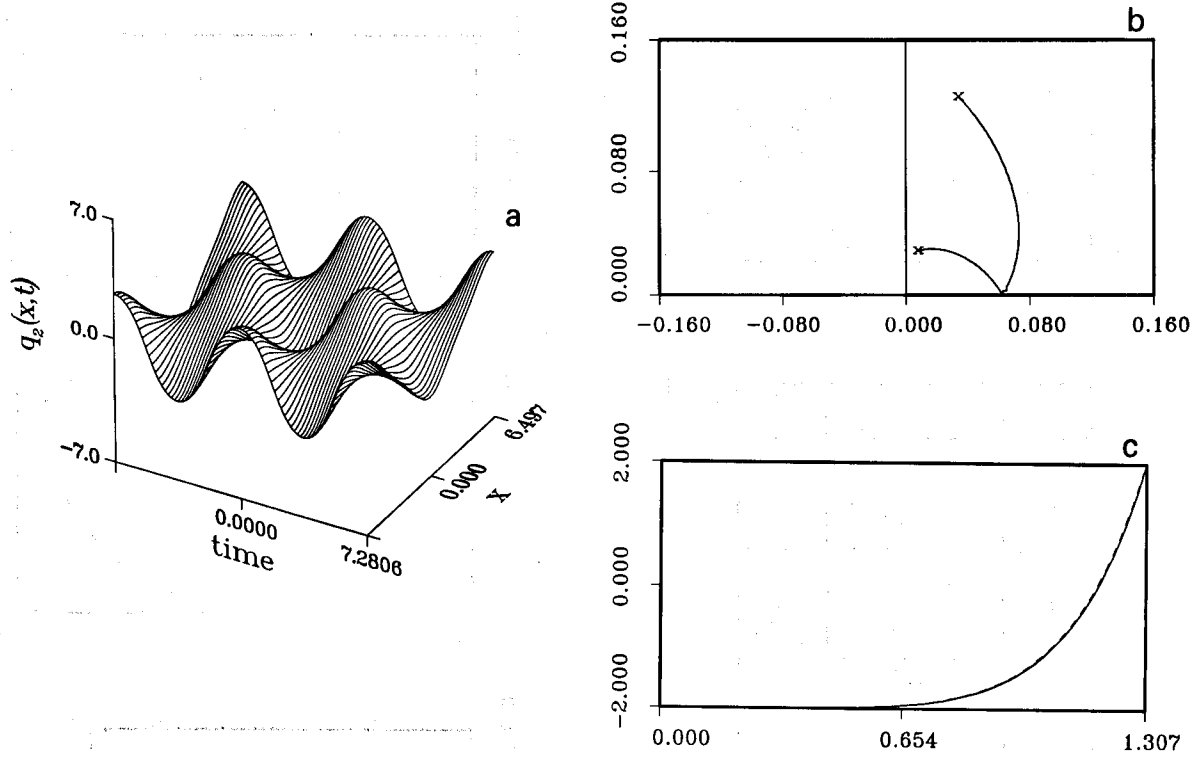


Fig. 20. For the two-phase solution with $E_1 = E_2^* = 0.03 e^{i\pi(0.41606)}$, $E_3 = E_4^* = 0.130208 e^{i\pi(0.41606)}$, $L = 2\pi/|\kappa_1| = 10.994$, $\kappa_2 = \kappa_1$, $\omega_1 = -\omega_2 = 0.863$, we show (a) the surface $q_2(x, t)$ over one x -period and two temporal periods, (b) the Floquet spectrum in the upper half plane, (c) $\Delta(E)$ along the bands of spectrum. In (b) the part of the spectrum along the positive real axis is not shown. In (c) the horizontal axis represents the polar angle of the points on the complex band of spectrum, the solid curves are for the left spine and the dashed curves are for the right spine. Note that the two spines of spectrum touch at $\frac{1}{16}$.

(vii) The intermediate spectral configuration between (v) and (vi) has $|E| = \frac{1}{16}$ as a third-order zero of the polynomial part of $\Omega^{(x)}$, so that $|\Delta| - 2 = \Delta' = \Delta'' = \Delta''' = \Delta^{(4)} = 0$ at $|E| = \frac{1}{16}$. Fig. 20 corresponds to this special case.

Fig. 19 depicts a breather train with all connected spectrum, and where $L = 12$, $\omega = 0.87$. As in figs. 17, we provide: (a) $q_2(x, t_n)$ at several times t_n , which clearly exhibit zero x -mean as well as the maximum amplitude $= 2\phi_1$, (b) contour plots of $q(x, t)$ which illustrate periodicity in x and t , (c) the surface $q_2(x, t)$ over one x -period and two t -periods, (d) the spectrum of (1.3) with potential $q_2(x, t)$ and the fundamental length $L^{(x)}$, which shows connected spectrum, (e) the graph of $L^{(x)} \int_{E_1}^E \Omega^{(x)}$ along the complex "spines" of spectrum, which shows no complex double points exist with $L = L^{(x)} = 12$, the fundamental length, (we emphasize this graph also determines the location of all double points for longer periods commensurate with $q_2(x, t)$, $L = L^{(n)} = nL^{(x)}$), (f) the growth rate σ_p associated to any complex double point E_p^d is then gleaned from $\text{Im}(\int_{E_1}^E \Omega^{(t)})$ where E is varied along spectrum. (Refer to the remarks above in example A.1.)

As we increase ϕ the bands of spectrum touch at $E = \frac{1}{16}$. We present the waveform (fig. 20a) and the spectrum (fig. 20b) of this case ($L = 14.562$). In fig. 21, the degenerate eigenvalue at $E = \frac{1}{16}$ has split into two complex double points, E_1^d, E_1^{d*} , each with modulus $\frac{1}{16}$ (labelled by a small circle on the spectral band). Note, however, from fig. 21e that the growth rate σ_1 vanishes at E_1^d , so that even these higher amplitude standing waves are neutrally stable on the fundamental period $L^{(x)}$.

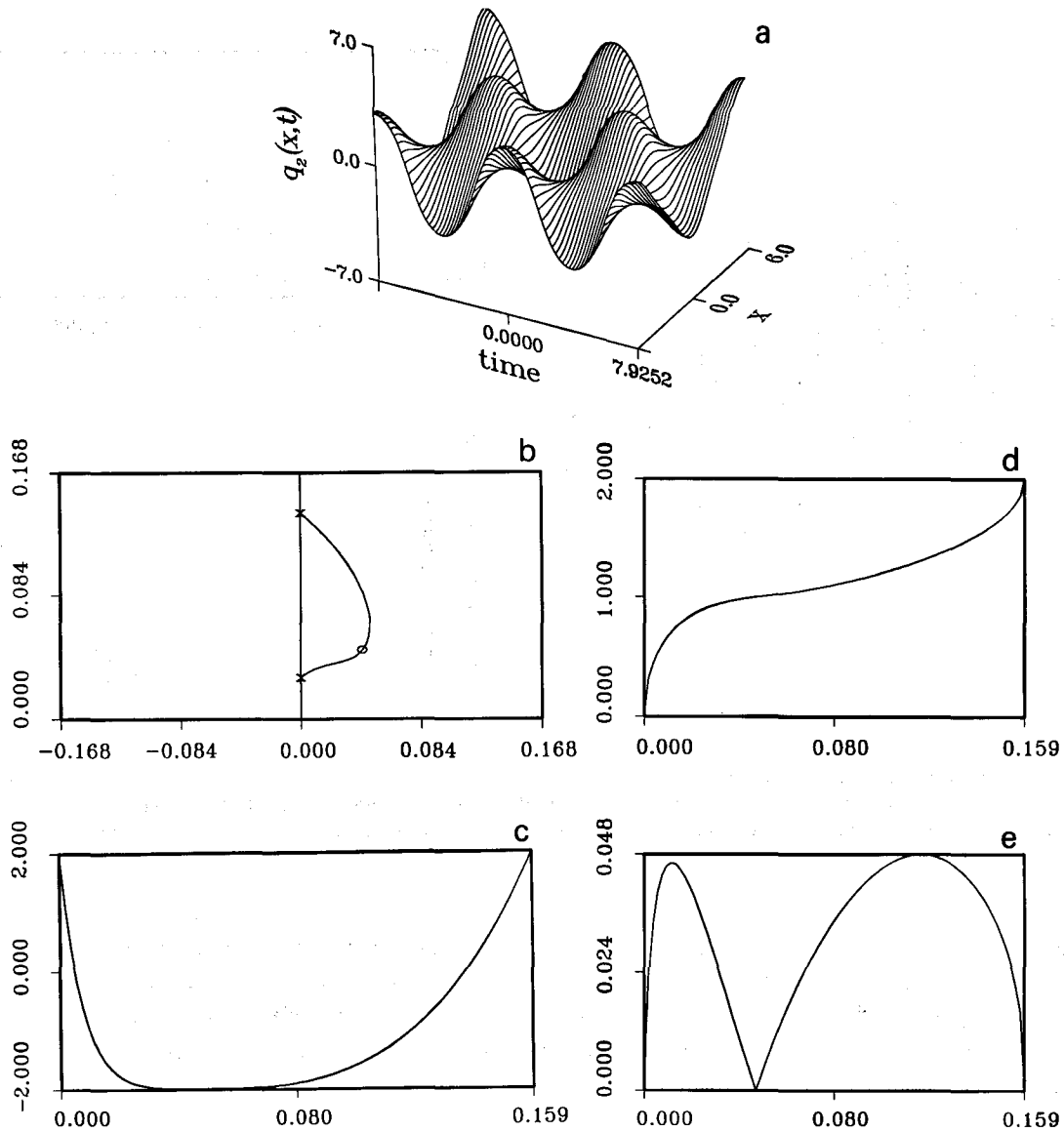


Fig. 21. For the two-phase solution with $E_1 = E_2^* = 0.027823 e^{i\pi/2}$, $E_3 = E_4^* = 0.140397 e^{i\pi/2}$, $L = 2\pi/|\kappa_1| = 12$, $\kappa_2 = \kappa_1$, $\omega_1 = -\omega_2 = 0.7928$ (a) the surface $q_2(x, t)$ over one x -period and two temporal periods, (b) the spectrum in the upper half plane, (c) $\Delta(E)$ along the complex band of spectrum (d) $(L/\pi) \int_{E_1}^E \Omega(x)$ along the complex band spectrum, (e) the absolute value of $\text{Im}(\int_{E_1}^E \Omega(t))$ along the complex band spectrum. In (b) the part of the spectrum along the positive real axis is not shown. In (c)–(e) the horizontal axis represents the arclength from E_1 . In (b) the circle represents a complex double point for $L = 12$. The double point lies on the circle of radius $\frac{1}{16}$, and from (e) the linearized growth rate is zero.

Remark. While the growth rate is zero in the mode labelled by E_1^d, E_1^{d*} , nonetheless a small perturbation of $q_2(x, t)$ will generically break E_1^d into a pair of simple spectra E_1^\pm , and the perturbed wave will have two additional phases θ_1^\pm , with amplitudes proportional to the phases of E_1^\pm . The zero growth rate in this mode labelled by E_1^d reflects that it will take $\mathcal{O}(1)$ time units for a small perturbation of $q_2(x, t)$ to evolve $\mathcal{O}(1)$ distance away from $q_2(x, t)$ in the x -function space, rather than occur exponentially fast as with nonzero growth rates.

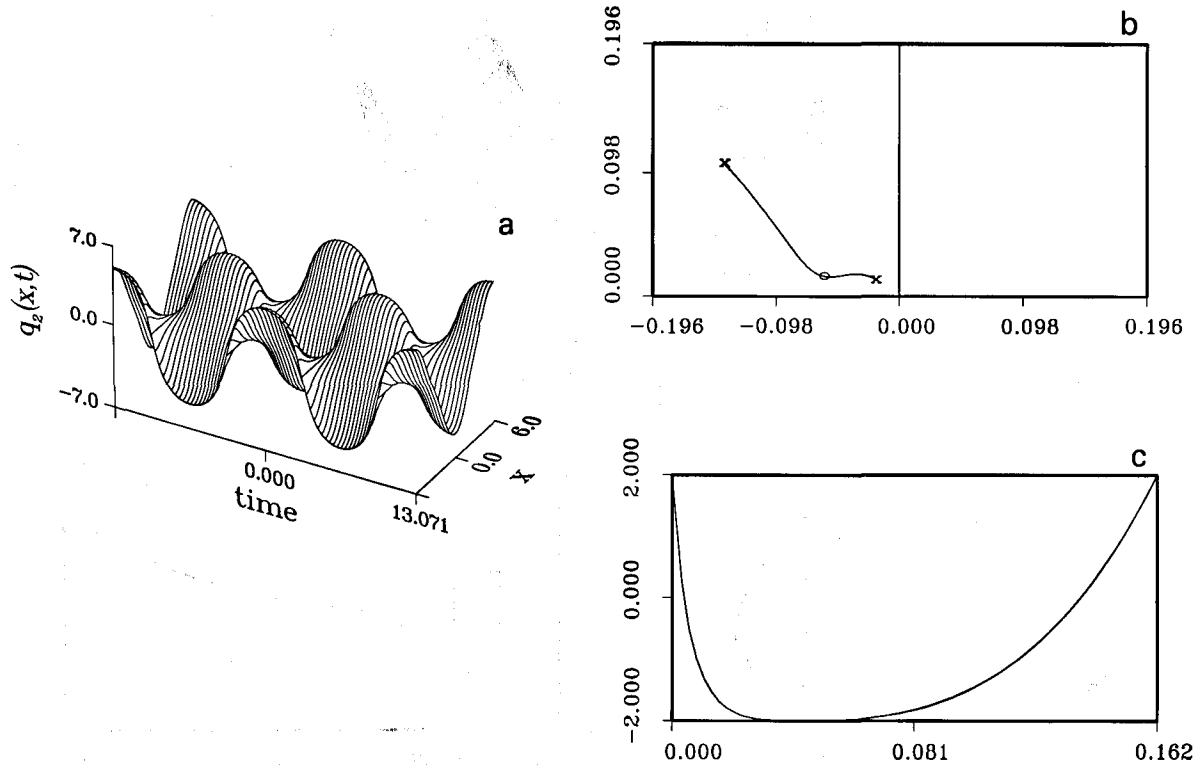


Fig. 22. For the two-phase solution with $E_1 = E_2^* = 0.022543 e^{i\pi(0.79444)}$, $E_3 = E_4^* = 0.173277 e^{i\pi(0.79444)}$, $L = 2\pi/|\kappa_1| = 12$, $\kappa_2 = \kappa_1$, $\omega_1 = -\omega_2 = 0.4807$ (a) the surface $q_2(x, t)$ over one x -period and two temporal periods, (b) the spectrum in the upper half plane, (c) $\Delta(E)$ along the complex band of spectrum, the horizontal axis is the arc length from E_1 along the spectrum. The circle in (b) is a complex double point of modulus $\frac{1}{16}$, with zero growth rate.

Remark. This family of 2-phase examples provides the first conclusive evidence that *nonreal double periodic eigenvalues are necessary for linearized instability but not sufficient*. In ref. [17], we prove the necessity of nonreal E_j^d for instability, but could only conclude that one of the flows which commute with sine-Gordon must be unstable. We have not confirmed this yet with the higher commuting flows for these examples.

In fig. 22 we increase the amplitude (i.e., increase $\phi_1 = \phi_2$) sufficiently so that the neutrally stable complex double points almost merge at $E = -\frac{1}{16}$, whereas $\phi_1 = 143\pi/180$ is not yet near the singular limit (soliton limit) corresponding to $E_1 = E_3$, $E_2 = E_4 \in \mathbb{R}^-$.

For larger ϕ_1 , fig. 23, the two complex double points have already collided at $-\frac{1}{16}$ into a fourth-order periodic eigenvalue, then split back into double points and traveled along the negative real E -axis in order to preserve the symmetry $E_1^d = 1/16^2 E_2^d$. This final spectral configuration with two vertical bands of spectrum corresponds to a very large amplitude breather train as the fig. 23 indicates.

The two examples shown in figs. 24, 25 show the effect of changing $|E_1|$ for a fixed value of $\phi_1 = \phi_2 = \pi/3$.

Example A.3. Standing kink-kink and kink-antikink trains

When each $E_j \in \Sigma_{N=2}^{(s)}$ is negative real, corresponding to a nonlinear superposition of two kink modes, or a kink and antikink, or two antikink modes, then the symmetry (6.7a) reduces $\Sigma_{N=2}^{(s)}$ to a two-dimen-

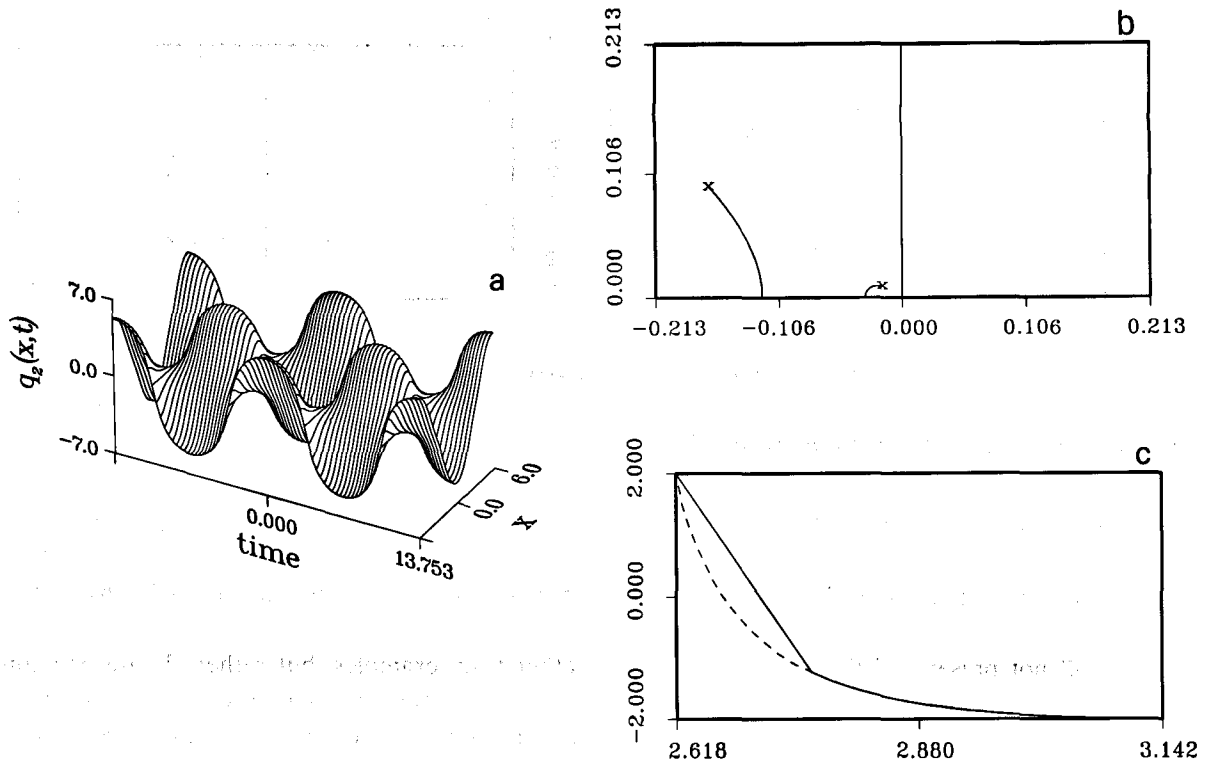


Fig. 23. For the two-phase solution with $E_1 = E_2^* = 0.020322 e^{i\pi(0.83333)}$, $E_3 = E_4^* = 0.192214 e^{i\pi(0.83333)}$, $L = 2\pi/|\kappa_1| = 12$, $\kappa_2 = \kappa_1$, $\omega_1 = -\omega_2 = 0.457$ we show (a) the surface $q_2(x, t)$ over one x -period and two temporal periods, (b) the spectrum in the upper half plane, (c) $\Delta(E)$ along the complex bands of spectrum.

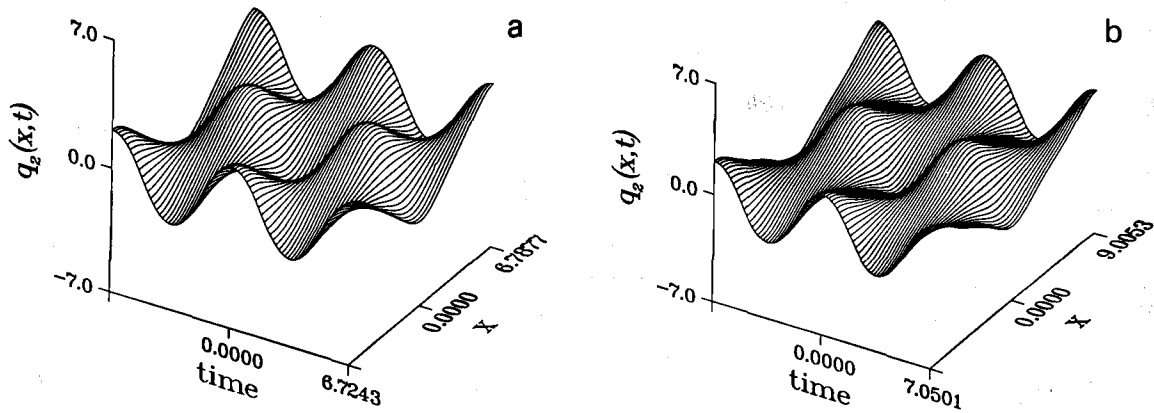


Fig. 24. The solution $q_2(x, t)$ with simple spectra (a) $E_1 = E_2^* = 0.03 e^{i\pi/3}$, $E_3 = E_4^* = 0.130208 e^{i\pi/3}$, (b) $E_1 = E_2^* = 0.04 e^{i\pi/3}$, $E_3 = E_4^* = 0.097656 e^{i\pi/3}$ are shown.

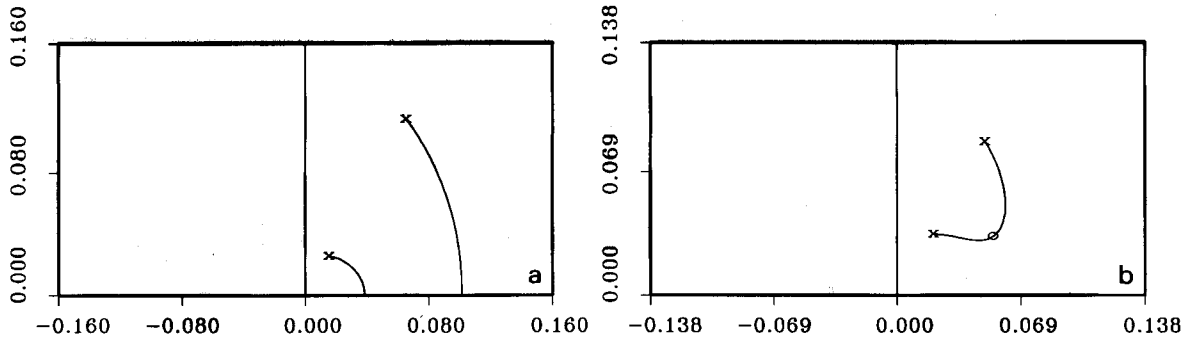


Fig. 25. The spectrum in the upper half plane associated with the solutions in fig. 24 are shown.

sional family parametrized by $\eta_1, \eta_2 \in \mathbb{R}^+$, with

$$E_1 = -\frac{1}{16} e^{\eta_1}, \quad E_2 = -\frac{1}{16} e^{-\eta_1}, \quad E_3 = -\frac{1}{16} e^{\eta_2}, \quad E_4 = -\frac{1}{16} e^{-\eta_2}. \quad (6.9)$$

The fixed period constraint, $L^{(x)} \equiv \text{constant}$ or $L^{(t)} \equiv \text{constant}$, yields a one-dimensional subset of (6.9), $\eta_2(\eta_1)$.

We will not present all the details as in the breather train examples, but rather choose one simple spectrum $\Sigma_{N=2}^{(s)}$ of the family (6.9), and display all four possible wavetrains with this spectrum. These 2^2 possibilities arise, we recall from section 3 and equations (6.22), (6.23a), since each phase θ_j may correspond to a kink or an antikink mode depending on whether $\text{Re}[(l_0)_j] = +\frac{1}{4}$ or $-\frac{1}{4}$, respectively.

Fig. 26 consists of the four standing two-phase wavetrains with spectrum of class (6.9), (26a) with $l_0 = (+\frac{1}{4}, +\frac{1}{4})$, (26b) with $l_0 = (+\frac{1}{4}, -\frac{1}{4})$, (26c) with $l_0 = (-\frac{1}{4}, +\frac{1}{4})$, then (26d) with $l_0 = (-\frac{1}{4}, -\frac{1}{4})$. Note that (26a), (26d) correspond to kink-kink, antikink-antikink standing waves, while (26b), (26c) are kink-antikink bound states.

6.2. Two-phase periodic breathers with $\kappa_2 = 2\kappa_1$

Next we seek to generate periodic breather trains where $\Sigma_{N=2}^{(s)}$ satisfy the period constraints (6.6) for small values of n_1, n_2 . Section 6.1 exhausts $n = 0, \pm 1$. We now illustrate cases where $n_1 = 1, n_2 = 2$.

We remark that these solutions break the symmetry $E_j \rightarrow 1/16^2 E_j$, and likewise break the standing wave constraint, inducing translational degrees of freedom.

We search for elements of

$$\{\Sigma_{N=2}^{(s)} | n_1 \kappa_2 = n_2 \kappa_1\} \quad (6.10)$$

by deformation of elements of the family (6.8a), (6.8b). For example, we take $E_1 = r e^{i\phi}$, $E_2 = r e^{-i\phi}$, $E_3 = s e^{i\phi}$ and $E_4 = s e^{-i\phi}$, with $s = \tau/16^2 r$, where $\tau = 1$ belongs in the family (6.8a). Fig. 27 shows the behavior of κ_1/κ_2 as a function of τ . Clearly, this family includes $n_1 \kappa_2 = n_2 \kappa_1$, $n_1, n_2 \in \mathbb{Z}$. However, $L^{(x)}$ changes as we vary τ . By varying both r and s , we can obtain specific values of $L^{(x)}$. Fig. 28 depicts one such periodic breather wave train with $\kappa_2 = 2\kappa_1$ and $L^{(x)} = 12$, along with spectral information. Note that this example has one pair of complex double points $(E_1^{(d)}, E_1^{(d)*})$, with $E_1^{(d)} = (0.266, 0.218)$ and growth rate $\sigma = 0.035$, so that this solution is unstable.

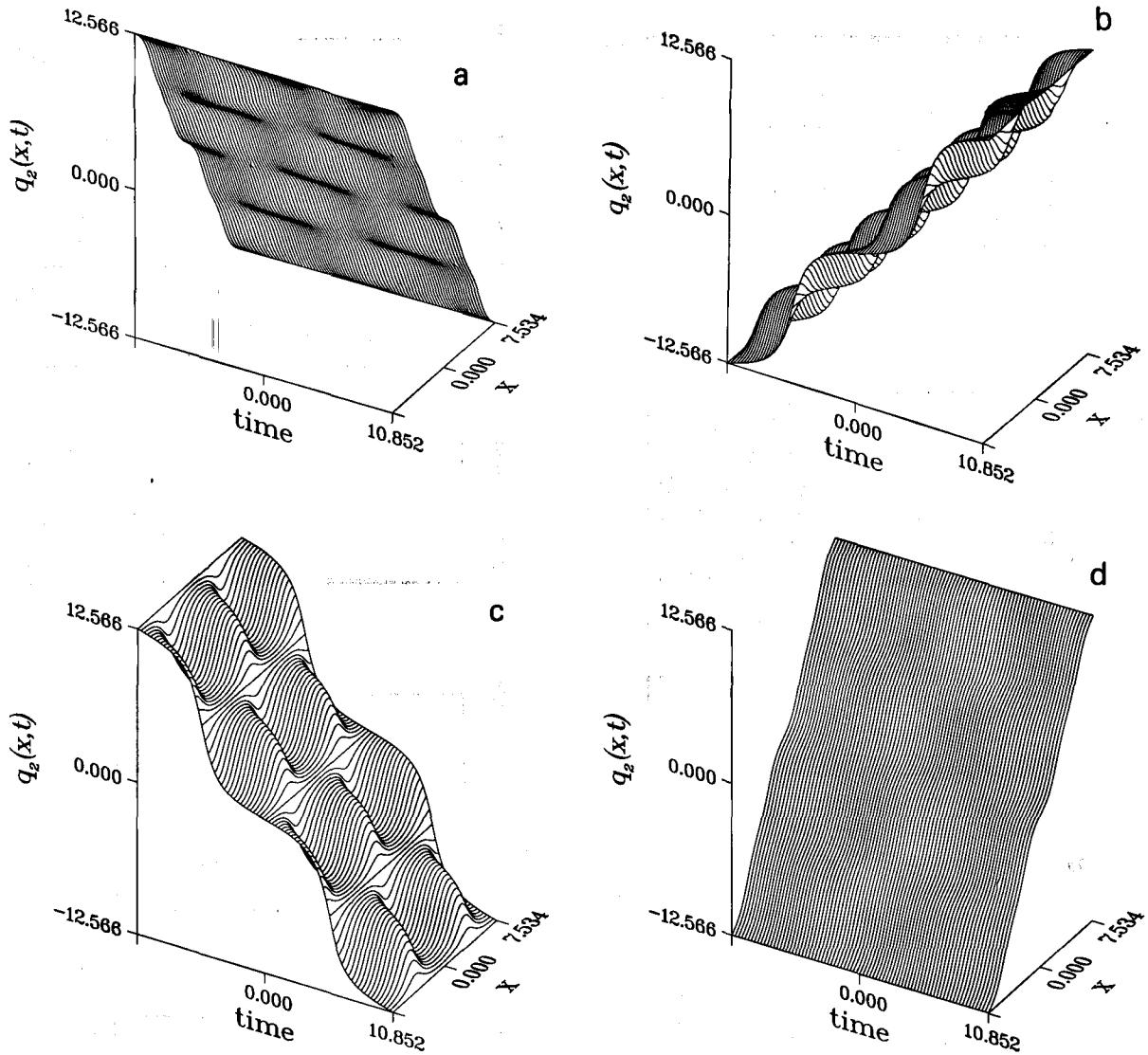


Fig. 26. Two-phase (a) kink-kink, (b) kink-antikink, (c) antikink-kink and (d) antikink-antikink solutions are shown for one spatial and two temporal periods. The simple spectrum is $E_1 = -0.195312$, $E_2 = -0.097656$, $E_3 = -0.04$, $E_4 = -0.02$.

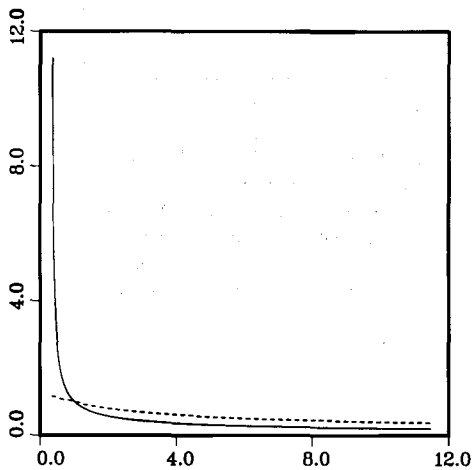


Fig. 27. We consider a simple spectrum with $E_1 = r e^{i\phi}$, $E_2 = r e^{-i\phi}$, $E_3 = s e^{i\phi}$ and $E_4 = s e^{-i\phi}$. Here we show the variation of κ_1/κ_2 and ω_1/ω_2 as s is changed with r, ϕ fixed. κ_1/κ_2 (solid curve) and $-\omega_1/\omega_2$ (dashed curve) are plotted against τ , with $s = \tau/16^2 r$, for $r = 0.03$ and $\phi = \pi/3$. Note that $\tau = 1$ belongs in the family (6.8a) for which $\kappa_1 = \kappa_2$ and $\omega_1 = -\omega_2$.

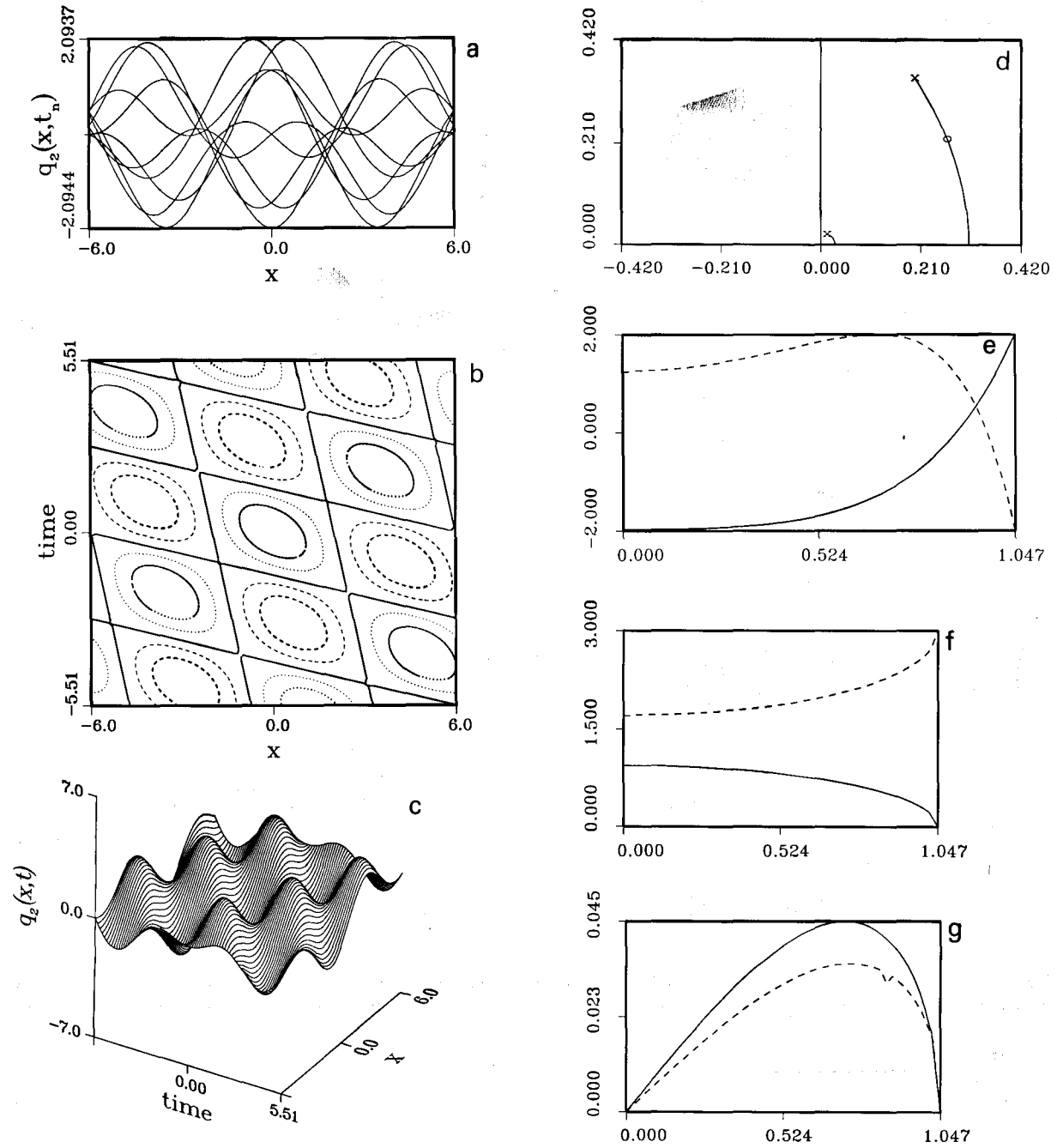


Fig. 28. For the two-phase solution with $E_1 = E_2^* = 0.025214 e^{i\pi/3}$, $E_3 = E_4^* = 0.394631 e^{i\pi/3}$, $L = 2\pi/|\kappa_1| = 12$, $\kappa_2 = 2\kappa_1$, $\omega_1 = 0.96$, $\omega_2 = -0.13206$, we show (a) the spatial structure of $q_2(x, t_n)$ at selected times $t_n = n(T/8)$, $n = -4, -3, \dots, 4$, $T = 5.51$, (b) contour levels of the surface $q_2(x, t)$, (c) the surface $q_2(x, t)$, (d) the spectrum in the upper half plane, (e) $\Delta(E)$ along the bands of spectrum, (f) $(L/\pi) \int_{E_1}^E \Omega^{(x)}$ along the bands of spectrum, (g) $\text{Im}(\int_{E_1}^E \Omega^{(t)})$ along the spectrum. In (d) the part of the spectrum along the positive real axis is not shown. In (e)–(g) the horizontal axis represents the polar angle of the points on the band of spectrum, the solid curves are for the left spine and the dashed curves are for the right spine of the spectrum. Note that the solution is quasiperiodic in time.

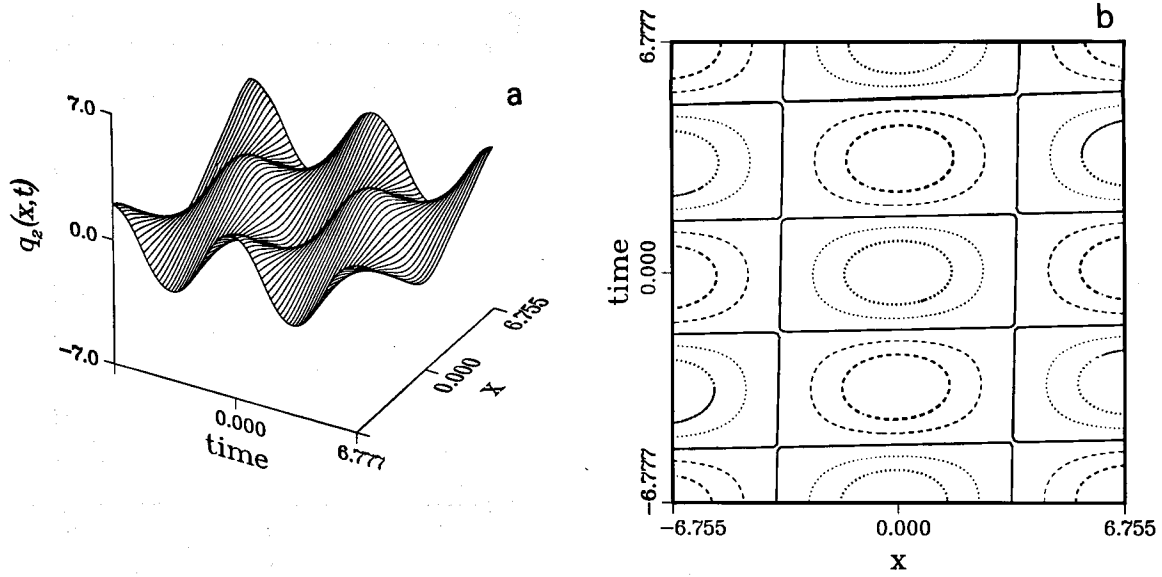


Fig. 29. For the two-phase solution with $E_1 = E_2^* = 0.03 e^{i\pi/3}$, $E_3 = E_4^* = 0.12 e^{i\pi/3}$, $\kappa_1 = -0.46506$, $\kappa_2 = -0.42722$, $\omega_1 = 0.93627$, $\omega_2 = -0.91806$, we show (a) the surface $q_2(x, t)$, (b) contour levels of the surface $q_2(x, t)$.

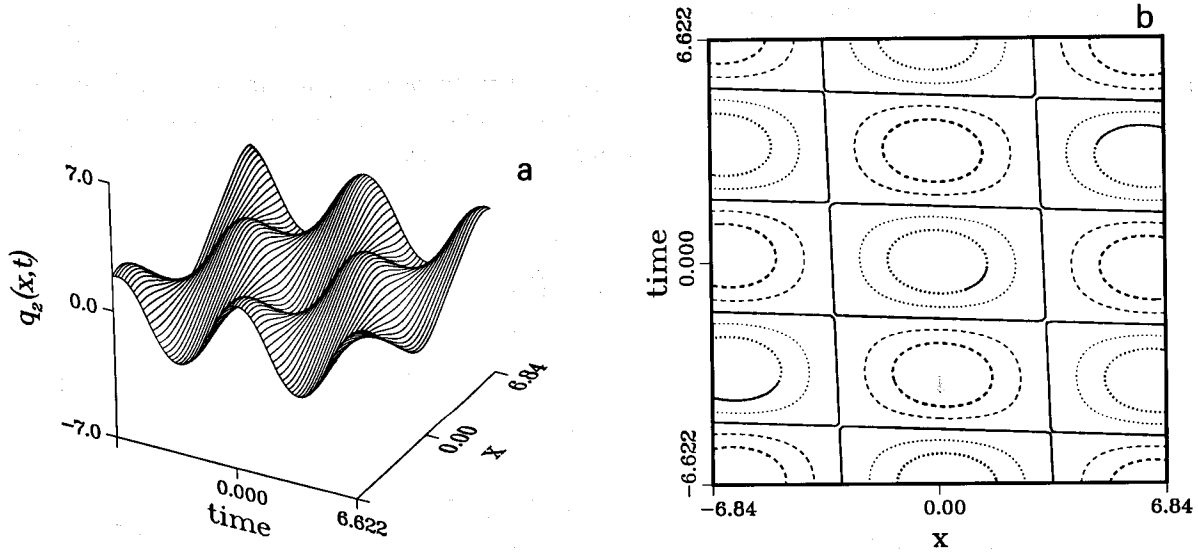


Fig. 30. For the two-phase solution with $E_1 = E_2^* = 0.03 e^{i\pi/3}$, $E_3 = E_4^* = 0.15 e^{i\pi/3}$, $\kappa_1 = -0.45929$, $\kappa_2 = -0.52639$, $\omega_1 = 0.93147$, $\omega_2 = -0.96632$ we show (a) the surface $q_2(x, t)$, (b) contour levels of the surface $q_2(x, t)$. Observe that the solutions in fig. 29 and this figure are quasiperiodic in x and t . $E_3 = 0.130208 e^{i\pi/3}$ belongs in class (4.8a). Note the deformation of the “fundamental period parallelogram” in the contour plots.

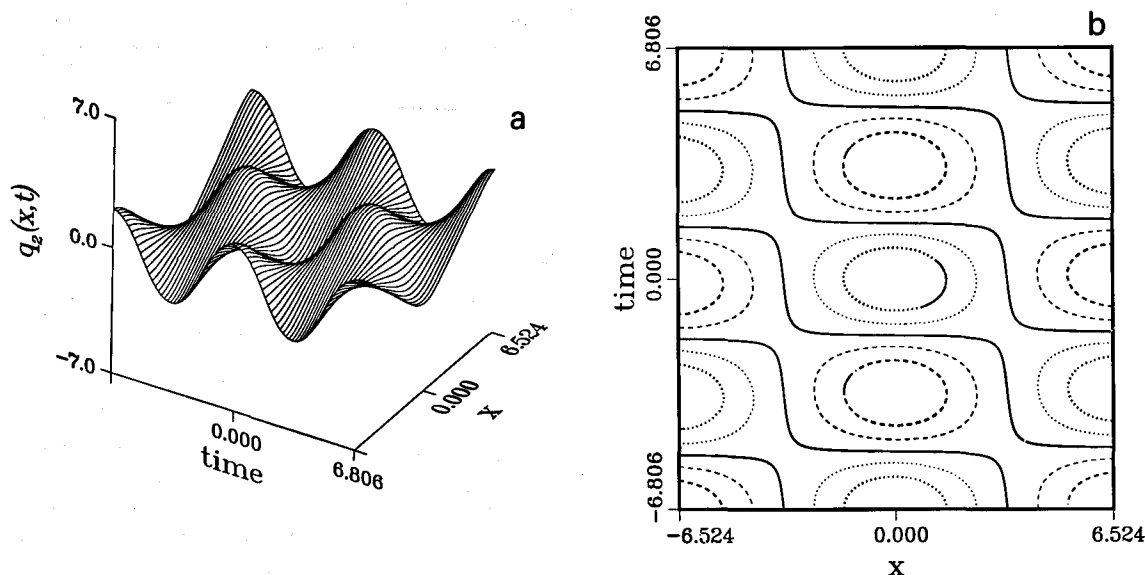


Fig. 31. For the two-phase solution with $E_1 = E_2^* = 0.03 e^{i\pi/3}$, $E_3 = E_4^* = 0.130208 e^{i\pi(0.36111)}$, $\kappa_1 = -0.48151$, $\kappa_2 = -0.45260$, $\omega_1 = 0.92423$, $\omega_2 = -0.92207$, we show (a) the surface $q_2(x, t)$, (b) contour levels of the surface $q_2(x, t)$.

6.3. Two-phase, x and t quasiperiodic breather trains

If we choose arbitrary $\Sigma_{N=2}^{(s)}$, the wavenumbers κ_1, κ_2 and frequencies ω_1, ω_2 are generically incommensurate. Machine arithmetic yields all commensurate values, of course, but the periods are likely to be quite large. For moderate space and time scales, the wavetrains are quasiperiodic in x and t . We depict four such wavetrains in figs. 29–32.

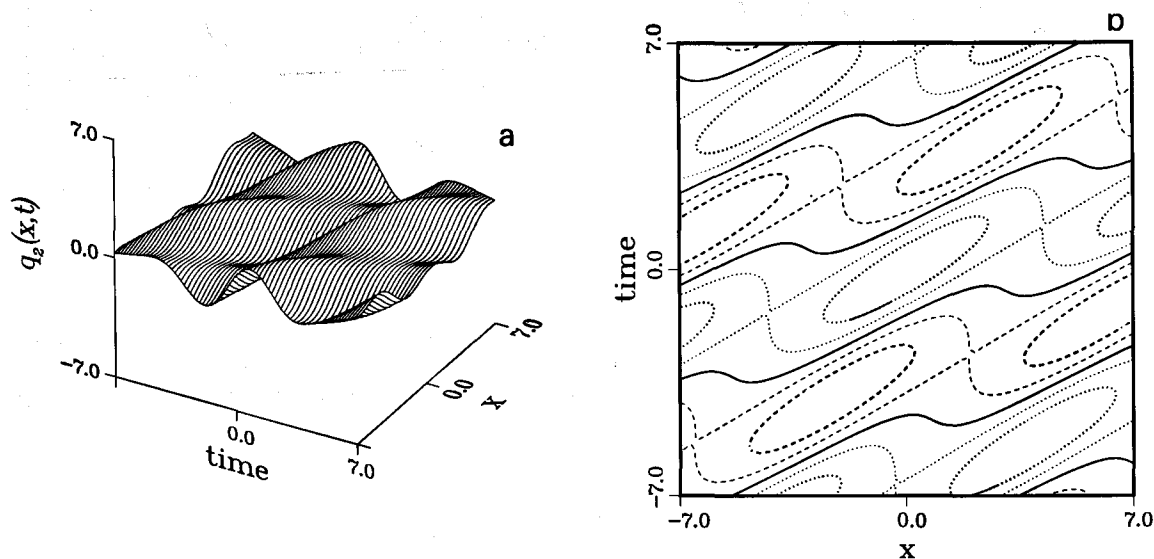


Fig. 32. For the two-phase solution with $E_1 = E_2^* = 0.01 e^{i\pi/6}$, $E_3 = E_4^* = 0.03 e^{i\pi/3}$, $\kappa_1 = -1.2033$, $\kappa_2 = 0.30046$, $\omega_1 = 1.4697$, $\omega_2 = -0.95417$, we show (a) the surface $q_2(x, t)$, (b) contour levels of the surface $q_2(x, t)$.

The first three examples correspond to small perturbations of the simple spectrum with $E_1 = 0.03 e^{i\pi/3}$ from the family (6.8a). Fig. 32 shows the solution for an arbitrarily chosen simple spectrum.

The spectral theoretic and stability calculations relevant for x -periodic solutions do not apply for these solutions. *However*, the meromorphic differentials $\Omega^{(x)}$ and $\Omega^{(t)}$ are still defined, and play fundamental roles in the modulation theory of these two-phase quasiperiodic wavetrains [19, 20], both for the perturbed and unperturbed sine-Gordon equations. Applications of our codes to modulations of x - and t -quasiperiodic wavetrains consisting of all kink-like modes are planned. These studies are relevant for the generation of new phases as the modulation equations develop shocks.

7. Special examples of three-phase solutions

We now display some selected three-phase x -periodic wavetrains. These sine-Gordon solutions correspond to choices of simple periodic spectrum, $\Sigma_{N=3}^{(s)}$, which have been measured via the direct spectral transform in numerical studies [10, 11] of chaotic attractors for the damped and periodically driven s-G equation. On an x -interval of length 12 for specific perturbation parameter values, the space-time attractor in ref. [11] consists of a chaotic flow among coherent spatial waveforms. Overman's DST code [15, 16] indicates that at each time step t_n these waveforms are remarkably well approximated by a three-phase simple periodic spectrum, $\Sigma^{(s)}(q(x, t_n)) \approx \Sigma_{N=3}^{(s)}$.

There are two essential nondegenerate types of $\Sigma_{N=3}^{(s)}$ observed, described in cases 1 and 2 below, in which the continuous spectrum is either connected (a "cross" spectrum) or disconnected (a "gap" spectrum). These two types of three-phase simple spectra are "separated" by a degenerate one-phase spectrum, $\Sigma_{N=1}^{(s)}$, in which two pairs of simple periodic eigenvalues have coalesced off the real axis to create a conjugate pair of nonreal double periodic eigenvalues. *This degenerate simple spectrum $\Sigma_1^{(s)}$ corresponds both to s-G solutions which are unstable single-phase wavetrains and to homoclinic three-phase wave-trains which are homoclinic (as $|t| \rightarrow \infty$) to the single-phase solution.* These homoclinic solutions are intermediate states between the three-phase solutions of case 1 and case 2.

Our motivation in this section is to: (i) provide two types of sets $\Sigma_{N=3}^{(s)}$ which are bona fide simple periodic spectral sets on an x -interval of length $L = 12$; (ii) graph the wavetrains for each type of $\Sigma_{N=3}^{(s)}$; (iii) find near-homoclinic limits of $\Sigma_{N=3}^{(s)}$ for period $L = 12$ which are nearby a homoclinic single-phase spectrum $\Sigma_{N=1}^{(s)}$ with one pair of nonreal double periodic eigenvalues.

In each case below, we begin with the DST data from Overman's code which yields $\Sigma_{N=3}^{(s)}$ on length $L = 12$ for which the fixed $L = 12$ constraints, (3.9d), are satisfied to within five decimal places. Overman's PDE integrator imposes even boundary conditions in x , which forces the continuous spectrum (and the discrete periodic spectrum) to obey the symmetry

$$E_j \in \Sigma^{(p)} \Rightarrow 1/16^2 E_j \in \Sigma^{(p)}. \quad (7.1)$$

This symmetry allows for two classes of $\Sigma_{N=3}^{(s)}$ (recall eq. 6.8 for $N = 2$) given by

$$\Sigma_{N=3}^{(s)} = \{E_1 = E_2^* = \frac{1}{16} e^{i\phi_1}, E_3 = E_4^* = r e^{i\phi_2}, E_5 = E_6^* = (1/16^2 r) e^{i\phi_2}, 0 < \phi_1, \phi_2 < \pi, 0 < r < \frac{1}{16}\} \quad (7.2a)$$

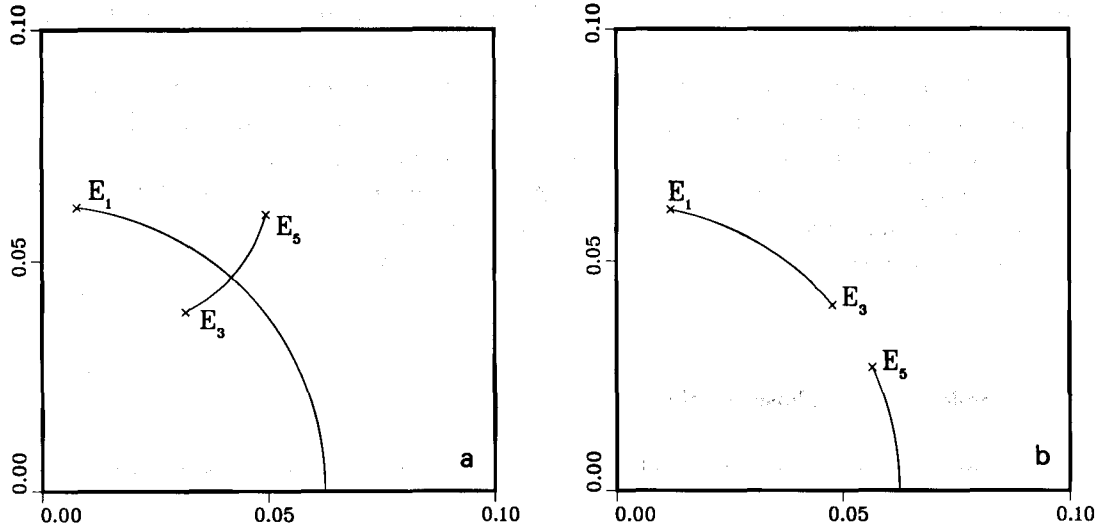


Fig. 33. The qualitative structure of the spectrum (in the upper half plane) with the symmetry (7.1) is shown: (a) the “cross” configuration, for eq. (7.2a), and, (b) the “gap” configuration, for eq. (7.2b).

and

$$\Sigma_{N=3}^{(s)} = \{E_j = \frac{1}{16} e^{i\phi_j}, j = 1, \dots, 6, \phi_{2j} = -\phi_{2j+1}\}. \quad (7.2b)$$

The symmetry (7.1) on the entire continuous spectrum restricts the curves of spectrum to a small number of possibilities. We have not yet implemented the direct computation of the spectrum via Hochstadt’s formula (4.2) for $N = 3$. Therefore while we know the qualitative structure of the spectral curves, we do not have the IST linearized stability information for this class of solutions. Nonetheless, Overman’s DST codes indicate the spectrum for (7.2a) is the “cross” configuration (fig. 33a) and the “gap” configuration (fig. 33b) for (7.2b), with no nonreal double periodic eigenvalues for length $L = 12$ (thus no instabilities).

Case 1. A 3-phase “cross” spectral configuration with connected Σ

$$\Sigma_{N=3}^{(s)} = \{E_1 = \frac{1}{16} e^{i\phi_1}, E_3 = r e^{i\phi_2}, E_5 = (1/16^2 r) e^{i\phi_2}, E_{2j}^* = E_{2j-1}, j = 1, 2, 3, \\ \phi_1 = 0.50943\pi, \phi_2 = 0.32901\pi, r = 0.056783\}. \quad (7.3a)$$

The IST algorithm from section 3 is implemented to yield

$$\kappa_1 = -\kappa_2 = 0.5236352, \quad \kappa_3 = 0, \quad (7.3b)$$

$$\omega_1 = -0.852612, \quad \omega_2 = 0.705324, \quad \omega_3 = 0.778968. \quad (7.3c)$$

From (3.9d), we verify the fixed period $L = 12$ constraints are satisfied. The corresponding theta function solution $q_3(x, t)$ is depicted in fig. 34 corresponding to the qualitative spectrum in fig. 33a, drawn by hand. We note that the waveform flows between a breather localized in the center of the interval and a breather localized at the ends of the interval. (We have selected the phase shifts θ_j^0 , $j = 1, 2, 3$, so that $q_3(x, t)$ is an even function of x for all t .)

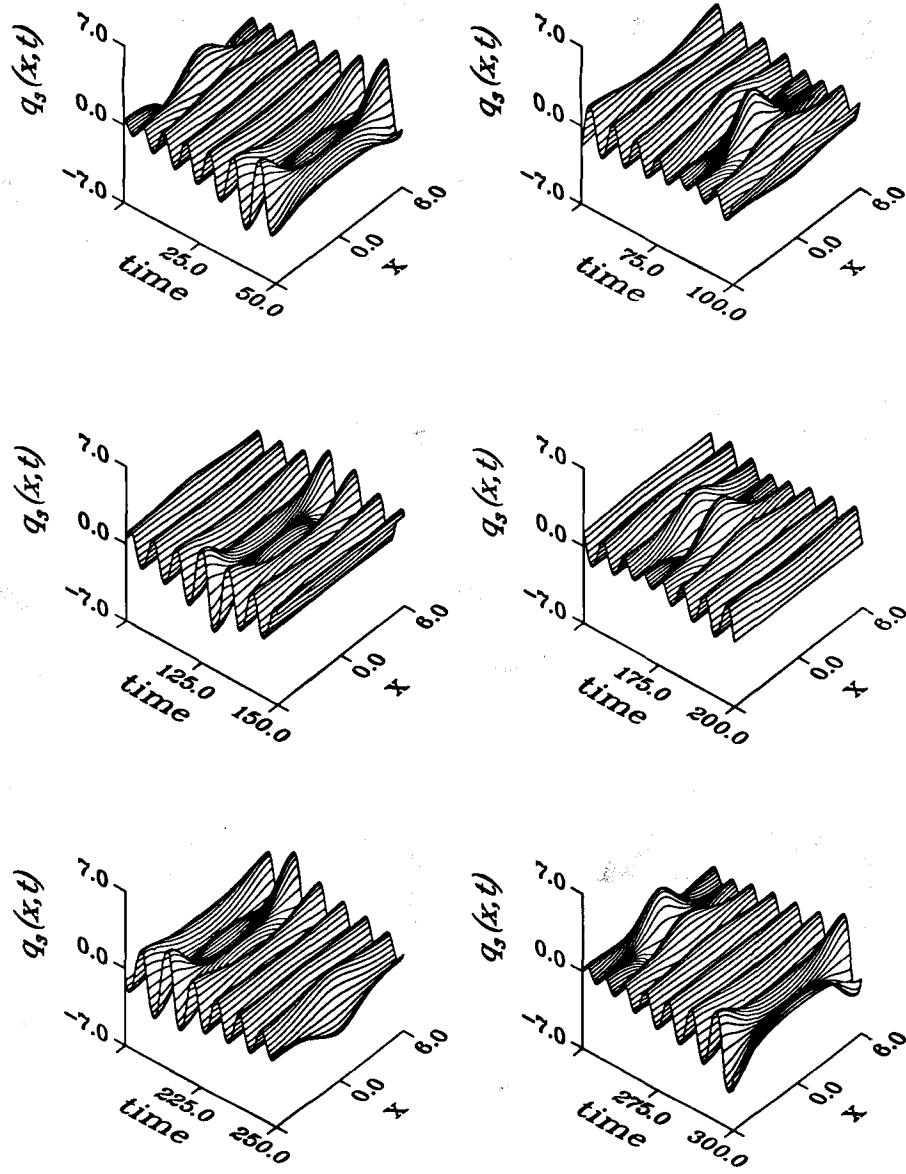


Fig. 34. The three-phase solution with simple spectrum given by eq. (7.3a) is shown.

Case 2. A 3-phase “gap” spectral configuration with disconnected Σ

$$\Sigma_{N=3}^{(s)} = \left\{ E_j = \frac{1}{16} e^{i\phi_j}, j = 1, \dots, 6, \phi_{2j} = -\phi_{2j-1}, \phi_1 = 0.40264\pi, \phi_3 = 0.231995\pi, \phi_5 = 0.07804\pi \right\}. \quad (7.4a)$$

The IST algorithm is implemented to find

$$\kappa_1 = 0.52362, \quad \kappa_2 = -0.52362, \quad \kappa_3 = 0, \quad (7.4b)$$

$$\omega_1 = -0.97769, \quad \omega_2 = -\omega_3 = 0.86935. \quad (7.4c)$$

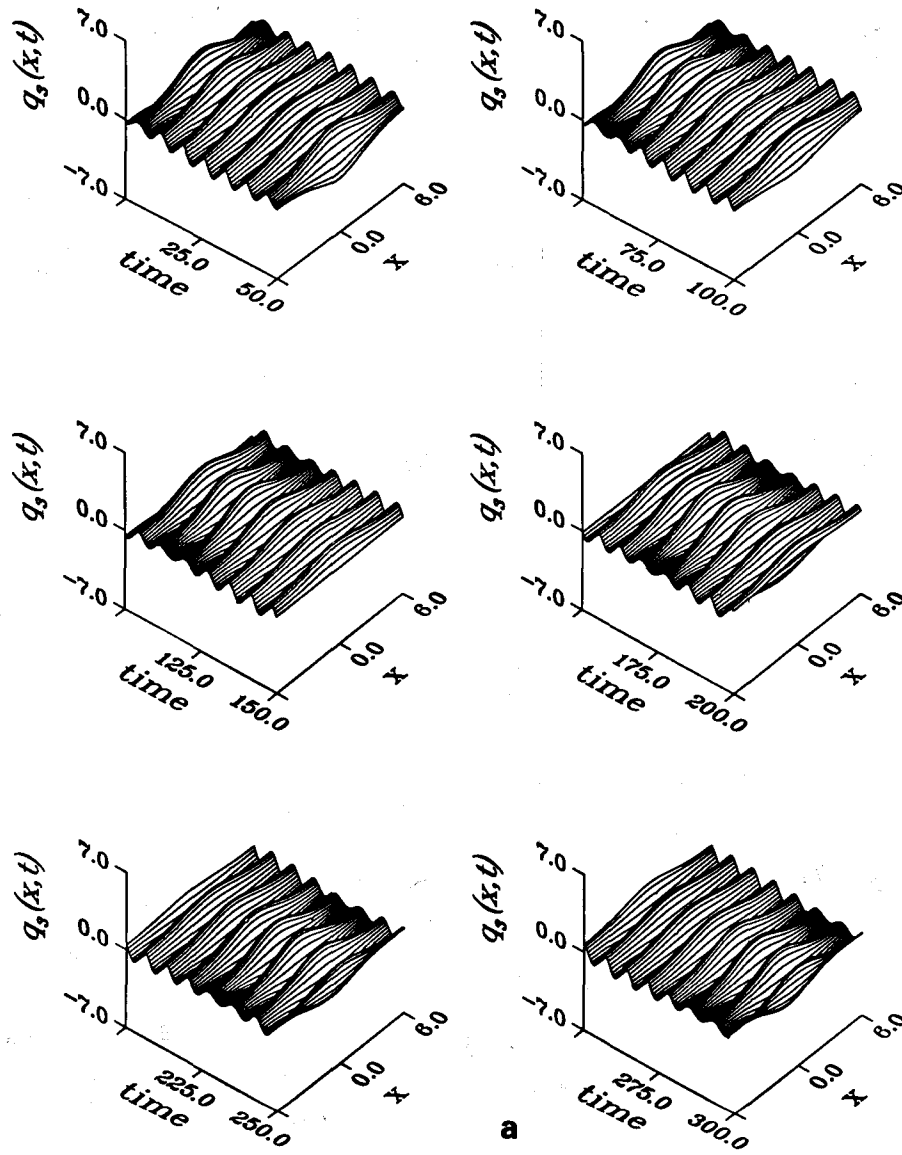


Fig. 35. The three-phase solution with simple spectrum given by eq. (7.4a) is shown. The two solutions correspond to the two choices for the phase shifts which guarantee evenness of $q_3(x, t)$ as a function of x for all t . The two solutions are related by a translation in x by half a period. For our choice of the phase shifts, the solution is an even function of t also.

For this “gap” spectrum (fig. 33b), there are two discrete choices of θ_j^0 which guarantee evenness of $q_3(x, t)$ as a function of x for all t . Figs. 35a, 35b display these two discrete even three-phase periodic solutions: fig. 35a with the breather oscillating in the center of the interval for all time, fig. 35b with the breather oscillating in the ends of the interval for all time.

Case 3. “Near homoclinic” spectral configurations

In this example, we consider the limit $E_3 \approx E_5$ and $E_4 \approx E_6$, so that the periodic spectrum is *very close* to a one-phase simple periodic spectrum, $\Sigma_{N=1}^{(s)} = \{\frac{1}{16} e^{i\phi_1}, \frac{1}{16} e^{-i\phi_1}\}$, for which $E_3 \equiv E_5 = E_1^d$, $E_4 \equiv E_6 =$

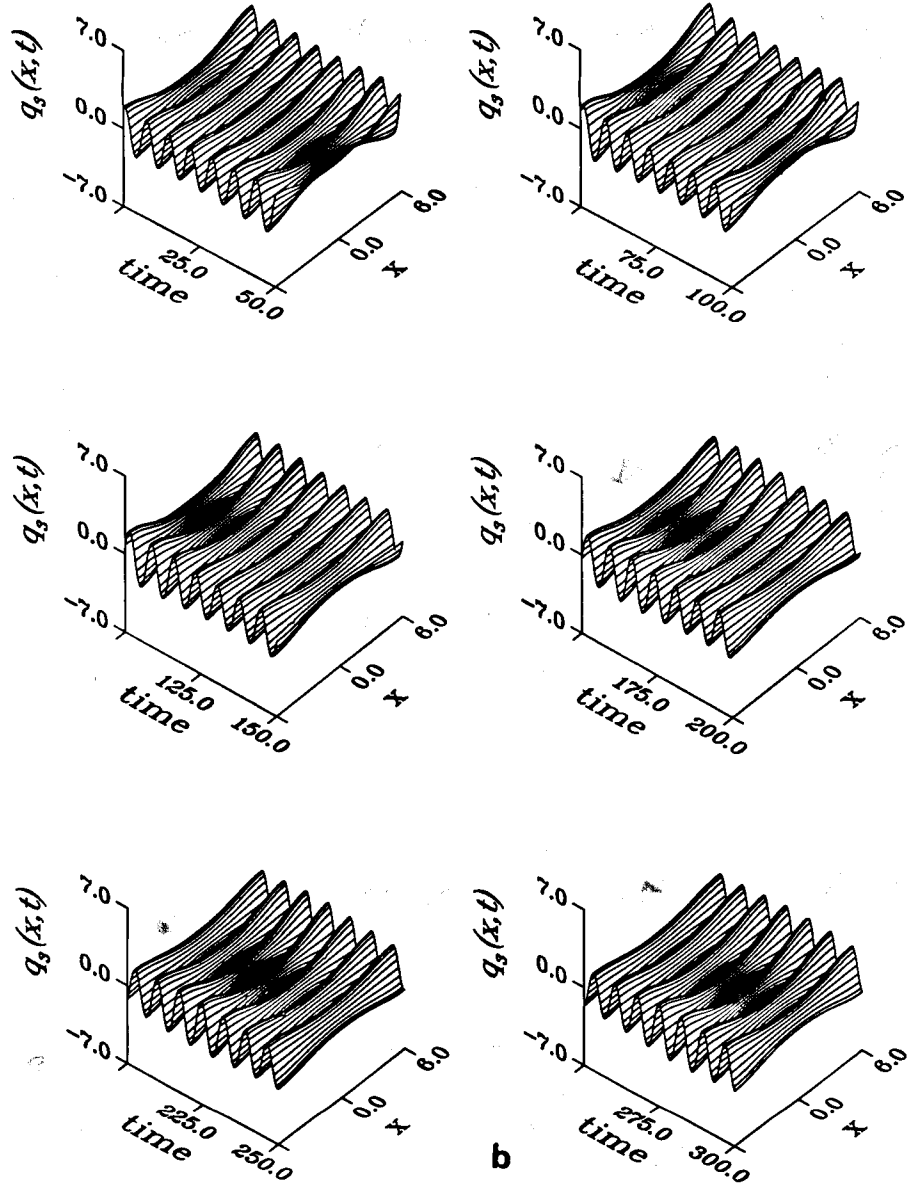


Fig. 35. (continued)

$(E_1^d)^*$ are complex double periodic eigenvalues.

Near-homoclinic gap configuration

$$\Sigma_{N=3}^{(s)} = \{E_j = \frac{1}{16} e^{i\phi_j}, j=1, \dots, 6, \phi_{2j} = -\phi_{2j-1}, \phi_1 = 0.461011\pi, \phi_3 = 0.266372\pi, \phi_5 = 0.265797\pi\}. \quad (7.5a)$$

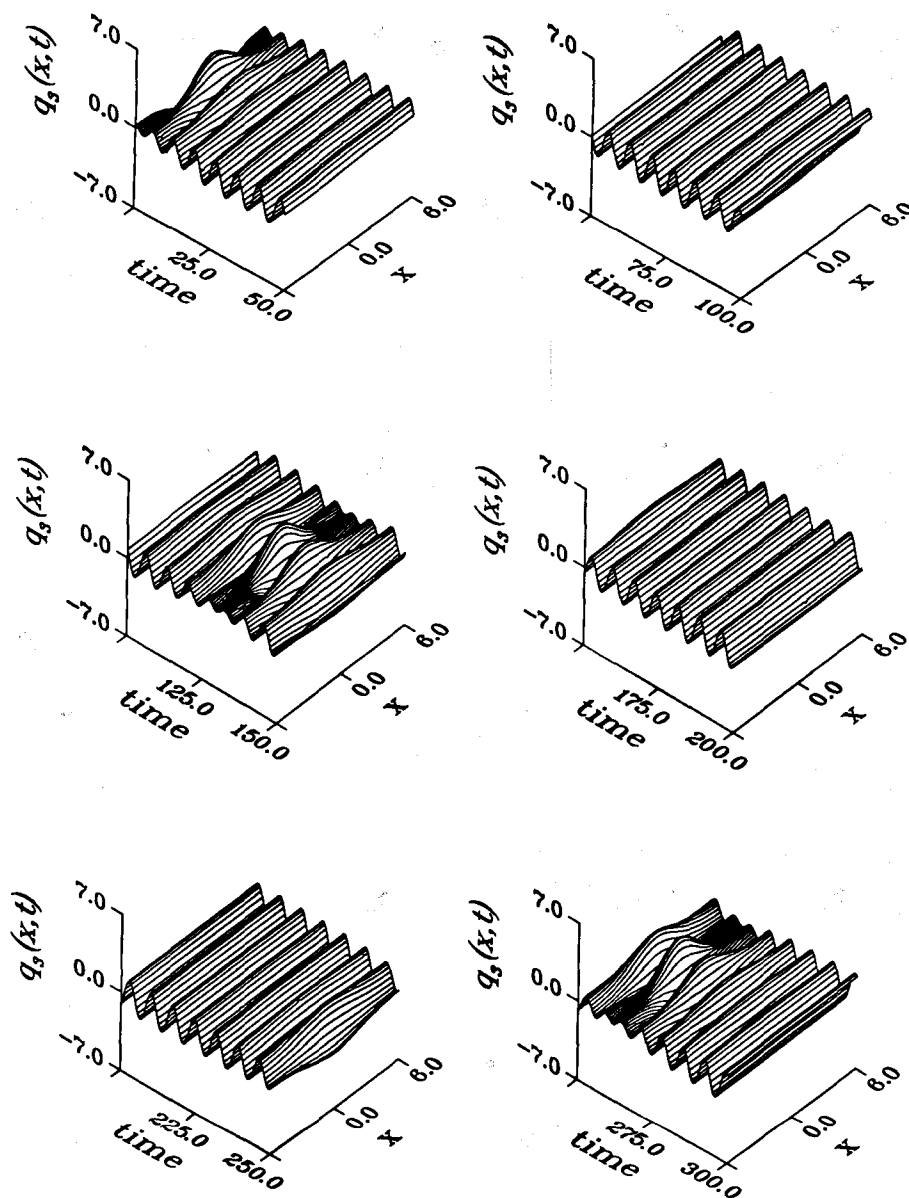


Fig. 36. The three-phase solution with simple spectrum given by eq. (7.5a) is shown.

We compute from the IST algorithm:

$$\kappa_1 = -\kappa_2 = 0.5235964, \quad \kappa_3 = 0, \quad (7.5b)$$

$$\omega_1 = -0.89992, \quad \omega_2 = -\omega_3 = 0.851912. \quad (7.5c)$$

The corresponding x -period is $L = 12$. The waveform $q_3(x, t)$ and spectral configuration are depicted in fig. 36.

Notice how the waveform qualitatively consists of a spatially uniform oscillating background with a breather localized in the center recurring approximately every 130 times units. (This recurring breather

mode can also be moved to the ends of the interval by a discrete phase shift.) In the limit as $E_3 \rightarrow E_5$ ($\phi_3 = \phi_5$), the three-phase simple spectrum $\Sigma_{N=3}^{(s)}$ limits to $\Sigma_{N=1}^{(s)} = \{\frac{1}{16} e^{i\phi_1}, \frac{1}{16} e^{-i\phi_1}, \phi_1 = 0.461011\pi\}$. Recall the one-phase example of section 5, figs. 5b, 6b, 7b, which is identical to this $\Sigma_{N=1}^{(s)}$, and for $L = 12$ we find this $\Sigma_{N=1}^{(s)}$ has one pair of complex double periodic eigenvalues at $\phi = 0.266083\pi$ on the circle of radius of $\frac{1}{16}$.

Near-homoclinic cross configuration

$$\begin{aligned} \Sigma_{N=3}^{(s)} &= \{E_1 = E_2^* = \frac{1}{16} e^{i\phi_1}, E_3 = E_4^* = r e^{i\phi_2}, E_5 = E_6^* = (1/16^2 r) e^{i\phi_2}, \\ \phi_1 &= 0.461011\pi, \phi_2 = 0.26610\pi, r = 0.062\}. \end{aligned} \quad (7.6a)$$

In this limiting regime we find

$$\kappa_1 = -\kappa_2 = 0.5236016, \quad \kappa_3 = 0 \quad (7.6b)$$

$$\omega_1 = -0.978213, \quad \omega_2 = 0.811571, \quad \omega_2 = -0.844892. \quad (7.6c)$$

Notice how this limiting waveform (fig. 37) again has x -period $L = 12$ consisting of a spatially uniform oscillating mean and a breather mode localized alternatively in the center and at the ends of the interval recurring approximately every 185 time units.

These near-homoclinic solutions, figs. 36 and 37, are the saturated 3-phase nonlinear states corresponding to the modulationally unstable 1-phase solution of figs. 5b, 6b, 7b. That is, consider a numerical simulation of the integrable s-G PDE, with even periodic boundary conditions on a length of $L = 12$. Let the initial data $(q(x), q_t(x))$ be given by this single-phase spatially uniform solution of figs. 4b, 5b, 6b, with an arbitrary $\mathcal{O}(\epsilon)$, $0 < \epsilon \ll 1$, perturbation $\epsilon(q_1(x), q_{1t}(x))$. The numerical integration of the integrable PDE will then look like *either* fig. 36 *or* a discrete x -translation of this figure by $L/2$ *or* fig. 37. Moreover, one may observe *all three* possibilities by varying the small perturbation $\epsilon(q_1(x), q_{1t}(x))$. (In private studies with Overman, we have verified these theoretical facts.) It is precisely this “saddle point” structure illustrated by the modulationally unstable one-phase solution, with the associated homoclinic orbit separating the two distinct yet equally likely saturated states of figs. 36 and 37, that forms the basis of our analysis of chaos in the perturbed integrable PDE. This is but one example of modulationally unstable N -phase waves and multiple-component homoclinic degrees of freedom in the integrable sine-Gordon phase space $\mathcal{F}^{(L)}$.

8. One-phase limits and soliton limits of two-phase wavetrains

In section 7 we illustrated a three-phase ($\Sigma_{N=3}^{(s)}$) to one-phase ($\Sigma_{N=1}^{(s)}$) limit, in which two conjugate pairs of simple periodic eigenvalues coalesce into one pair of non-real double periodic eigenvalues. In this limit, the theta function solutions (3.19) only capture the one-phase solution associated to $\Sigma_{N=1}^{(s)}$, although there are homoclinic solutions with the same spectrum due to the nonreal double periodic eigenvalues $E_1^d, (E_1^d)^*$ with positive growth rate (section 5, figs. 4b, 5b, 6b). The existence of homoclinic solutions is supported by the near-homoclinic limits in section 7, figs. 36 and 37: one observes $\mathcal{O}(1)$ coherent spatial structures which recur (appear, then disappear) on long time scales, and the

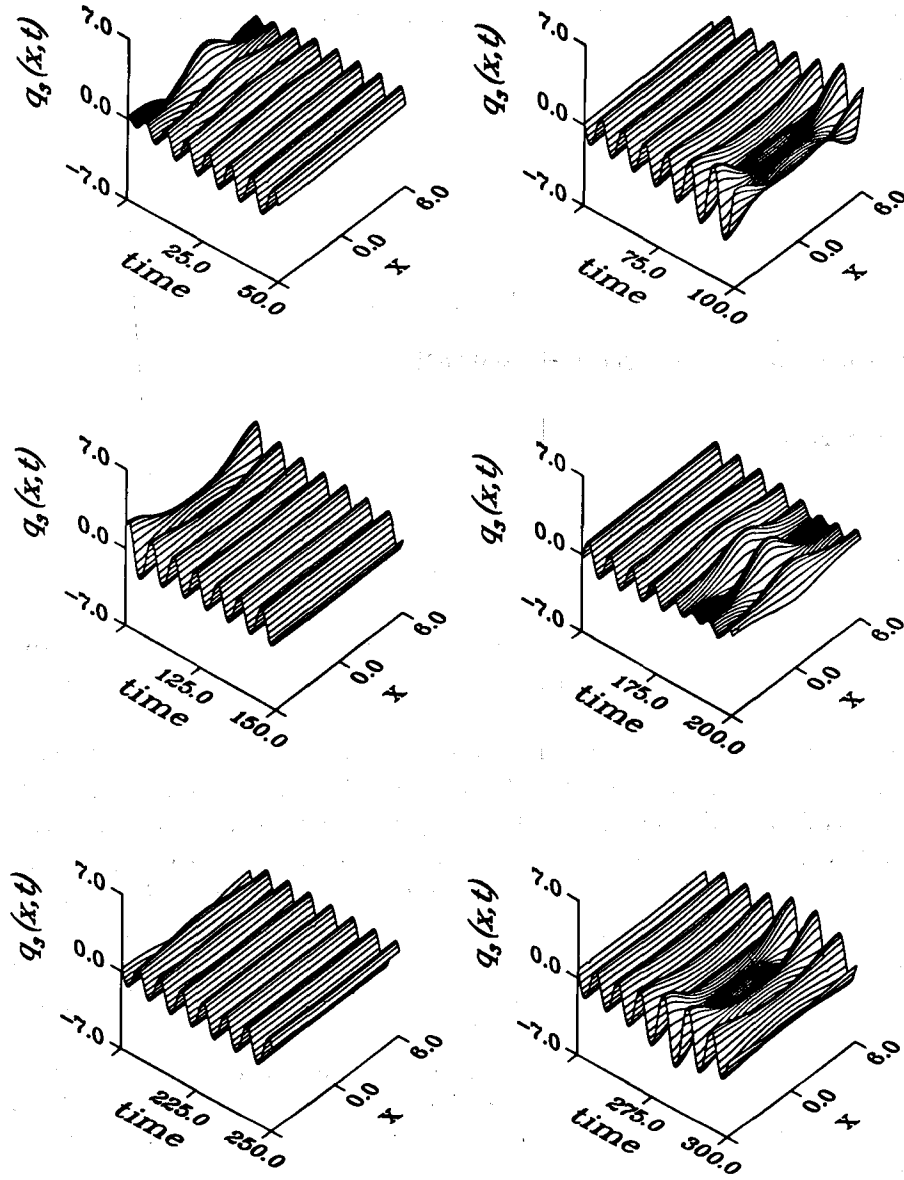


Fig. 37. The three-phase solution with simple spectrum given by eq. (7.6a) is shown.

recurrence-time scales as $\log |E_3 - E_5|^{-1}$. Between these recurrent breather-like modes, the wavetrain is identical to the single-phase uniform solution in fig. 4 computed from $\Sigma_{N=1}^{(s)}$.

There are two additional limits we want to illustrate from the two-phase solutions of section 6: (1) a *two-phase to one-phase limit* in which one pair of simple periodic eigenvalues is pinched together along the positive real axis; and (2) a *soliton limit* in which the spatial period goes to infinity as the two pairs of simple periodic eigenvalues are pinched together off the positive real axis. We will only illustrate a near-breather limit as the simple eigenvalues coalesce off the real axis; the corresponding double kink, kink-antikink, or double antikink solitons occur as the simple eigenvalues coalesce along the negative real axis.

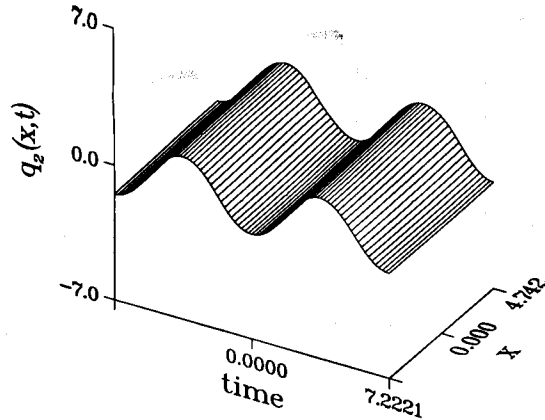


Fig. 38. The two-phase solution with $E_1 = E_2^* = \frac{1}{16} e^{i\pi(0.461011)}$, $E_3 = E_4^* = \frac{1}{16} e^{i\pi(0.001111)}$, $\kappa_1 = -0.662505$, $\kappa_2 = 0$, $\omega_1 = -\omega_2 = -0.869999$, is shown. Note that the solution is very close to the one-phase solution in fig. 4b.

8.1. Two-phase to one-phase limits

We begin with $\Sigma_{N=2}^{(s)}$ of the form in example 6.1, section 6, $\Sigma_{N=2}^{(s)} = \{\frac{1}{16} e^{i\phi_j}, j = 1, \dots, 4, \phi_2 = -\phi_1, \phi_4 = -\phi_3, \phi_1 > \phi_3\}$. We then consider the limit as ϕ_2 and ϕ_4 go to zero, where $\Sigma_{N=2}^{(s)} \rightarrow \Sigma_{N=1}^{(s)}$ of the type computed in figs. 4–5 of section 5.

In fig. 38 we graph the 2-phase solution $q_2(x, t)$ corresponding to $\phi_1 = 0.46011\pi$ and $\phi_2 = 0.0011\pi$. The limiting one-phase solution for which $\phi_2 \equiv 0$, $\phi_1 = 0.461011\pi$ appears in figs. 4b, 5b.

One observes that this is a regular limit in which the amplitude due to the nearly coalesced E_3 and E_4 is uniformly bounded on the order of the radian measure of ϕ_2 .

8.2. Two-phase breather wavetrain to breather soliton limit

Another distinguished limit occurs when the spatial period goes to infinity while the temporal frequency remains bounded, and the coherent spatial structure becomes localized inside of its ever increasing period. This is the *soliton limit* and is achieved by coalescing two simple periodic eigenvalues into a pole of the transfer matrix rather than a double periodic eigenvalue.

We illustrate this limit in fig. 39 from the family of example A.1, section 6, and in fig. 40 from the family of example A.2, section 6. For fig. 39, we have chosen

$$\Sigma_{N=2}^{(s)} = \{\frac{1}{16} e^{i\phi_j}, j = 1, \dots, 4, \phi_2 = -\phi_1, \phi_4 = -\phi_3, \phi_1 = \pi(\frac{1}{3} + \delta), \phi_3 = \pi(\frac{1}{3} - \delta), \delta = 0.0000278\}. \quad (8.1)$$

For fig. 40, we have chosen

$$\Sigma_{N=2}^{(s)} = \{E_1 = E_2^* = r e^{i\phi}, E_3 = E_4^* = (r/16^2) e^{i\phi}, r = \frac{1}{16}(1 - \epsilon), \phi = \pi/3, \epsilon = 0.0048\}. \quad (8.2)$$

In this limit, the imaginary part of the B matrix diverges logarithmically. Since we compute a ratio of theta functions, and factor out the maximum term from each theta series, this divergence does not pose any computational difficulty for the examples presented here.

In each case, (8.1) with fig. 39 and (8.2) with fig. 40, the near-soliton breather has maximum amplitude $= \phi_1 + \phi_3 = 2\pi/3$, which is the amplitude for an infinite-line breather soliton with poles in

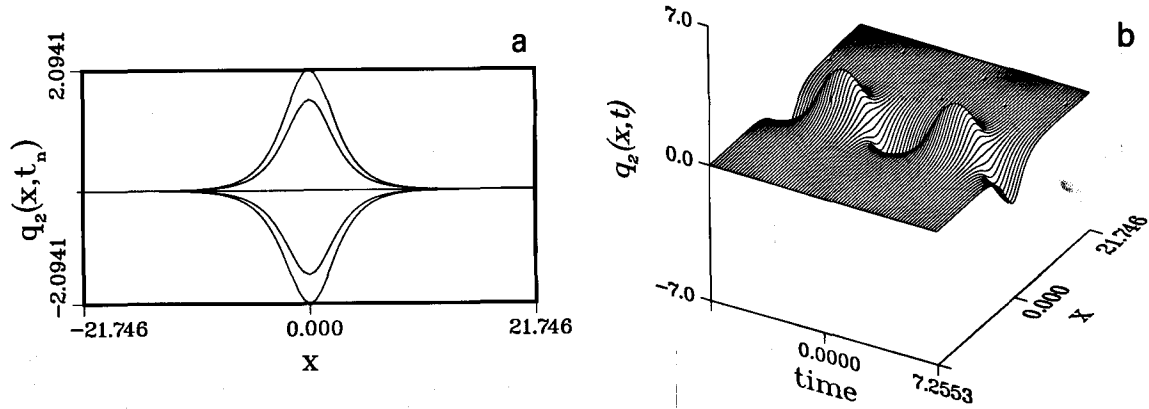


Fig. 39. For the two-phase solution with $E_1 = E_2^* = \frac{1}{16} e^{i\pi(0.333306)}$, $E_3 = E_4^* = \frac{1}{16} e^{i\pi(0.333361)}$, $\kappa_1 = -0.144465$, $\kappa_2 = 0$, $\omega_1 = -\omega_2 = -0.8660$, we show (a) the spatial structure of $q_2(x, t_n)$ at selected times $t_n = n(T/8)$, $n = -4, -3, \dots, 4$, $T = 7.2553$, (b) the surface $q_2(x, t)$ over one x -period and two temporal periods.

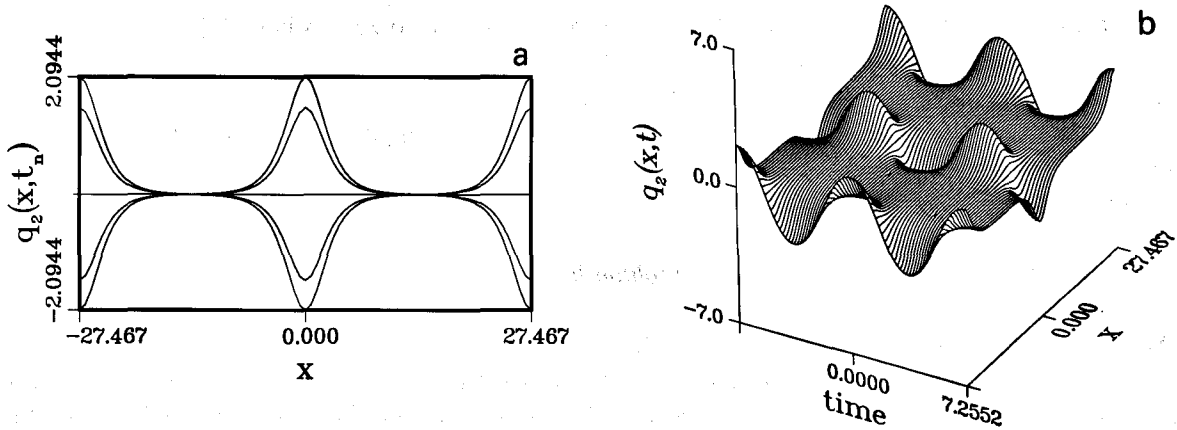


Fig. 40. For the two-phase solution with $E_1 = E_2^* = 0.0622 e^{i\pi/3}$, $E_3 = E_4^* = 0.0628015 e^{i\pi/3}$, $\kappa_1 = \kappa_2 = -0.114376$, $\omega_1 = -\omega_2 = -0.86603$, we show (a) the spatial structure of $q_2(x, t_n)$ at selected times $t_n = n(T/8)$, $n = -4, -3, \dots, 4$, $T = 7.25517$, (b) the surface $q_2(x, t)$ over one x -period and two temporal periods.

the scattering matrix at $E = \frac{1}{16} e^{i\pi/3}$, $\frac{1}{16} e^{-i\pi/3}$. Notice, however, that the limiting breather waveform from the spectral class (8.1) has one breather per period whereas the limiting waveform in spectral class (8.2) has two breathers per period. In fact, the sine-Gordon energy, $H = \int_0^L [\frac{1}{2}(q_t^2 + q_x^2) + 1 - \cos q] dx$, in fig. 39 is exactly one-half the energy in fig. 40. The limiting breather frequency in these examples is $2\pi/T$, where the t -period $T = 7.2552$.

The above examples of figs. 39, 40 are *standing* breathers in the near-soliton limit. These solutions are even in x and do not translate as they “breathe”. To achieve breather solitons which translate and breathe we must break the $E \rightarrow 1/16^2 E$ symmetry in the spectrum. We illustrate such an example in fig. 41 where $E_1 \approx E_3 \approx 0.045 e^{i\pi/3}$, $E_2 \approx 0.045 e^{-\pi/3}$, which produces a breather moving to the right with velocity $v \approx -0.163$.

In fig. 42 we choose a near-soliton spectrum $\Sigma_{N=2}^{(g)}$ which is the inversion of the fig. 41 spectrum through the circle $|E| = \frac{1}{16}$: $E_1 \approx E_3 \approx [1/16^2(0.045)] e^{i\pi/3}$, which produces an identical breather to fig. 41 except the phase velocity $v \approx 0.163$, so that the breather travels to the left.

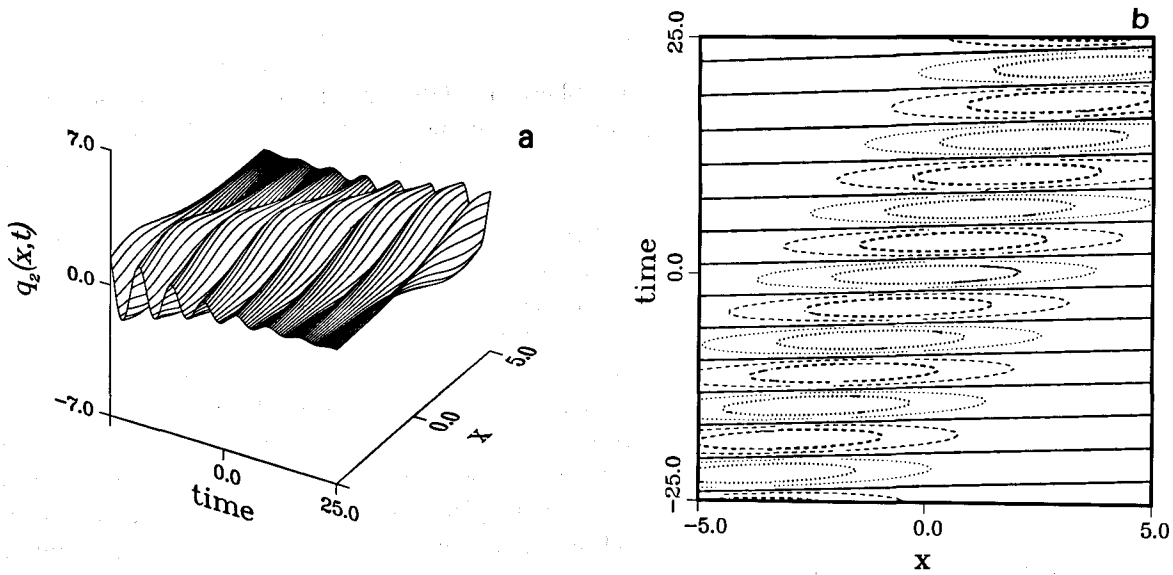


Fig. 41. For the two-phase solution with $E_1 = E_2^* = 0.045 e^{i\pi(0.33056)}$, $E_3 = E_4^* = 0.045 e^{i\pi(0.33611)}$, $\kappa_1 = -0.39673$, $\kappa_2 = -0.14288$, $\omega_1 = 0.91905$, $\omega_2 = -0.87772$, we show (a) contour levels of the surface $q_2(x, t)$, (b) the surface $q_2(x, t)$ for $-5 \leq x \leq 5$ and $-25 \leq t \leq 25$. Note that the solution is quasiperiodic in x .

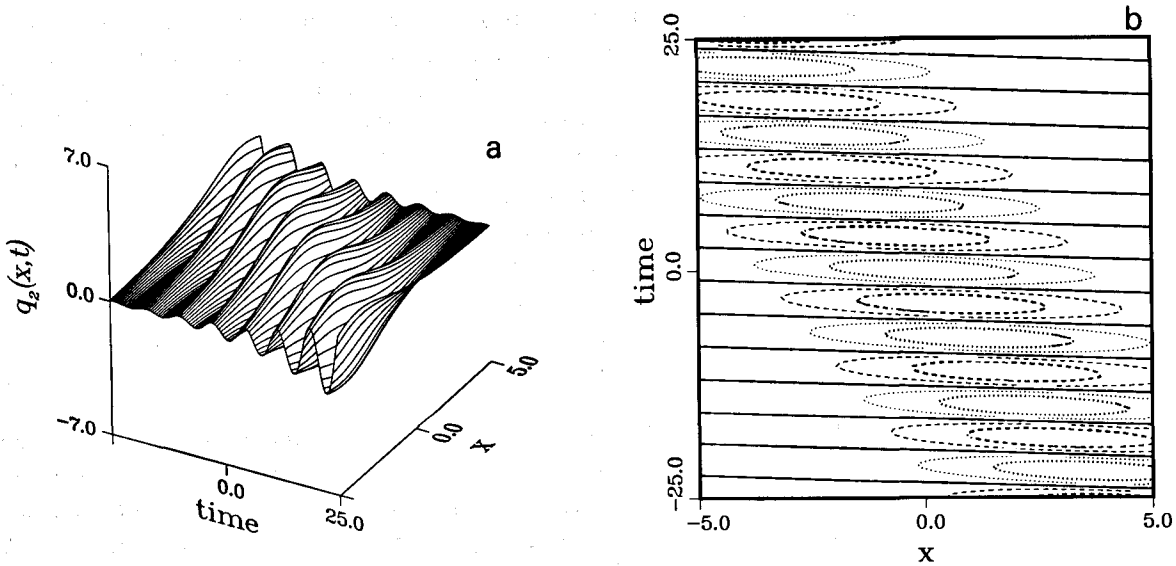


Fig. 42. For the two-phase solution with $E_1 = E_2^* = 0.0086806 e^{i\pi(0.33056)}$, $E_3 = E_4^* = 0.086806 e^{i\pi(0.33611)}$, $\kappa_1 = -0.11096$, $\kappa_2 = -0.14288$, $\omega_1 = 0.83640$, $\omega_2 = -0.87772$, we show (a) contour levels of the surface $q_2(x, t)$, (b) the surface $q_2(x, t)$ for $-5 \leq x \leq 5$ and $-25 \leq t \leq 25$. Note that the solution is quasiperiodic in x .

9. Conclusion

We have displayed periodic one-, two- and three-phase sine-Gordon wavetrains as generated by the IST algorithm. Along the way, we have also computed those spectral theoretic ingredients which are fundamental to x -periodic solutions, both in labelling instabilities and in computing linearized growth rates.

These numerical calculations have been helpful in clarifying several theoretical and experimental results for the periodic sine-Gordon equation. For example, we have provided an explicit 2-phase x -periodic family of solutions which are *potentially* unstable due to non-real double periodic eigenvalues but which have zero growth rates in these modes. Our theoretical results [17] imply that the next higher sine-Gordon flow *must* have an instability in this mode for solutions with this spectrum. Until these computations, we did not have any examples of this type. In section 7 we have illustrated the integrable three-phase periodic wavetrains which are observed in previous studies [10, 11] of chaos in the perturbed s-G PDE. The “cross” and the “gap” spectral configurations that accompany the distinct 3-phase even breather trains provide a definitive measure of the homoclinic crossings referred to in our nearly integrable chaos studies [10, 11]. These figures confirm the qualitative difference in the solutions that is so evident in the spectrum: the “cross” spectrum yields solutions where the breather passes from the center to the wings, whereas the “gap” spectrum yields either a breather at the center for all time or a breather in the wings for all time, and the choice is made depending on a discrete parameter. We refer to ref. [22] for a topological interpretation of these results.

The IST solution algorithm is clear and straightforward, as described herein for the sine-Gordon PDE and likewise for all integrable equations whose theta function solutions are defined with respect to hyperelliptic Riemann surfaces (e.g. Korteweg–de Vries, non-linear Schrödinger, the Toda lattice, and the sinh–Poisson equation whose doubly periodic solutions yield non-spherical surfaces of constant mean curvature which can be imbedded in \mathbb{R}^3). Two potential numerical difficulties arise from either (i) the computation of period information on the Riemann surface defined by IST input data or (ii) the summation of N -fold theta series. In this paper we have shown a general prescription that resolves these difficulties in the hyperelliptic case. The remaining obstruction is in prescribing the set $\Sigma_N^{(s)}$ of simple periodic eigenvalues corresponding to an N -phase x -periodic wavetrain. That is, one cannot a priori give $\Sigma_N^{(s)}$. Rather, it is necessary to search a real $2N$ -dimensional space for N -dimensional subsets which meet the N transcendental fixed period constraints. However, wavetrains quasiperiodic in x and t do not pose any difficulties whatsoever.

The limiting cases of singular Riemann surfaces, which arise as two pairs of simple periodic eigenvalues coalesce off the real axis, have not been computed at the limit configuration. We have, however, illustrated how our codes apply very near this limit. The solutions that we therefore have *not* displayed here, corresponding to non-real double periodic eigenvalues, are homoclinic solutions [17]. These homoclinic orbits exist for the periodic sine-Gordon and focusing nonlinear Schrödinger equations [17, 23] and may be computed with a slight embellishment of the present paper, employing Baker eigenfunctions of the linear system (1.3).

References

- [1] H. Flaschka, The Toda lattice I, II, Phys. Rev. B 9 (1975) 1924–1925, Prog. Theor. Phys. 51 (1974) 703–716.
- [2] H.P. McKean and P. Van Moerbeke, The spectrum of Hill’s equation, Inventiones Math. 30 (1975) 217–274.

- [3] B.A. Dubrovin, V.B. Matveev and S.P. Novikov, Nonlinear equations of Korteweg-de Vries type, finite-zone linear operators, and Abelian varieties, *Usp. Mat. Nauk.* 31 (1976) 55–136.
- [4] E. Tracy, Ph.D. Thesis, Department of Physics, University of Maryland (1984).
- [5] M.G. Forest and D.W. McLaughlin, Spectral theory for the periodic sine-Gordon equation: a concrete viewpoint, *J. Math. Phys.* 23 (1982) 1248–1277.
- [6] N.M. Ercolani and M.G. Forest, The geometry of real sine-Gordon wavetrains, *Commun. Math. Phys.* 99 (1985) 1–49.
- [7] H.P. McKean, The sine-Gordon and sinh-Gordon equations on the circle, *Comm. Pure Appl. Math.* 34 (1981) 197–257.
- [8] A. Finkel and H. Segur, *Stud. Appl. Math.* 73 (1985) 183; J. Hammack, N. Sheffner and H. Segur, in: *Nonlinear Ocean Physics: Proceedings of the Enrico Fermi Summer School*, ed. A.R. Osborne (North-Holland, Amsterdam, 1989).
- [9] J.P. Boyd, Theta functions, Gaussian series, and spatially periodic solutions of the KdV equation, *J. Math. Phys.* 23 (1982) 375–387.
- [10] A.R. Bishop, M.G. Forest, D.W. McLaughlin and E.A. Overman, A quasiperiodic route to chaos in a near-integrable PDE, *Physica D* 23 (1986) 293–328.
- [11] A.R. Bishop, M.G. Forest, D.W. McLaughlin and E.A. Overman, A quasiperiodic route to chaos in a near-integrable PDE: homoclinic crossings, *Phys. Lett. A* 127 (1988) 335–340.
- [12] N.M. Ercolani, M.G. Forest and D.W. McLaughlin, Fully nonlinear modal equations for nearly integrable PDE's, O.S.U. preprint (1988).
- [13] W. Ferguson, H. Flaschka and D.W. McLaughlin, Nonlinear normal modes of the Toda chain, *J. Comput. Phys.* 45 (1982) 157–209.
- [14] L. Bergamasco and A.R. Osborne, *Physica D* 18 (1986) 26.
- [15] E.A. Overman, D.W. McLaughlin and A.R. Bishop, Coherence and chaos in the driven, damped sine-Gordon equation: measurement of the soliton spectrum, *Physica D* 19 (1986) 1–41.
- [16] E.A. Overman, private communication.
- [17] N.M. Ercolani, M.G. Forest and D.W. McLaughlin, Geometry of the modulational instability, I. Local analysis, *Memoirs Am. Math. Soc.*, to appear; Geometry of the modulational instability, II. Global results, *Memoirs Am. Math. Soc.*, to appear; Geometry of the modulational instability, III. Homoclinic orbits for the periodic sine-Gordon equation, *Physica D* 43 (1990) 349–384.
- [18] C.L. Siegel, *Topics in Complex Function Theory*, Vol. II (Wiley-Interscience, New York, 1971).
- [19] M.G. Forest and D.W. McLaughlin, Modulations of sine-Gordon and sinh-Gordon wavetrains, *Stud. Appl. Math.* 68 (1983) 11–59.
- [20] N.M. Ercolani, M.G. Forest and D.W. McLaughlin, Modulational stability of two-phase sine-Gordon wavetrains, *Stud. Appl. Math.* 71 (1984) 91–101.
- [21] N.M. Ercolani, M.G. Forest and D.W. McLaughlin, private notes.
- [22] N.M. Ercolani and D.W. McLaughlin, Toward a topological classification of integrable PDE's, in: *Proceedings of MSRI Workshop*, Berkeley, CA, 1990, to appear.
- [23] N.M. Ercolani, M.G. Forest and D.W. McLaughlin, Notes on Melnikov integrals for the perturbed nonlinear Schrödinger equations, University of Arizona preprint (1988).

THE UNIVERSITY OF CHICAGO

THE UNIVERSITY OF CHICAGO
CHICAGO, ILLINOIS 60637

THE UNIVERSITY OF CHICAGO
CHICAGO, ILLINOIS 60637

THE UNIVERSITY OF CHICAGO
CHICAGO, ILLINOIS 60637

THE UNIVERSITY OF CHICAGO
CHICAGO, ILLINOIS 60637

THE UNIVERSITY OF CHICAGO
CHICAGO, ILLINOIS 60637

THE UNIVERSITY OF CHICAGO
CHICAGO, ILLINOIS 60637

THE UNIVERSITY OF CHICAGO
CHICAGO, ILLINOIS 60637

THE UNIVERSITY OF CHICAGO
CHICAGO, ILLINOIS 60637

THE UNIVERSITY OF CHICAGO
CHICAGO, ILLINOIS 60637

THE UNIVERSITY OF CHICAGO
CHICAGO, ILLINOIS 60637

THE UNIVERSITY OF CHICAGO
CHICAGO, ILLINOIS 60637